

UNIVERSIDAD DE MURCIA

Escuela de Doctorado

TESIS DOCTORAL

Simulador Visual Binocular de Óptica Adaptativa con control automático de vergencia

Binocular Visual Adaptive Optics Simulator with automatic vergence control

AUTOR Santiago Sager La Ganga

DIRECTORES Pablo Artal Soriano

Pedro María Prieto Corrales

2026



UNIVERSIDAD DE MURCIA Escuela de Doctorado

TESIS DOCTORAL

Simulador Visual Binocular de Óptica Adaptativa con control automático de vergencia

Binocular Visual Adaptive Optics Simulator with automatic vergence control

AUTOR Santiago Sager La Ganga

DIRECTORES Pablo Artal Soriano
Pedro María Prieto Corrales

2026

UNIVERSIDAD DE MURCIA

DECLARACIÓN DE AUTORÍA Y ORIGINALIDAD DE LA TESIS PRESENTADA PARA OBTENER EL TITULO DE DOCTOR/A

Aprobado por la Comisión General de Doctorado el 19 de octubre de 2022.

Yo, D. Santiago Sager La Ganga, habiendo cursado el Programa de Doctorado Ciencias de la Visión de la Escuela Internacional de Doctorado de la Universidad de Murcia (EIDUM), como autor/a de la tesis presentada para la obtención del título de Doctor/a titulada:

A Binocular Visual Adaptive Optics Simulator with automatic vergence control

y dirigida por:

D.: Pablo Artal Soriano
D.: Pedro María Prieto Corrales
D.:

DECLARO QUE:

La tesis es una obra original que no infringe los derechos de propiedad intelectual ni los derechos de propiedad industrial u otros, de acuerdo con el ordenamiento jurídico vigente, en particular, la Ley de Propiedad Intelectual (R.D. legislativo 1/1996, de 12 de abril, por el que se aprueba el texto refundido de la Ley de Propiedad Intelectual, modificado por la Ley 2/2019, de 1 de marzo, regularizando, aclarando y armonizando las disposiciones legales vigentes sobre la materia), en particular, las disposiciones referidas al derecho de cita, cuando se han utilizado sus resultados o publicaciones.

Del mismo modo, asumo ante la Universidad cualquier responsabilidad que pudiera derivarse de la autoría o falta de originalidad del contenido de la tesis presentada, en caso de plagio, de conformidad con el ordenamiento jurídico vigente.

Murcia, a 27 de abril de 2026

(firma)

Información básica sobre protección de sus datos personales aportados:	
Responsable	Universidad de Murcia. Avenida teniente Flomesta, 5. Edificio de la Convalecencia. 30003; Murcia. Delegado de Protección de Datos: dpd@um.es
Legitimación	La Universidad de Murcia se encuentra legitimada para el tratamiento de sus datos por ser necesario para el cumplimiento de una obligación legal aplicable al responsable del tratamiento. art. 6.1.c) del Reglamento General de Protección de Datos
Finalidad	Gestionar su declaración de autoría y originalidad
Destinatarios	No se prevén comunicaciones de datos
Derechos	Los interesados pueden ejercer sus derechos de acceso, rectificación, cancelación, oposición, limitación del tratamiento, olvido y portabilidad a través del procedimiento establecido a tal efecto en el Registro Electrónico o mediante la presentación de la correspondiente solicitud en las Oficinas de Asistencia en Materia de Registro de la Universidad de Murcia

Esta DECLARACIÓN DE AUTORÍA Y ORIGINALIDAD debe ser insertada en la quinta hoja, después de la portada de la tesis presentada para la obtención del título de Doctor/a.

Firmante: SANTIAGO SAGER LA GANGA; Fecha-hora: 27/04/2026 18:21:57; Emisor del certificado: CN=AC FNMT Usuarios,OU=Ceres,O=FNMT-RCM,C=ES;

@dministración electrónica

Código seguro de verificación: RUxFMn7S-R+zZ558I-N2Y1RNVd-6QDvpc6K

COPIA ELECTRÓNICA - Página 1 de 1

Esta es una copia auténtica imprimible de un documento administrativo electrónico archivado por la Universidad de Murcia, según el artículo 27.3 c) de la Ley 39/2015, de 1 de octubre. Su autenticidad puede ser contrastada a través de la siguiente dirección: https://sede.um.es/validador/

Contents

Abstract 7

Resumen 9

Chapter 1: Introduction 15

1.1. Adaptive Optics (AO) 16
1.1.1. Wavefront sensing 17
1.1.2. Wavefront shaping 21
1.1.3. AO in ophthalmology 23
1.2. Adaptive Optics Visual Simulators (AOVS) 25
1.2.1. AOVS prototypes 25
1.2.2. Binocular AOVS (B-AOVS) 27
1.3. B-AOVS applications 30
1.3.1. Vergence-Accommodation Conflict (VAC) 30
1.4. Objectives and purpose 34

Chapter 2: Design and assembly of the B-AOVS 36

2.1. Optical design 37
2.2. Instrument alignment 41
2.2.1. Visual path 41
2.2.2. Measurement path 42
2.2.3. Motorized periscope 43
2.3. Instrument calibration 46
2.3.1. Intensity modulator 46
2.3.2. Phase modulator 46
2.3.3. Stimulus screen 47
2.3.4. Hartmann-Shack sensor 48
2.3.5. Tunable lens 50
2.3.6. Positioning camera 51
2.3.7. Motorized periscope 52
2.4. Instrument validation 57
2.4.1. Wavefront sensing 57
2.4.2. Stimulus generation 58

2.4.3. Phase modulation 59

Chapter 3: Applications 61

3.1. Through-focus curves with and without matching convergence 62

3.1.1. Methods 62

3.1.2. Results 64

3.1.3. Discussion 67

3.2. Effect of spherical aberration on the vergence-accommodation conflict 69

3.2.1. Methods 70

3.2.2. Results 75

3.2.3. Discussion 81

Chapter 4: Conclusions 84

Bibliography 86

Agradecimientos 97

Abstract

Adaptive Optics Visual Simulators are powerful tools that have significantly advanced our understanding of human vision, particularly regarding the role of optical aberrations. These instruments have contributed to deeper insights into visual pathologies, the interplay between optical and neural components of vision, and the development of optical interventions aimed at improving quality of life.

Despite their impact, the majority of existing prototypes are monocular, inherently limiting their ability to explore binocular vision. Among the few binocular adaptive optics systems developed worldwide, none offers a practical and rapid method for controlling vergence angle. This limitation leaves a critical aspect of binocular vision, vergence, largely unexamined under controlled aberration conditions. Vergence is intrinsically linked to accommodation and plays a crucial role in a variety of applications. The aim of this thesis is to develop a Binocular Adaptive Optics Visual Simulator that leverages the advantages of adaptive optics in a compact, cost-effective configuration, while integrating a motorized vergence control system for rapid and precise adjustment of vergence angles. This document details the design, development, and validation of the instrument.

The new vergence control system was designed to provide full adjustment of the lines of sight of both eyes. This was achieved by synchronized rotation of two mirrors mounted on servomotors while the interpupillary distance was tuned by axially displacing a prism mirror mounted on a stepper motor. The addition of automatic angular control allows a more realistic study of binocular vision under the effect of optical aberrations and other complex phase profiles, as well as their relationship with the vergence-accommodation conflict. Additionally, the prototype provides the core functionalities characteristic of visual simulators, including two microdisplays for independent stimulus presentation, two liquid crystal on silicon spatial light modulators that control pupil size and aberration correction, a Hartmann-Shack wavefront sensor for aberration measurement, and a tunable lens to extend the system's measurement and correction range.

The first study conducted with the new instrument aimed to test the impact of vergence control on through-focus measurements performed in subjects with absent accommodation. Previous simulators have been used to perform similar studies under the assumption that the

vergence-accommodation conflict plays no role when the subject lacks an accommodative response, thus circumventing the need to match the vergence angle to the simulated stimulus distance. To test this hypothesis, visual acuity was measured for different distances and spherical aberration conditions with either matching convergence or a fixed vergence angle at 0 diopters. Results showed minimal differences between vergence conditions, supporting the validity of prior studies conducted with systems lacking vergence control.

A second study tested the effect of the vergence-accommodation conflict on stereoacuity and subjective experience trough different spherical aberration profiles, a previously uncharted line of research now enabled by the development of a binocular adaptive optics simulator with vergence control. While stereoacuity results did not show a significant improvement for the different profiles, a certain amount of spherical aberration seemed to homogenize subjective experience. This could prove to be impactful in certain applications such as extended reality, where dynamic vergence changes are common and the peaks of discomfort create a worse user experience.

The binocular adaptive optics visual simulator prototype developed in this thesis opens new avenues of research on previously unexplored topics on account of its automatic vergence control system. Binocular vision can now be assessed under more realistic conditions, providing better insight into the effect of different optical profiles on stereoscopic vision. On the other hand, independent vergence control provides a unique tool to assess the vergence-accommodation conflict and the potential effect of introducing different phase profiles, an innovative optical solution that could have a strong impact on applications such as extended reality.

Resumen

Los Simuladores Visuales de Óptica Adaptativa son herramientas potentes que han contribuido significativamente al avance en la comprensión de la visión humana, especialmente en lo que respecta al papel de las aberraciones ópticas. Estos instrumentos han permitido obtener conocimientos más profundos sobre las patologías visuales, la interacción entre los componentes ópticos y neuronales de la visión, así como el desarrollo de soluciones ópticas orientadas a mejorar la calidad de vida de los pacientes. A pesar de su impacto, la mayoría de los prototipos existentes son monoculares, lo que limita inherentemente su capacidad para explorar aspectos de la visión binocular.

Entre los escasos sistemas binoculares de óptica adaptativa desarrollados a nivel mundial, ninguno ofrece un método práctico y rápido para el control del ángulo de vergencia. Esta limitación deja sin explorar un aspecto fundamental de la visión binocular, la vergencia, bajo condiciones controladas de aberraciones ópticas. La vergencia está intrínsecamente relacionada con la acomodación y tiene un papel crucial en diversas aplicaciones. Esta relación es particularmente importante en el campo de la realidad extendida, donde el conflicto entre acomodación y convergencia puede generar fatiga y malestar tras el uso prolongado de estos dispositivos. Aunque se han propuesto en la literatura múltiples alternativas de diseño para aliviar este problema, todas ellas tienen limitaciones como elevados costes, excesivo tamaño o peso, u otros problemas en la calidad óptica. Una potencial solución es el efecto de una profundidad de foco extendida generada mediante la inducción de aberraciones, que no se ha explorado hasta ahora principalmente debido a la ausencia de instrumentación que permitiera evaluar su impacto. En caso de reducir la fatiga y el mareo asociados al uso prolongado de la realidad aumentada y virtual, esta solución podría implementarse de forma barata y sencilla usando máscaras de fase añadidas al dispositivo o lentes de contacto válidas para la mayoría de los instrumentos. El prototipo propuesto de simulación visual de óptica adaptativa con control de vergencia podría usarse, entre otras líneas de investigación, para estudiar este campo previamente inexplorado.

El objetivo de esta tesis ha sido el desarrollo de un Simulador Visual Binocular de Óptica Adaptativa con un sistema motorizado de control de vergencia que permita ajustar de manera rápida y precisa los ángulos deseados, permitiendo simulaciones binoculares realistas en una

configuración compacta. Esta Tesis describe el diseño, alineación y validación del dispositivo desarrollado.

El nuevo sistema de control de vergencia ha sido diseñado para permitir un ajuste completo de las líneas de visión de ambos ojos. Esto se ha conseguido sincronizando la rotación de dos espejos montados en servomotores a la vez que se ajusta la distancia interpupilar desplazando axialmente un prisma reflectante montado en un motor paso a paso. Esta adición permite un estudio más realista de la relación entre vergencia y acomodación y el impacto de aberraciones ópticas y otros perfiles de fase complejos. Además, con este sistema se ha buscado mejorar las funcionalidades principales características de los simuladores visuales de óptica adaptativa, incluyendo dos microdisplays para la presentación independiente de estímulos, dos moduladores de cristal líquido sobre silicio que controlan el tamaño de la pupila y la corrección de aberraciones, un sensor de frente de onda tipo Hartmann-Shack para la medida de las aberraciones, y una lente optoelectrónica de foco ajustable para extender el rango de corrección y medida del sistema.

El nuevo prototipo incorpora un diseño compacto que facilita su potencial adaptación a un entorno clínico. El instrumento, basado en una iteración previa del Laboratorio de Óptica de la Universidad de Murcia, consta de dos ramas principales. El camino visual incorpora la funcionalidad de presentación de estímulos necesarias para realizar los tests visuales junto con la capacidad de corrección de aberraciones y de simulación de perfiles de fase. Por otra parte, el camino de medida incluye la capacidad de posicionar al sujeto y de medir las aberraciones de ambos ojos. Finalmente, el sistema periscópico permite separar las pupilas generadas por el sistema para coincidir con las pupilas naturales del sujeto.

Las pantallas de estímulos forman el inicio del camino visual, compartiendo un único camino óptico gracias a un prisma reflectante. El uso de dos pantallas permite la presentación independiente de estímulos para cada ojo y por tanto la presentación de estímulos estereoscópicos. La lente colimadora se ha elegido teniendo en cuenta el tamaño de las pantallas de estímulos para obtener el mayor campo visual posible mientras que se mantiene una resolución suficiente para no imponer limitaciones en los tests visuales. Una pantalla de cristal líquido sobre silicio posicionada entre polarizadores cruzados actúa como modulador de intensidad para crear las aperturas que actúan como aberturas del sistema, mientras que la siguiente pantalla de cristal líquido actúa como modulación de fase e introduce los perfiles necesarios en un plano conjugado a la generación de pupilas. La lente optoelectrónica se encuentra en el siguiente plano conjugado, y finalmente el periscopio separa las pupilas del

sistema antes del plano final donde se encontrarán las pupilas del sujeto. El camino de medida está formado por el láser separado en dos haces para medir ambos ojos. El aumento del camino óptico se ha elegido, teniendo en cuenta el tamaño del sensor del frente de onda, para permitir la medida simultánea de ambos ojos a la vez que se maximiza el rango y precisión de la medida.

El correcto alineamiento del sistema se realizó con un interferómetro para posicionar las lentes creando telescopios afocales. Las posiciones de las pantallas de estímulos, pantalla de generación de pupila, el modulador de fase, y lente ajustable se determinaron formando imagen con una cámara enfocada a infinito y asegurando que estaba correctamente enfocada. De la misma forma se aseguró la coincidencia del láser de medida con el camino óptico de las pantallas de estímulos para una correcta iluminación en fóvea, mientras que el reflejo del láser hacia el interior del sistema indicó la posición óptima del sensor de frente de onda. Las posiciones angulares base de los motores del sistema de convergencia se obtuvieron manteniendo paralelos dos láseres alineados con el camino óptico de las pantallas de estímulos.

Con todos los elementos ópticos posicionados en su lugar, el siguiente paso fue realizar un calibrado para asegurar el correcto comportamiento del instrumento. Debido al ángulo al que se encuentran posicionados ambos moduladores, las imágenes introducidas generan elipticidad. Para determinar la deformación, se aplicó un programa de detección de bordes a las imágenes de las pupilas generadas por el modulador de intensidad y capturadas con una cámara externa. Una vez corregidos los parámetros medidos, se comprobó que el resultado final era circular. Un procedimiento parecido se usó con el modulador de fase, en este caso usando imágenes de anillos características al introducir desenfoque y ajustando el sistema de detección. Las pantallas de estímulos se calibraron en términos de su tamaño de píxel final y calidad de imagen. El tamaño de píxel se obtuvo capturando una imagen en el plano de pupila con una cámara, y se empleó una métrica de calidad de imagen para corregir las aberraciones introducidas por el sistema.

El sensor de Hartmann-Shack se calibró utilizando un láser externo con el que se obtuvo una imagen de referencia para eliminar las aberraciones internas del sistema. Se determinó la distancia efectiva entre las microlentes y el sensor de la cámara midiendo una serie de lentes de prueba en un rango de -10D a +10D y realizando un ajuste entre los resultados medidos y las potencias nominales de las lentes. Las mismas lentes de prueba se emplearon para calibrar la capacidad de corrección de la lente optoelectrónica, obteniendo el voltaje necesario para compensar el desenfoque producido por cada una de ellas. Por último, se usó una regla

milimétrica en el plano de pupila para calcular el tamaño de pixel de la cámara de posicionamiento, y una apertura situada en el plano de pupila para obtener las coordenadas usadas para centrar a los sujetos.

Finalmente, se calibró el periscopio automatizado, una tarea esencial para asegurar el correcto funcionamiento del sistema de control de vergencia. El movimiento generado por el motor paso a paso se midió para obtener un parámetro de conversión entre pasos y milímetros. La precisión de esta calibración se comprobó introduciendo un ángulo de vergencia y compensando el desplazamiento con el motor, resultando en errores de desplazamiento por debajo de las tolerancias necesarias para el correcto funcionamiento del instrumento.

La validación del instrumento se realizó en dos pasos. Para la rama de medida se usó un ojo artificial con diferentes lentes de prueba, simulando ojos reales con diferentes valores refractivos. Los resultados mostraron errores pequeños comparados con los valores nominales de las lentes, demostrando el correcto comportamiento del sensor de Hartmann-Shack. La calidad de la rama visual se comprobó comparando las imágenes de las pantallas correspondientes a cada ojo del instrumento con la pantalla del simulador visual de óptica adaptativa VAO comercializado por Voptica. Calculando métricas de enfoque se obtuvieron valores similares entre todas las imágenes, tendencia que se mantuvo al introducir perfiles bifocales en el modulador de fase y por tanto se tomó como un indicador de una calidad de imagen adecuada y un correcto comportamiento del modulador de fase.

El primer estudio realizado con el nuevo prototipo fue la medida de curvas de desenfoque en sujetos sin capacidad acomodativa, comparando situaciones de vergencia fija y vergencia correspondiente al desenfoque inducido. Las medidas en sujetos présbitas o con acomodación paralizada en condiciones de vergencia fija son comunes en previas versiones de simuladores visuales binoculares, bajo la suposición de que dada la ausencia de capacidad acomodativa no es necesaria la inclusión del control de vergencia. Aunque la mayor parte del efecto del conflicto acomodación-vergencia se elimina si el ojo no puede variar su potencia, ciertos estudios han sugerido que efectos secundarios de la introducción de vergencia como el cambio de tamaño de pupila podrían afectar al resultado de las curvas de desenfoque. Para comprobar esta hipótesis, se midió la agudeza visual para diferentes distancias y valores de aberración esférica con una convergencia acorde a la distancia o un ángulo de vergencia fijo a 0 dioptrías. Los resultados mostraron la diferencia esperada al introducir la aberración esférica, mejorando la agudeza visual para estímulos más cercanos debido a su aumento de la profundidad de foco a costa de reducir la calidad de la imagen para distancias lejanas. Sin embargo, las diferencias

entre las condiciones con y sin vergencia variable fueron negligibles, sugiriendo que el rol de la vergencia es mínimo en ausencia de acomodación. Tampoco se observaron cambios apreciables en los resultados para un sujeto présbita, cuya pupila mostró reacciones normales a los cambios de vergencia, lo que sugiere que la miosis no parece ser un factor disruptivo en este tipo de estudios. Estas pruebas aportan validez a estudios anteriores realizados sin control de convergencia, y refuerzan la capacidad de previos simuladores visuales binoculares de realizar medidas en sujetos carentes de acomodación.

Adicionalmente, se realizó un estudio de estereopsis bajo diferentes niveles de conflicto entre vergencia y acomodación y con diferentes cantidades de aberración esférica. El parámetro visual analizado fue la estereoagudeza, dado que se ha demostrado anteriormente su deterioro a medida que aumenta la diferencia entre acomodación y vergencia, y el estudio se complementó con un cuestionario subjetivo para comprobar los niveles de fatiga y malestar durante las pruebas. La capacidad única del instrumento para cambiar el ángulo de vergencia de forma rápida se empleó para realizar múltiples cambios entre condiciones del conflicto, proporcionando un mayor número de puntos para el cuestionario subjetivo y aleatorizando mejor el efecto de la fatiga para las diferentes condiciones durante la prueba.

Los resultados mostraron el esperado empeoramiento de la estereopsis al aumentar el conflicto en la dirección negativa, pero este efecto no se vio reducido al introducir la aberración esférica como cabría esperar debido al aumento de profundidad de foco. En este sentido, parece que la aberración esférica no proporciona una ventaja funcional en términos de la visión estereoscópica. Sin embargo, el cuestionario subjetivo sugirió una ventaja potencial. La cantidad intermedia de aberración esférica mostró indicios de igualar los niveles de incomodidad entre las diferentes condiciones de conflicto, creando una situación de experiencia subjetiva más homogénea. Ciertas aplicaciones de realidad extendida con cambios dinámicos de vergencia muestran cambios constantes entre condiciones de conflicto, y algunos estudios sugieren que estas variaciones en malestar generan una peor experiencia de usuario comparado con un nivel de incomodidad constante. En este sentido, un perfil de aberración esférica podría ser una solución sencilla y barata de implementar en este tipo de dispositivos, ya sea integrada o en forma de producto externo como gafas o lentes de contacto, para reducir la fatiga en sesiones prolongadas de realidad extendida.

Además de los ejemplos de uso presentados en esta tesis, el prototipo de simulador visual binocular de óptica adaptativa con control automático de vergencia desarrollado permitirá el avance en nuevos campos de investigación que hasta ahora no han sido explorados debido a la

falta de instrumentación. La visión binocular podrá estudiarse en condiciones más realistas, proporcionando un mayor entendimiento del efecto de diferentes perfiles ópticos en la visión estereoscópica. Por otro lado, el control de vergencia independiente proporciona una herramienta para investigar el conflicto de vergencia y acomodación bajo diferentes perfiles de fase, un tipo de soluciones que no se ha explorado hasta ahora y puede tener un impacto importante en aplicaciones como la realidad extendida.

Chapter 1: Introduction

1.1. Adaptive Optics (AO)

Adaptive Optics (AO), a technology originally conceived to counteract the distorting effects of atmospheric turbulence on telescopic imaging, has undergone a remarkable evolution since its inception. Initially a concept reserved for astronomers and defense scientists, AO has since found transformative applications in biomedical imaging and vision science.

The theoretical foundations of adaptive optics were laid in the mid-20th century. In 1953, Babcock proposed the idea of a real-time optical correction system to neutralize atmospheric distortion during astronomical observations (Babcock, 1953). His proposal introduced the basic principles that still underpin modern AO systems: detect distortions with a wavefront sensor, then correct them with a wavefront shaping device. Despite its simplicity, the proposal remained impractical at the time due to technological limitations regarding wavefront sensing and manipulation.

The concept remained mostly theoretical until the 1970s and 1980s, when military interest spurred the development of operational AO systems for satellite imaging. The improvements in computing and optical fabrication brought AO to the forefront of astronomical applications, allowing telescopes to achieve near-diffraction-limited imaging from the ground which was previously only attainable through space-based instruments.

As AO matured within astronomy, its potential to correct optical imperfections in the human eye began to attract interest from vision scientists. Traditional ophthalmic instruments were limited by the eye's own optical aberrations, degrading image quality. In 1989 an AO system was used for the first time to increase the resolution of retinal imaging (Dreher, et al., 1989), and in 1997 the first demonstration of visual functions under complete correction of the eye's natural aberrations was performed (Liang, et al., 1997).

These early demonstrations marked a turning point in both ophthalmology and vision science. Adaptive optics enabled the in vivo visualization of individual photoreceptor cells, capillaries, and other fine structures in the living human eye, details that had previously been invisible using conventional instruments. Moreover, AO opened new avenues for understanding the functional architecture of the visual system, diagnosing retinal diseases at their earliest stages, and exploring the limits of human visual perception.

1.1.1. Wavefront sensing

Out of the multiple technologies capable of characterizing an incoming wavefront, the Hartmann-Shack (HS) wavefront sensor stands out due to its robustness, compactness, low-light requirements, and relatively straightforward implementation. The underlying principle was proposed by Hartmann in 1900 (Hartmann, 1900), in which light was projected through a mask with pinholes onto a screen at a known distance, creating a spot pattern. The incident angle of the light at each pinhole produces a displacement of the corresponding spot with respect to its ideal position, providing an estimate of the local slope of the wavefront. The measured spot displacements in Cartesian coordinates, Δx and Δy, can therefore be related to the local derivatives of the wavefront $W(x, y)$ using the distance between the pinhole array and the screen, D, as follows:

$$\frac{\partial W(x,y)}{\partial x} = \frac{\Delta x}{D}$$
$$\frac{\partial W(x,y)}{\partial y} = \frac{\Delta y}{D} \quad (1)$$

This concept was improved upon in 1971 by Platt and Shack (Platt & Shack, 1971), who replaced the pinhole mask with a lenslet array that focused the light onto a detector. This drastically improved light collection efficiency and allowed shorter exposure times and thus faster measurements. It also resulted in more compact sensors, as the larger numerical aperture of the lenses compared to the pinholes permitted a reduction in overall size without reaching the limit imposed by diffraction. A diagram of this implementation is shown in Figure 1.1, a configuration that has survived the test of time and has been a critical component throughout the history of adaptive optics. This innovation was incorporated into different areas, with its introduction into vision science being marked by the first reported use of a Hartmann-Shack wavefront sensor to measure aberrations in the human eye in 1994 (Liang, et al., 1994) followed by further optimization for vision science applications (Prieto, et al., 2000).

In this configuration, the focal length of the microlenses typically determines the separation between the lenslet array and the sensor, as this corresponds to the position of optimal spot focus. A longer focal length results in larger spot displacements for the same wavefront slope, thereby increasing measurement precision. As a trade-off, however, it reduces the dynamic range, since the spots may begin to overlap or cross into adjacent subapertures for smaller angular changes.

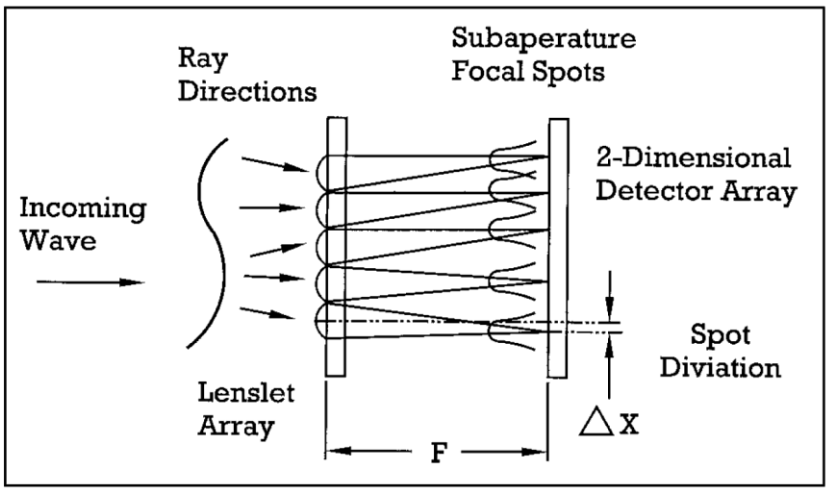


Figure 1.1 Diagram of the Hartmann-Shack wavefront sensor developed by Platt and Shack **(Platt & Shack, 1971)**. Figure adapted from **(Platt & Shack, 2001)**.

Another relevant parameter is the pitch of the lenslet array, which determines the sampling resolution. A smaller lenslet size and higher microlens density allow the slope calculation of smaller sections of the wavefront. However, reducing the lenslet size also decreases the measurement range and the intensity of the spots, potentially increasing noise. Additionally, the overall size of the lenslet array and camera sensor can be combined with telescopic magnification to increase the number of microlenses used for measurement without reducing the measurement range, as this effect is compensated by the reduction in wavefront slope introduced by the magnification.

Finally, image sensor resolution and pixel size may affect measurement precision, as they determine the smallest detectable spot displacements. Other parameters may become more relevant depending on the application, such as the transmittance of the lenslet array and the sensitivity of the camera sensor for efficient light collection, or the frame rate and shutter speed of the camera to decrease acquisition times. All these parameters must be considered when selecting the optimal Hartmann-Shack wavefront sensor to integrate into an adaptive optics system.

Local slope measurements enable a segmented reconstruction of the wavefront; however, more effective and interpretable representations are available. Among these, Zernike polynomial decomposition is widely employed across various disciplines and is particularly valuable in vision science. Originally introduced by Frits Zernike in 1934 (Zernike & Stratton, 1934) to improve the characterization of optical aberrations in astronomical mirrors, Zernike polynomials form a complete set of orthogonal and continuous functions defined over the unit circle.

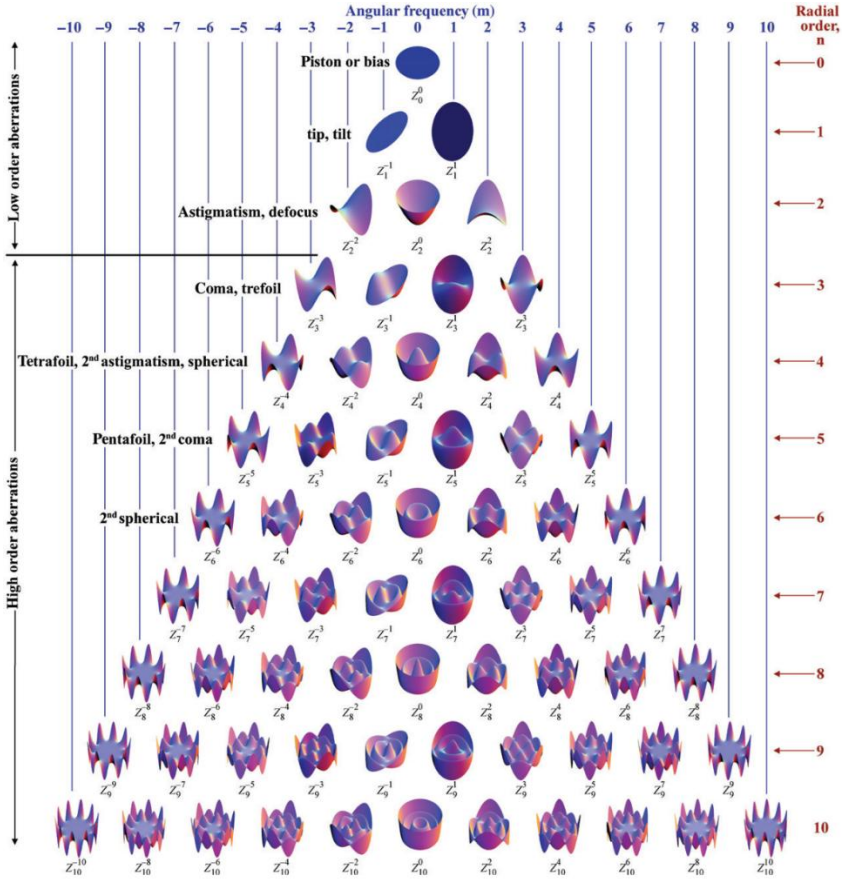


Figure 1.2. Phase representation of the first ten orders of Zernike polynomials, adapted from Lakshminarayanan and Fleck **(Lakshminarayanan & Fleck, 2011)**.

Zernike polynomials can be identified by their radial and azimuthal orders (*n* and *m*) or by the index used by the American National Standards Institute (ANSI) described by $j = (n(n+2) + l)/2$. The Zernike polynomials Z_n^m are often defined in normalized polar coordinates (r,θ) and described by:

$$\begin{aligned} Z_n^m(r,\theta) &= R_n^m(r)\cos m\theta \qquad \text{for } m \geq 0, \\ Z_n^m(r,\theta) &= R_n^m(r)\sin m\theta \qquad \text{for } m < 0, \end{aligned} \tag{2}$$

with the radial function $R_n^m(r)$ being:

$$R_n^m(r) = \sum_{l=0}^{(n-m)/2} \frac{(-1)^l (n-l)!}{l!\,((n-m)/2-l)!\,((n+m)/2-l)!} r^{n-2l} \tag{3}$$

A wavefront limited by a circular pupil can be expressed as a linear combination of Zernike polynomials:

$$W(r,\theta) = \sum_{n,m} C_n^m Z_n^m(r,\theta) \tag{4}$$

Where C_n^m represents the coefficient associated to its respective polynomial and therefore its contribution to the wavefront. The linear properties of the derivative result in the decomposition of the wavefront slope into a set of functions that maintain the Zernike coefficients necessary for the original wavefront reconstruction. With a cartesian representation of the polynomials we can relate the spot displacements to the Zernike coefficients using Equation (1) as:

$$\begin{aligned} \sum_{n,m} C_n^m \frac{\partial Z_n^m(x,y)}{\partial x} &= \frac{\Delta x}{D} \\ \sum_{n,m} C_n^m \frac{\partial Z_n^m(x,y)}{\partial y} &= \frac{\Delta \mathrm{y}}{D} \end{aligned} \tag{5}$$

Equation (5) forms a set of two linear equations per spot, with the spot displacements being the measurable quantities and the Zernike coefficients the values obtained by solving the system. One of the reasons behind the prevalence of the Zernike basis representation is that the lower-order terms correspond to the most prevalent aberrations encountered in optical systems, with the first ten orders shown in Figure 1.2. In the context of vision science, the second order is particularly significant, as it encapsulates the classical refractive errors. These include variations in optical power along orthogonal meridians, which are clinically known as defocus (associated with myopia or hyperopia) and astigmatism (defined by both magnitude and axis). These components are directly relevant to ophthalmic diagnostics and form the basis for corrective lens prescriptions.

The coefficients corresponding to the polynomials Z_3, Z_4 and Z_5 are related to certain optometric quantities: the oblique astigmatism J_{45}, spherical equivalent M, and horizontal-vertical astigmatism J_0, with the relationship being as follows:

$$J_{45} = \frac{-2\sqrt{6}}{r_0^2} z_3, \qquad M = \frac{-4\sqrt{3}}{r_0^2} z_4, \qquad J_0 = \frac{-2\sqrt{6}}{r_0^2} z_5 \tag{6}$$

where z_j (the ANSI equivalent of C_n^m) represents the coefficient associated to the corresponding polynomial in microns, r_0 represents the physical radius of the pupil in millimeters, and the optometric quantities are expressed in diopters. Another useful conversion

is to transform these quantities to the ubiquitous defocus, cylinder and axis used in clinical practice for lens prescription:

$$\text{Sphere} = M - \sqrt{J_{45}^2 + J_0^2}, \qquad \text{Cylinder} = -2\sqrt{J_{45}^2 + J_0^2}, \qquad \text{Axis} = \frac{1}{2}\tan^{-1}\frac{J_{45}}{J_0} \tag{7}$$

where defocus and cylinder are obtained in diopters and axis in degrees. While this provides a theoretical framework to translate Zernike coefficients to sphero-cylindrical refraction, it is not advisable to directly use wavefront measurements to determine the best subject correction. This is in part due to the influence of higher order aberrations, which can create a scenario where the best image correction with only sphero-cylindrical lenses is obtained for powers differing from those obtained with the Zernike coefficients. While for most eyes the influence of the lower order aberrations dominates the deviations of the wavefront, other High Order Aberrations (HOA) such as coma (Z_7 and Z_8) or spherical aberration (Z_{12}) have a stronger presence in subjects with certain pathologies (Guirao, et al., 2002).

1.1.2. Wavefront shaping

Both the Hartmann-Shack wavefront sensor and the Zernike polynomial representation were initially developed to provide more accurate characterization of phase aberrations introduced by optical components, particularly mirrors used in astronomical imaging. Although these tools were originally applied to identify and quantify mirror surface defects, it was later recognized that other disturbances such as atmospheric turbulence, which is a major source of image degradation in ground-based telescopes, could also be effectively measured and described using the same methodologies. With advances in fabrication and control technologies, mirrors could be manufactured to characterize and correct these wavefront aberrations. Specifically, the development of deformable mirrors (DMs) enabled localized control of the optical path length traversed by incoming wavefronts. This marked a significant improvement in the ability to correct dynamic aberrations, leading to substantial gains in image quality not only in astronomical applications, but also in biomedical imaging and vision science.

The first deformable mirrors developed in the early 1970s focused on the use of piezoelectric actuators that can be driven with an electric current to produce a deformation in a reflective layer placed on top. Some examples are the stacked array DMs, which use an actuator array formed by stacks of individual piezoelectric disks to push the optical surface, or bimorph DMs, which use transversal elongations and contractions to create a controlled local curvature (Madec,

2012). They provided relatively large and controlled deformations with short response times at the cost of requiring bulky and expensive control systems.

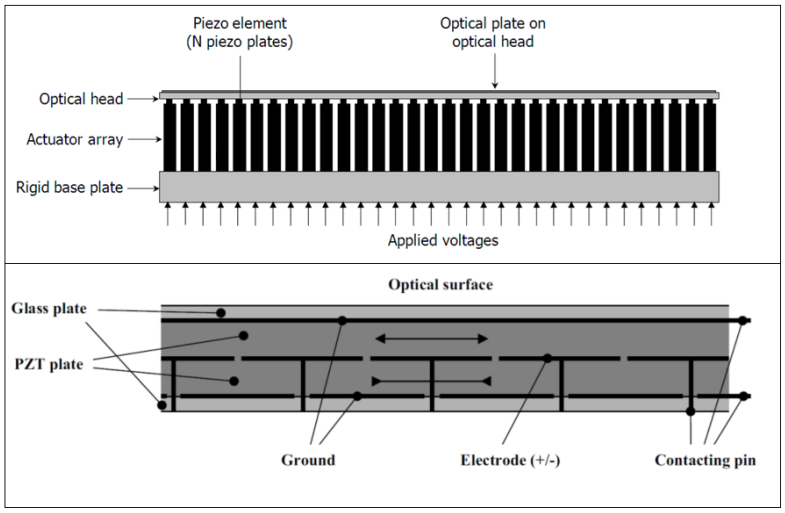


Figure 1.3. Figure adapted from **(Madec, 2012)**. Top panel shows a diagram of a stacked array DM. Bottom panel shows a diagram of a bimorph DM.

With the development of micro electro-mechanical system (MEMS) technology in the 1990s, a new generation of DMs were created with a larger number of actuators at a reduced cost (Cornelissen, et al., 2010). A thin mirror layer is attached to a flexible surface actuated by electromagnetic fields, with the manufacturing process being based on the silicon lithography process used for microchip fabrication. This allowed a more streamlined fabrication procedure, reducing production times and cost, with more compact designs, leading to a higher density of actuators.

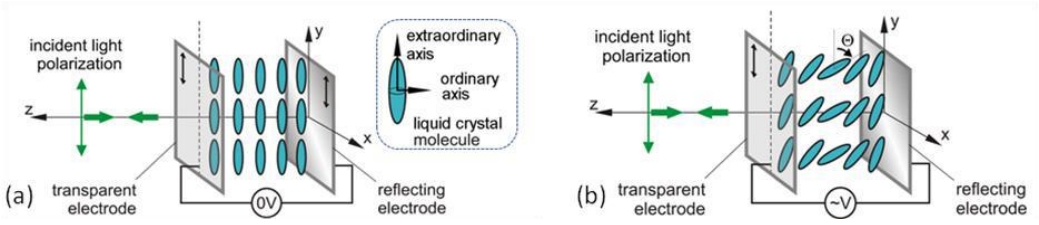


Figure 1.4. Figure adapted from **(Kujawinska, et al., 2012)**. a) and b) show the molecular orientation of the LCoS configuration without and with applied voltage respectively.

However, deformable mirrors are not the only technology capable of altering the wavefront. Liquid Crystal on Silicon (LCoS) screens have arisen as an alternative for phase modulation due to their high spatial resolution and capability of generating discontinuous phase maps. Liquid crystals presented the advantage of possessing a high birefringence index and a molecular alignment set through electric fields. This means that refractive index, and therefore phase

retardation, can be controlled for a specific light polarization. Phase control is typically segmented in cells of liquid crystal molecules with a pitch of a few microns that can be controlled through a small applied voltage (Kujawinska, et al., 2012) (Zhang, et al., 2014).

The smaller cell (or pixel) sizes coupled with the lower voltage requirements resulted in more compact devices with higher resolutions. Furthermore, advancements in LCoS technology for their use as microdisplays have resulted in lower costs for phase modulation screens based on the same principle. Another significant advantage is their capability of independent pixel control, as this enabled the introduction of discontinuous wavefronts such as diffractive phase profiles. Additionally, while traditional deformable mirrors require a continuous change of phase, LCoS screens can return from a 2π phase modulation to an equivalent off state with a singular pixel change. This phase wrapping technique increases the effective modulation range of the device when compared to other DMs. While segmented deformable mirrors exist, they typically present a much lower number of actuators than LCoS based spatial light modulators.

The main drawbacks of LCoS screens are the incident polarization requirement and overall low reflectivity reducing light efficiency, making it unsuitable for photon starved applications such as astronomy, and the relatively slow response times of the screens limiting their use in highly dynamic scenarios. While these disadvantages are very relevant for different applications, they are less important in vision science where the advantages outweigh the drawbacks.

1.1.3. AO in ophthalmology

The first application of adaptive optics elements to the human eye was achieved through its integration into a Scanning Laser Ophthalmoscope (SLO) (Dreher, et al., 1989), where a piezoelectric deformable mirror compensated a known amount of astigmatism to improve image resolution of the retina. Later studies incorporated full adaptive optics loops including wavefront sensors to further improve retinal image quality by correcting higher order aberrations (Liang, et al., 1997) (Vargas-Martín, et al., 1998). The benefits of adaptive optics were later extended to Optical Coherence Tomography (OCT), an interferometric technique that provides high axial resolution images of ocular tissues. Although OCT inherently offers excellent depth resolution, its lateral resolution is limited by the eye's optical aberrations. By integrating AO, these aberrations can be corrected, yielding high-resolution volumetric reconstructions of the retina and anterior segment (Hermann, et al., 2004).

While these first experiments were made with piezoelectric DMs (Liang, et al., 1997), MEMS based mirrors quickly gained popularity (Hofer, et al., 2001) (Doble, et al., 2002) (Fernández & Artal, 2003) (Fernández, et al., 2006). However, LCoS devices soon proved to be a very useful tool in the field of vision science. Their high fidelity enabled more stable phase modulation, often making it possible to operate in open-loop configurations without continuous feedback from a wavefront sensor (Prieto, et al., 2004). Additionally, their capability to generate discontinuous phase profiles was particularly useful to simulate complex ophthalmic optics such as multifocal or diffractive lenses (Manzanera, et al., 2007). The lower light efficiency of these devices represents a less important drawback in vision science, where sufficient illumination is typically available. Concerning the speed of the responses, it has a much smaller effect in visual simulation applications that typically present a static phase map. As a result, LCoS modulators have proven to be highly effective tools for wavefront correction and visual simulation in ophthalmic research and clinical applications (Marcos, et al., 2017).

The introduction of AO into vision science enabled a new research paradigm: the impact of aberrations on the visual process. This opened the door to investigations into the optical characteristics of the eye (Artal, et al., 2001) (Atchison, 2023), the impact of aberrations on visual performance (Marcos, et al., 2008) (Artal, 2014), the effect of neural processing on optically corrected images (Artal, et al., 2004) (H. Rouger, 2010), and the development of novel optical solutions such as intraocular lenses (IOLs) (Villegas, et al., 2020). To support such research, a class of instruments known as Adaptive Optics Visual Simulators (AOVS) was developed (Fernández, et al., 2002). These devices incorporate standard AO components, such as wavefront sensors and shapers, to control and manipulate the wavefront of the presented stimulus, while also including psychophysical testing modules to assess visual function under controlled optical conditions. The design variations and experimental applications of AOVS systems form the primary focus of the following section.

1.2. Adaptive Optics Visual Simulators (AOVS)

1.2.1. AOVS prototypes

Following the first demonstration of adaptive optics for aberration correction in the human eye by Liang et al. at the University of Rochester in 1997 (Liang, et al., 1997), several research groups worldwide began developing their own prototype systems.

One of the groups pioneering the use of adaptive optics in the human eye was the team led by Pablo Artal in the laboratory of optics in the University of Murcia. They used double-pass systems to obtain PSF images of the retina to estimate the aberrations of the eye (Artal & Guirao, 1998) before adopting Hartmann-Shack wavefront sensors and analyzing their performance for eye measurements (Prieto, et al., 2000). The addition of a deformable mirror completed the main AO elements, and they used it in a closed-loop system with the PSF retinal images to compensate aberrations (Fernández, et al., 2001). With the addition of a screen to perform psychovisual testing they coined the term Adaptive Optics Visual Simulator (AOVS), creating the first instrument that can assess visual performance under the influence of controlled aberration profiles (Fernández, et al., 2002). A schematic of this first AOVS prototype is shown in Figure 1.5.

The system was used to evaluate the limitation in aberration correction of deformable mirrors (Fernández & Artal, 2003), and a new iteration using an LCoS screen as a phase modulator was implemented (Prieto, et al., 2004). Further improvements include the implementation of a hybrid AOVS with both deformable mirror and LCoS screen (Cánovas, et al., 2010), and the inclusion of a tunable lens to increase measurement and modulation range as shown in Figure 1.6 (Suchkov, et al., 2019).

Concurrently to the developments in Murcia, continued efforts at the University of Rochester led by David Williams and Geunyoung Yoon contributed significantly to the evolution of AOVS technology (Williams, et al., 2000) (Yoon & Williams, 2002). By the late 2000s, additional research groups had successfully developed their own AOVS prototypes. Notable examples include the work of Chris Dainty at Imperial College London and later at the National University of Ireland in Galway (Dalimier, et al., 2008), Susana Marcos at the Institute of Optics (CSIC) (Marcos, et al., 2008), David Atchison at Queensland University of Technology (Atchison, et al., 2009), and John Werner at the University of California, Davis (Elliott, et al., 2009).

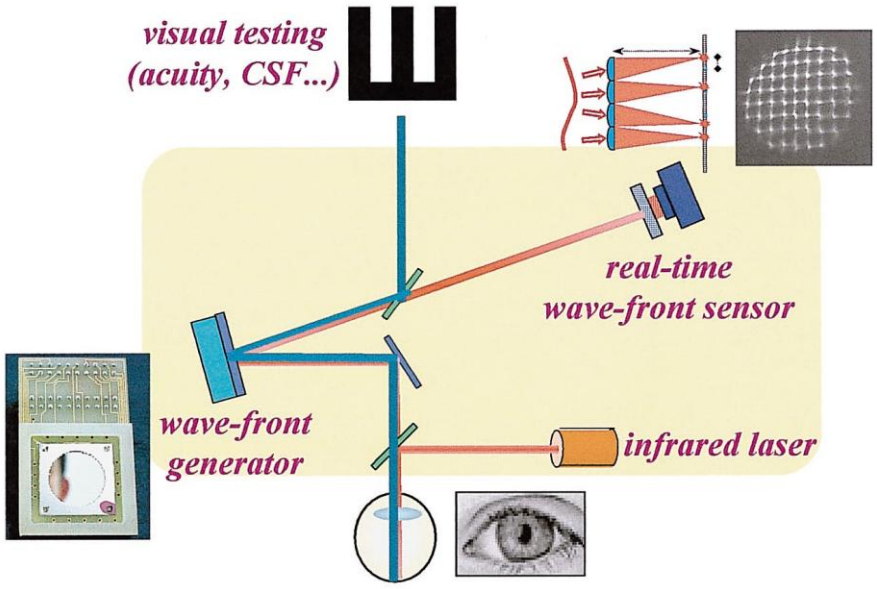


Figure 1.5. Schematic of the AOVS developed by Fernandez et al. **(Fernández, et al., 2002)**.

AOVS iterations such as those shown in Figure 1.5 and Figure 1.6 have been instrumental in advancing our understanding of how optical aberrations affect visual performance. One significant line of investigation has focused on neural compensation for ocular aberrations (Artal, et al., 2004) (Chen, et al., 2007), providing insights into the limits of retinal image quality improvements and their perceptual consequences. Chromatic effects have also been extensively studied, including wavelength-dependent changes in ocular aberrations (Fernández & Artal, 2005) and the influence of longitudinal chromatic aberration on visual performance (Artal, et al., 2010) (Suchkov, et al., 2019). AOVS systems have also facilitated the development of IOLs designed to optimize specific aberrations such as spherical aberration (Piers, et al., 2004). IOL simulation remains a prolific area of study enabled by AOVS technology (Manzanera, et al., 2007) (Marcos, et al., 2021) (Marcos, et al., 2025), offering the capability to assess lens performance prior to implantation.

Given their utility in both fundamental vision research and applied ophthalmic science, AOVS systems have transitioned into clinical tools with a device called VAO commercialized by Voptica SL in Murcia. VAO has been validated for subjective refraction measurements (Jaeken, et al., 2014) (Hervella, et al., 2019), as well as for the quantification of aberrations in both normal (Otero, et al., 2015) and keratoconic eyes (Shetty, et al., 2017). Over more than a decade of clinical use, the VAO system has supported a wide range of investigations. These include the assessment of post-LASIK aberrations (Perez, et al., 2013), comparison of different IOL designs (Jaeken, et al., 2015), and the development of novel lens models (Villegas, et al., 2020). Furthermore, the system has been used to induce controlled amounts of spherical aberration to

enhance depth of focus in presbyopic patients (Shetty, et al., 2019) (Villegas, et al., 2019) (Hervella, et al., 2020).

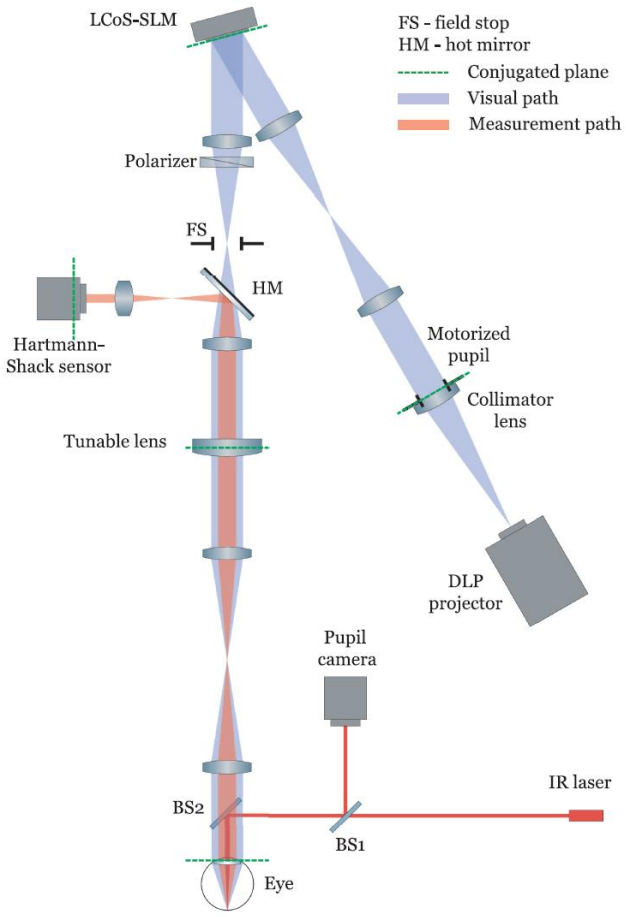


Figure 1.6. Schematic of the AOVS developed by Suchkov et al. **(Suchkov, et al., 2019)**

The impact and versatility of AOVS systems in vision science have been comprehensively reviewed in multiple articles (Fernández, 2012) (Marcos, et al., 2022). Noteworthy developments include the system by Viñas et al. (Vinas, et al., 2015), which incorporated both visible and infrared channels to investigate the effects of longitudinal chromatic aberration, and a device by Rosen et al. (Rosen, et al., 2012) specifically designed to measure peripheral aberrations. More recently, Soomro et al. (Soomro, et al., 2024) reported the development of a wearable AOVS, aimed at enhancing portability and facilitating use in clinical environments.

1.2.2. Binocular AOVS (B-AOVS)

While the adaptive optics visual simulators discussed thus far have significantly advanced visual optics research, a common limitation among these systems is their monocular design. This constraint is particularly significant, as many binocular visual functions such as stereopsis,

vergence, and binocular summation cannot be adequately investigated using independent monocular measurements. To address this limitation, some research groups have developed binocular adaptive optics visual simulators (B-AOVS) by extending and refining existing monocular designs.

One notable example was proposed by Fernandez et al. (Fernández, et al., 2009) in our laboratory. The design, shown in Figure 1.7, incorporates a single optical path shared by both eyes, significantly reducing the number of optical components by utilizing only one set of lenses, one wavefront sensor, and one phase modulator. Despite the shared optics, the system maintains the capability of aberration correction and measurement for each eye independently. A periscopic mechanism is employed to separate the optical paths and match the subject's interpupillary distance, while a Badal system extends the dynamic range for focus adjustment and aberration correction. This integrated configuration offers improved compactness, though it introduces increased alignment complexity. A limitation of the original implementation was the use of a single stimulus generator, precluding the presentation of eye-specific stimuli and thus the production of retinal disparity to simulate stereoscopic perception. This issue was addressed in subsequent iterations of the system (Fernández, et al., 2013), where two independent displays were incorporated. A periscopic arrangement was again used to optically combine the two channels while preserving pupil separation and alignment.

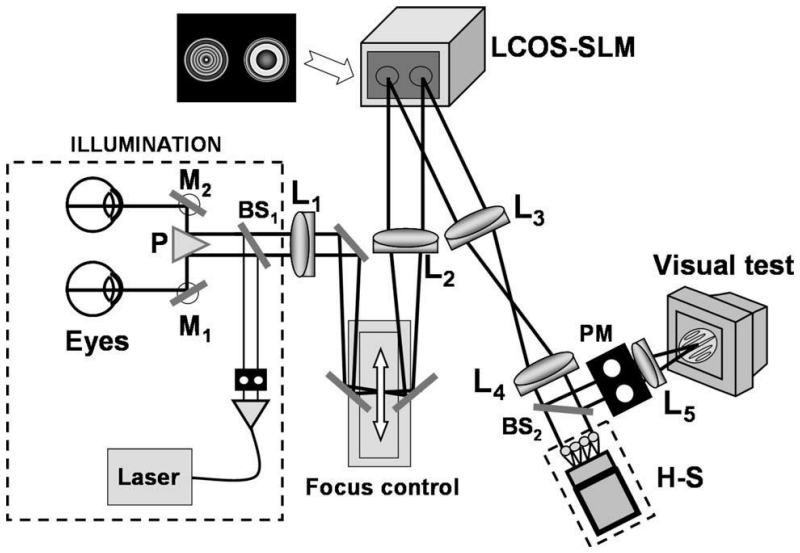


Figure 1.7. Schematic of the B-AOVS developed by Fernandez et al. **(Fernández, et al., 2009)**

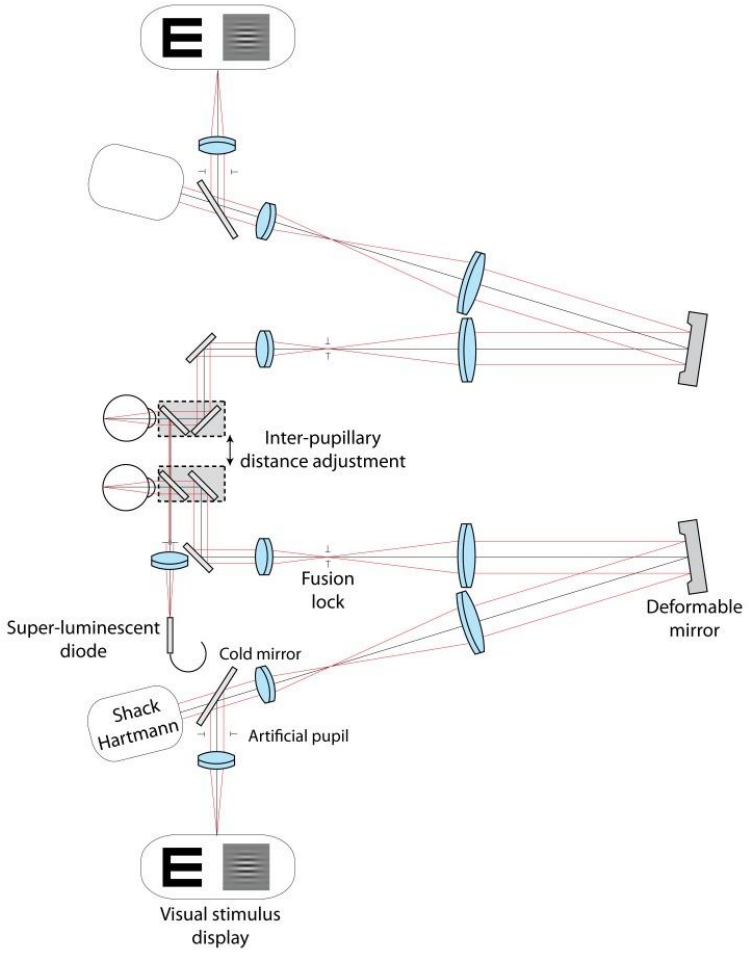


Figure 1.8. Schematic of the B-AOVS developed by Sabesan et al. **(Sabesan, et al., 2012)**

An alternative approach was the prototype developed by Sabesan et al. (Sabesan, et al., 2012), illustrated in Figure 1.8. This system consists of two independent AOVS units arranged in parallel, sharing only the laser source used for wavefront sensing. The optical components associated with each eye are fully independent, allowing eye-specific measurement and correction of aberrations. The distance between the mirrors nearest to the eyes can be adjusted to accommodate the subject's interpupillary distance (IPD), ensuring proper binocular alignment.

1.3. B-AOVS applications

One area of particular interest in both academic and clinical contexts is the binocular simulation of intraocular lenses, where different optical profiles can now be modelled independently for each eye. This capability is especially relevant for optimizing postoperative outcomes, as different focal profiles can be strategically combined to enhance depth of focus through binocular summation, thereby facilitating spectacle independence following cataract surgery.

In this regard, B-AOVS systems have been employed to simulate monovision conditions (Zheleznyak, et al., 2013), as well as to evaluate the performance of extended depth of focus IOL designs. These studies have contributed to the development of novel IOL technologies that offer improved visual quality across a range of distances (Artal, et al., 2023), while also mitigating common side effects of multifocal lenses, such as dysphotopsias (García-Pedreño, et al., 2026). Another essential component of binocular vision that can only be assessed through such simulators is stereopsis. B-AOVS prototypes have been utilized to investigate the influence of higher-order aberrations (HOAs) on stereoscopic vision (Fernández, et al., 2013), including the limitations imposed by neural adaptation mechanisms (Ng, et al., 2021).

Nevertheless, it is important to note that most of these experiments have been conducted with a fixed vergence angle. Only a few studies have attempted to manipulate convergence (Lyu, et al., 2021), primarily due to the absence of B-AOVS prototypes that allow convenient control of vergence angle. While this limitation is generally considered inconsequential for studies that only require far distance vision or for populations without accommodative ability, such as presbyopic or post-cataract surgery patients, it becomes a significant constraint in experiments aiming to replicate natural accommodation dynamics. In such cases, accurate vergence control is essential.

1.3.1. Vergence-Accommodation Conflict (VAC)

The interplay between vergence and accommodation has been a subject of scientific inquiry for over a century and is central to understanding binocular vision and the mechanisms that support three-dimensional perception. Accommodation refers to the eye's ability to change its optical power to maintain objects in focus at varying distances, while vergence denotes the coordinated movement of both eyes to ensure that images fall on corresponding retinal points.

Under natural viewing conditions these two processes are tightly linked, enabling accurate depth perception and visual comfort (Shibata, et al., 2011).

Decoupling binocular stimuli (i.e., presenting each eye with an independent input) can disrupt the natural relationship between vergence and accommodation, generating discomfort and reducing visual quality. Research investigating this dissociation has led to the characterization of several tolerance zones. These include *Panum's fusional area* (Panum, 1858), which defines the retinal disparity range within which a single fused image can still be perceived; the *zone of clear single binocular vision* (ZCSBV) (Fry, 1939), a more constrained region where the fused image remains sharp; and the *zone of comfort*, an even narrower region within which binocular viewing does not elicit discomfort (Percival, 1892) (Sheard, 1934) (Shibata, et al., 2011).

Interest in the vergence-accommodation relationship resurged during the latter half of the 20th century with the emergence of stereoscopic displays. In these systems, vergence is manipulated through binocular disparity cues, while accommodation remains fixed at the physical distance of the display. This decoupling, referred to as the *Vergence-Accommodation Conflict* (VAC), has become a significant concern, as it is considered one of the main causes of eyestrain, reduced visual performance, and perceptual fatigue during prolonged use of these devices.

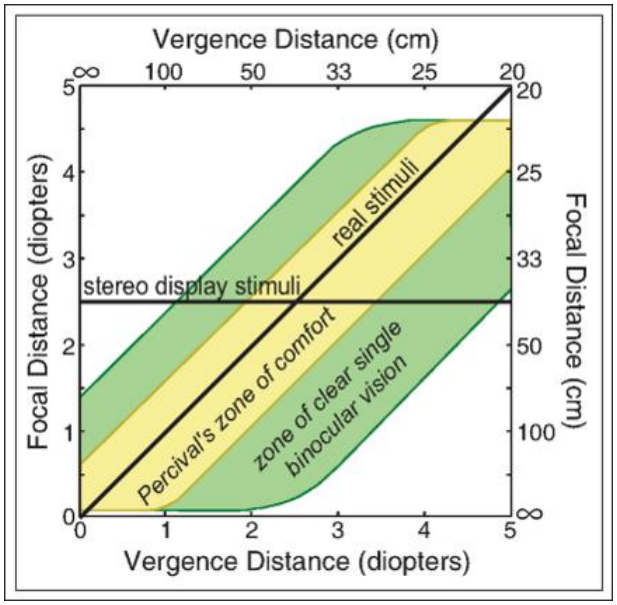


Figure 1.9. Range of vergence and accommodation responses possible and comfortable for a typical adult. Image adapted from Sabesan *et al*. **(Sabesan, et al., 2012)**.

Extended reality (ER) devices, encompassing both augmented reality (AR), where virtual content is overlaid onto the real world, and virtual reality (VR), where the entire visual field is replaced by digital imagery, have seen widespread adoption across entertainment, education, and professional applications. In these systems, VAC remains one of the primary barriers to user comfort during prolonged use (Sharples, et al., 2008) (Hoffman, et al., 2008). Numerous studies have investigated the sources and consequences of VAC-induced visual discomfort across different display technologies (Chang, et al., 2020), leading to the development of several hardware solutions intended to mitigate the problem (Kramida, 2016) (Wang & Lin, 2021).

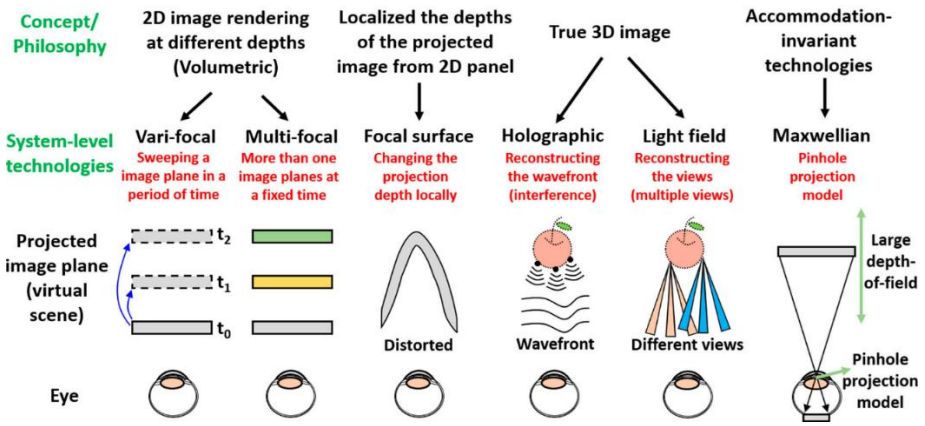


Figure 1.10. Diagram of the concepts behind different VAC solutions. Image adapted from Wang & Lin **(Wang & Lin, 2021)**.

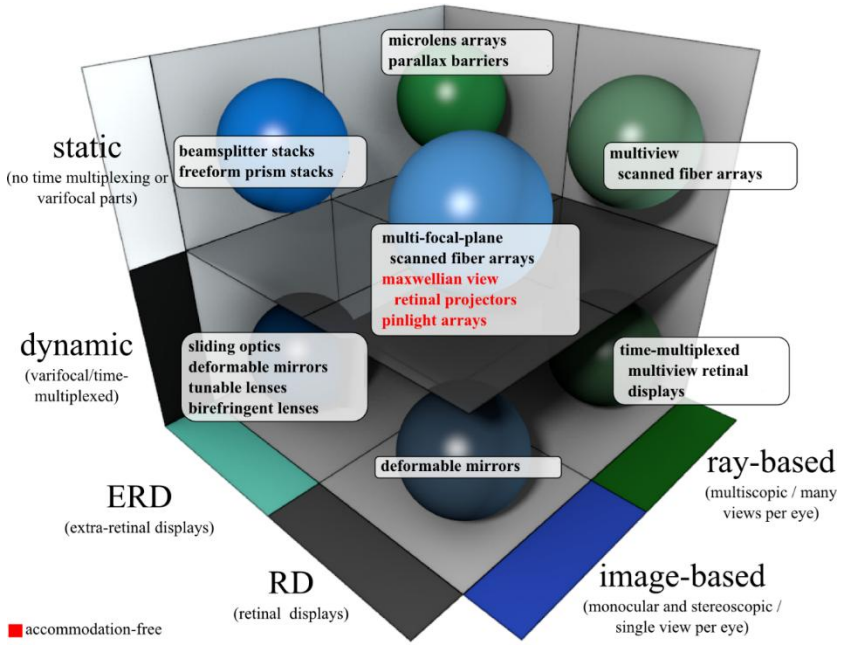


Figure 1.11. Diagram of the technologies behind different VAC solutions. Image adapted from Kramida **(Kramida, 2016)**.

Proposed approaches to address the VAC include multi-focal plane displays that present images at several discrete focal depths (Akeley, et al., 2004) (Hu & Hua, 2014), temporally multiplexed displays using tunable lenses to adjust focal distance in synchrony with visual content (Suyama, et al., 2000), and extended depth of focus systems leveraging technologies such as pinlight arrays (Maimone, et al., 2014) or Maxwellian view optics (Waldkirch, et al., 2004) (Lin, et al., 2020). While these methods show promise, each presents trade-offs. Many are complex, bulky, or cost-prohibitive, and may compromise key performance parameters such as spatial resolution, field of view, or overall visual fidelity.

Another known method for increasing the depth of focus is the inclusion of aberration-based phase profiles. While this approach is relatively common in other fields such as intraocular lens implantation (Marcos, et al., 2025), it remains a relatively unexplored option to solve the vergence-accommodation conflict. Such profiles could provide cheap and easy to implement solutions, as they could be either directly integrated into the screens of extended reality devices or added separately in the form of correction lenses. Despite the potential advantages, the lack of convenient instrumentation has limited the types of studies that can be performed to study the relationship between vergence, accommodation, and aberration-based profiles.

1.4. Objectives and purpose

The primary objective of this work was the development of a novel B-AOVS prototype incorporating an automatic vergence control system, enabling visual simulation under more realistic binocular viewing conditions. In particular, the new instrument allows the study of the effects of phase profiles at different viewing distances in subjects with normal accommodative responses, since a corresponding vergence angle is required to avoid significant visual discomfort. Additionally, the negative effects of the vergence-accommodation conflict can be investigated in a more controlled manner using the new instrument, taking advantage of its capability to independently adjust the vergence angle and accommodative distance.

In addition to the incorporation of the vergence system, which constitutes the main novelty of the new B-AOVS, several minor improvements over previous devices have also been included, while preserving the core functionalities that form the basis of binocular visual simulation: the measurement and correction of ocular aberrations; independent stimulus control for each eye, enabling stereoscopic and other binocular psychophysical testing; pupil size control within the system; and the ability to simulate complex phase profiles, including diffractive and multifocal designs.

Once the instrument was developed, an additional objective was to evaluate the validity of previous B-AOVS studies performed without vergence control. Binocular testing at different simulated distances has previously been conducted under the assumption that vergence plays no significant role in the absence of accommodative responses. Comparing measurements obtained under fixed vergence conditions with those acquired using vergence angles corresponding to the stimulus distance allows the assessment of the validity of prior studies, while also defining the vergence requirements for future experiments.

Finally, the last objective of this work was to investigate aspects of binocular vision that are now accessible due to the novel functionalities of the developed prototype, particularly the impact of aberration-based extended depth-of-focus profiles on the vergence accommodation-conflict. These profiles have been successfully employed in intraocular lens (IOL) design to increase the depth of focus experienced by users. Furthermore, although VAC remains one of the main causes of discomfort in extended reality displays, the effect of such phase profiles in this context remains largely unexplored. This is primarily due to the lack of instrumentation capable of generating complex phase profiles while simultaneously providing precise and convenient control of the vergence angle, a limitation addressed by the proposed device.

This thesis describes in detail the development and implementation of a novel B-AOVS prototype with vergence control. The following chapters outline the design specifications and component selection, the procedures for system alignment and calibration, and the experimental results obtained using the prototype developed throughout this work.

Chapter 2: Design and assembly of the B-AOVS

2.1. Optical design

The starting point for the design of the new prototype of binocular AOVS developed during this thesis is shown in the work of (Fernández, et al., 2013). This binocular adaptive optics visual simulator prototype incorporated both stimulus screens in a single optical path, sharing most optical and electronic components for both eyes. This reduces the cost and provides a more compact solution, critical features for a potential transition of the instrument from research to a commercial version.

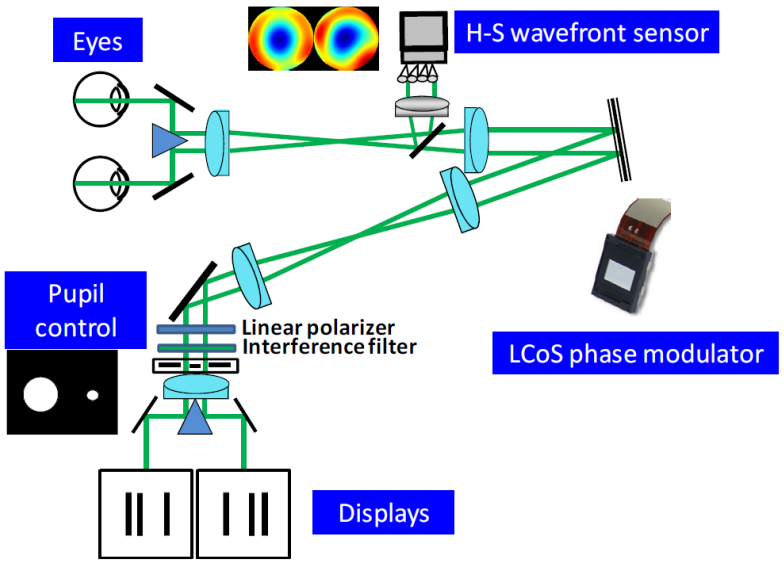


Figure 2.1. Diagram of the B-AOVS prototype developed by **(Fernández, et al., 2013)**.

The diagram of the instrument developed during this work is shown in Figure 2.2. The visual testing branch is composed of two displays for eye independent stimulus presentation, an intensity modulator for pupil size control, and a phase modulator for aberration correction and optical profile simulation. The measurement branch consists of an infrared laser and a wavefront sensor for optical aberration measurement, together with a positioning camera used to monitor subject alignment. Both branches are separated into two channels and directed toward their corresponding eyes by means of a periscopic system.

While the design philosophy remained similar to the previous B-AOVS prototype, several functionalities of the earlier iteration were improved. These included increasing the field of view of the presented stimuli through the use of higher resolution displays, as well as incorporating a tunable lens to extend the operating range of the wavefront sensing and phase modulation systems.

However, the main novelty of the newly developed instrument was the incorporation of an automatic vergence control system, allowing the study of binocular vision at different viewing distances under more realistic conditions. The periscopic system was designed to include two servomotors for controlling the angle of the visual axes and a stepper motor for adjusting interpupillary distance.

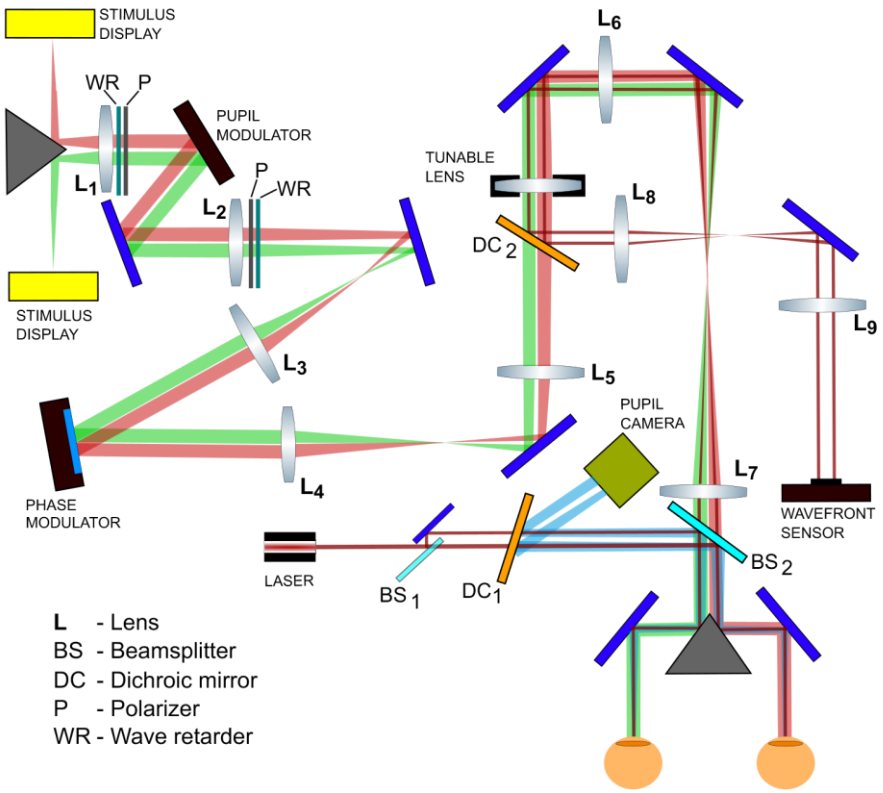


Figure 2.2. Optical diagram of the developed prototype.

The pupil planes are conjugated using telescopic systems formed by 100mm focal length lenses, as they provide relatively short focal lengths necessary to create a compact system without introducing significant aberrations. The lenses include either a visible AR coating (**L2** to **L5**, AC508-100-A, Thorlabs), a NIR AR coating (**L8** and **L9**, AC508-100-B, Thorlabs), or visible-NIR AR coating (**L6**, AC508-100-AB, Thorlabs) depending on whether they belong to the vision testing branch, measurement branch, or both. Lens **L7** has a 200mm focal length (AC508-200-AB, Thorlabs) to provide enough space to position the subject after the periscopic system, and lens **L1** has a 75mm focal length (AC254-075-A, Thorlabs) to maximize visual field while allowing high visual acuity stimuli presentation.

The binocular stimulus generation unit is formed by two LCoS micro-displays (SYL2271, Syndiant Inc) with RGB backlight LEDs, 6.4 µm pixel pitch, 0.37” panel size and 1280x720 pixel

resolution. Considering the system's magnification and collimating lens, these dimensions result in a 3.13x1.76º visual field with a resolution of 0.15 arcmin per pixel, enough to provide 0.1 logMAR steps even in the high visual acuity range.

The pupil intensity modulator is formed by an LCoS screen (SYL2282, Syndiant Inc) without backlight illumination, with 6.4µm pixel pitch, 0.55" panel size, and 1920x1080 pixel resolution. With a physical size of the screen of 12.3x6.9mm and the magnification factor of two, pupils up to 12mm can be generated in the eye plane. Two crossed polarizers are necessary for intensity generation with maximum contrast, and a half-wave plate placed before the first polarizer maximizes the intensity of the linearly polarized stimulus displays by rotating their polarization angle to match the required incident polarization. Finally, a second half-wave plate is introduced to optimize polarization for phase modulation.

Phase profiles are introduced by means of another LCoS screen (RDP551, CYOPC) with 6.3µm pixel pitch, and 1920x1080 pixel resolution corresponding to a physical size of 12.1x6.8mm, very similar to the intensity modulator. A third pupil plane contains the tunable lens (EL-16-40-TC, Optotune Switzerland AG) to introduce defocus values in a range from -2.5 to +2.5 D, both in the visual testing and measurement branches, to increase the range of refractive errors that can be measured and corrected.

The HS sensor is formed by a microlens array with 0.192mm pitch and 3.17mm focal length (APO-Q-P192-F3.17, Flexible Optical B.V.) and a camera sensor with 1.85µm pixel size and 4000x3000 pixel resolution (DMM 37UX226-ML, The Imaging Source). The sensor has a size of 7.4x5.6mm, and with the magnification it is possible to measure pupils up to 7mm in diameter. The measurement laser has a wavelength of 780nm (CPS780S, Thorlabs), and a matching bandpass filter (FBH780-10, Thorlabs) was added in front of the Hartmann-Shack to avoid potential interference from external light.

The design of the novel motorized periscope is shown in Figure 2.3, left. Vergence angle is set by rotating two mirrors (#84-444, Edmund Optics) in an automatic and controlled manner using two servo-motors (XL430-W250, ROBOTIS Co, Republic of Korea). These angular changes result in a lateral beam displacement that must be compensated to match the position of the eyes of the subject. A prism mirror (MRAK25-P01, Thorlabs Inc) displaced by a stepper motor (D8-MOTOR80, Guangzhou Fude Electronic Technology Co.) changes the position of the beams projected onto the vergence mirrors, modifying the overall distance between pupils. An example

of convergence movement is shown in Figure 2.3, right, where arrows indicate the direction of movement created by the motors.

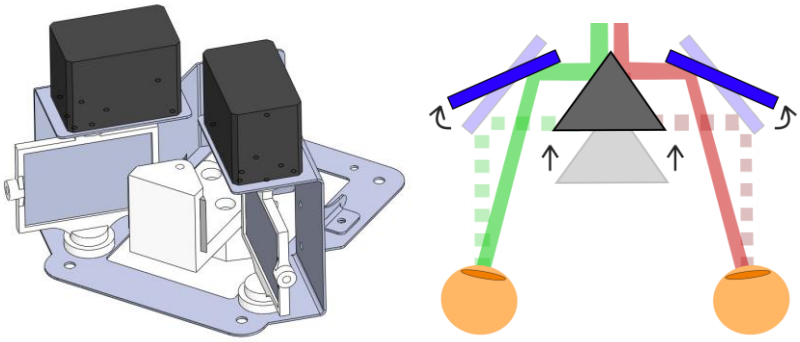


Figure 2.3. Left: 3D render of the motorized periscopic design. Right: Diagram of periscopic vergence movement.

The angular precision of the servo motors is set by their nominal 0.088º angle step with a contactless absolute encoder for precise positioning and results in an angular visual change of 0.176º or 0.62 prism diopters, which is better than the steps of one prism diopter used in typical optometric tests that assess vergence differences. The stepper motor can produce 16µm movements through a 1/16 microstepping of a nominal 250µm step motor movement. The maximum vergence angle that can be introduced is limited by the pupil displacement that can be compensated, which in turn depends on the size of the convergence mirrors. With a length for the mirrors of 35mm and a baseline angle of 45º, convergence angles up to 4D can be compensated for interpupillary distances in a range between 53 and 72mm, which are considered standard. However, since the angles necessary to induce convergence always have the same sign, the actual vergence range depends on the subject's particular pupil separation. For example, the prototype can manage subjects with IPD values as small as 38.5mm if no vergence is involved, while the convergence generation range exceeds 6.5D for subjects with more than 72mm between pupils.

2.2. Instrument alignment

2.2.1. Visual path

The protocol followed for the positioning and alignment of the visual testing branch of the prototype is described here. All lenses of the system were placed with the help of an external laser and a shear-plate interferometer to ensure that the telescopes remained afocal.

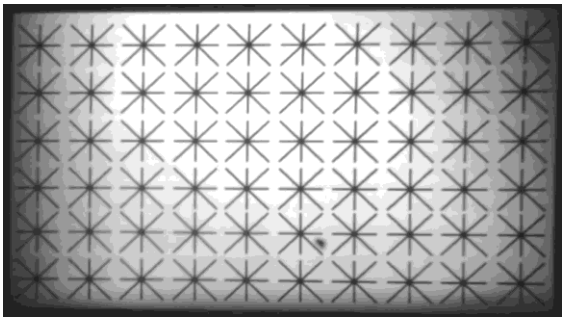


Figure 2.4. Image of one of the stimulus screens after the first collimating lens.

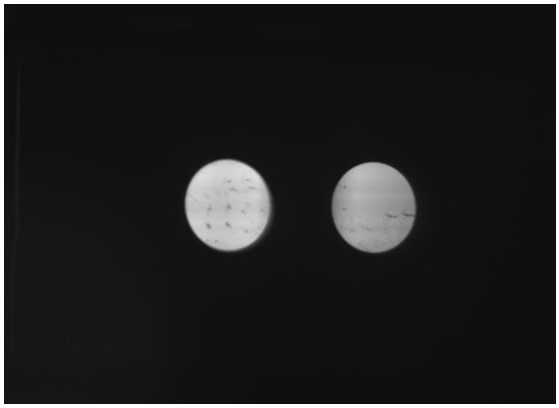


Figure 2.5. Pupils generated by the intensity modulator after its corresponding collimating lens.

The stimulus screens were positioned at the focal plane of the collimating lens **L1** by using a camera focused at infinity to obtain a sharp image as shown in Figure 2.4. The intensity modulator was placed at the focal plane of lens **L2** in a similar manner, with an example of the image obtained of the generated pupils being shown in Figure 2.5. While the phase modulator is not designed to modulate intensity, the phase wrapping transitions between a modulation of 0 and 2π can be seen as shown in Figure 2.6. This allowed its positioning with the same method placing the camera after lens **L4**. Finally, images of the tunable lens were taken with the camera after lens **L6** as seen in Figure 2.7 to check that all three pupil planes remain conjugated.

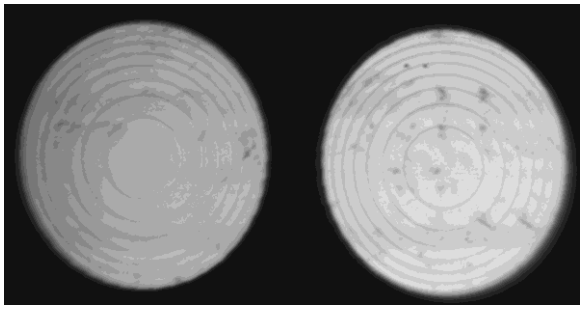


Figure 2.6. Pupils generated with the intensity modulator overlapped with the image produced by a 1D defocus generated with the phase modulator.

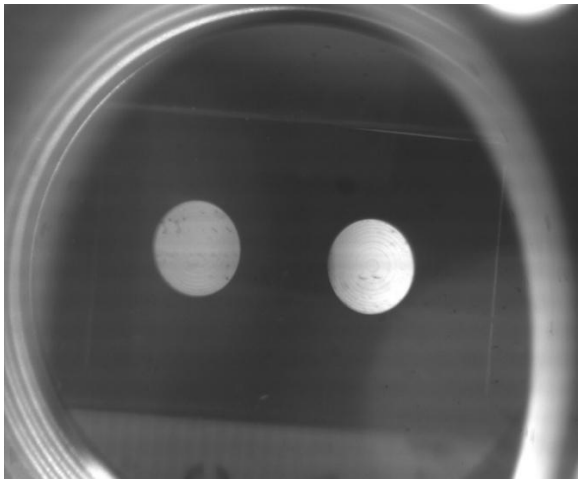


Figure 2.7. Pupils generated with the intensity modulator at the center of the tunable lens mount.

2.2.2. Measurement path

The laser was the first element of the measurement path to be aligned, being separated into two beams with a beamsplitter and a mirror and with each beam being aligned with their corresponding screen in the pupil and image planes. The beams were then shifted slightly to avoid most of the corneal reflections in future HS measurements. The final position of the beams in the image plane can be seen in Figure 2.8. These positions must be similar as the laser is still visible to the subject as a red dot, and therefore it was important to reduce disparity between the eyes to help maintain fusion and reduce discomfort during HS measurements.

Two apertures placed at the pupil plane were used as reference to reflect the measurement laser into the measurement branch and position the HS sensor. Finally, the pupil camera was positioned ensuring that the apertures remain clearly visible and properly focused.

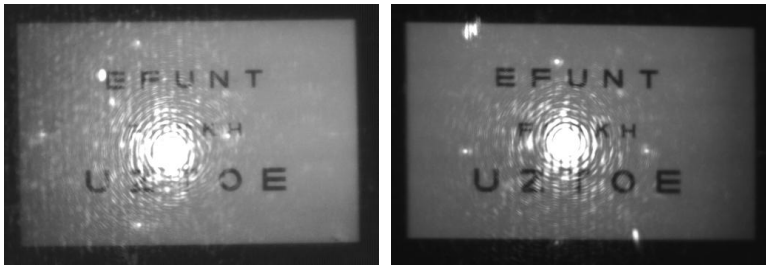


Figure 2.8. Left and right panels show the measurement laser superposed to the stimulus for the left and right eye respectively.

2.2.3. Motorized periscope

The elements of the periscopic system were fixed within its structure as seen in Figure 2.3 left, and the remaining degrees of freedom used for alignment were its overall placement and the baseline angle of the mirrors.

Two laser beams were aligned with the optical path by ensuring they remained centered with respect to their corresponding stimulus screen in both the pupil and image plane. The relative angle between the lines of sight of both channels was calibrated by measuring the distance between the laser beams at the pupil plane and at 3.12m along their path. The ruler used had a precision of 0.5mm, resulting in a 0.55 arcmin angular measurement precision. Baseline angular position of the convergence mirrors was set to maintain the beams parallel, corresponding to a vergence angle of 0 diopters and equivalent to an object located at infinity.

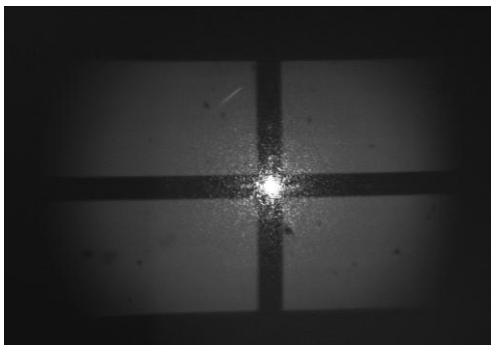


Figure 2.9. Alignment laser centered with respect to the stimulus screen image.

Beyond the baseline angle of the mirrors, the overall position of the periscope was also critical to ensure that the axis defined by the stepper motor movement coincided with the optical path. Imprecisions in periscope positioning would cause an asymmetrical pupil separation, requiring manual subject adjustment after each vergence change, and producing vignetting for large motor movements.

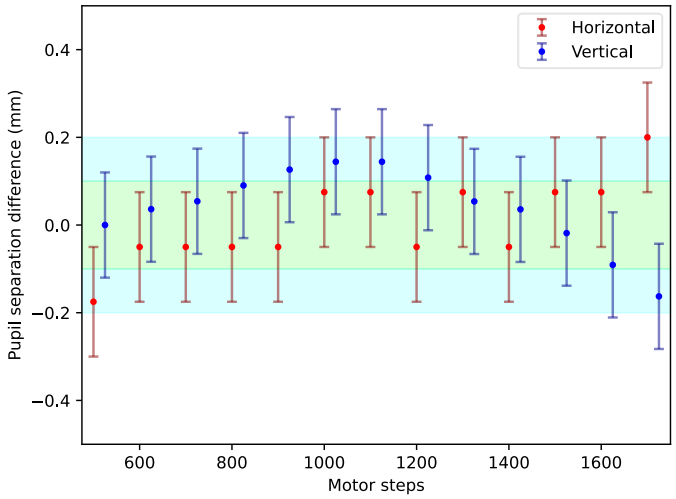


Figure 2.10. Difference in displacement for OS and OD pupils. Red and blue points represent horizontal and vertical differences respectively. Green and blue shaded regions represent differences smaller than 0.1 and 0.2mm respectively.

The change in pupil separation with prism movement was assessed by directly measuring the position of the pupils with an external camera. The differences in pupil movement, measured as OS minus OD displacement, are shown in Figure 2.10. Errors remained smaller than 0.2mm in all cases, with most differences being smaller than 0.1mm.

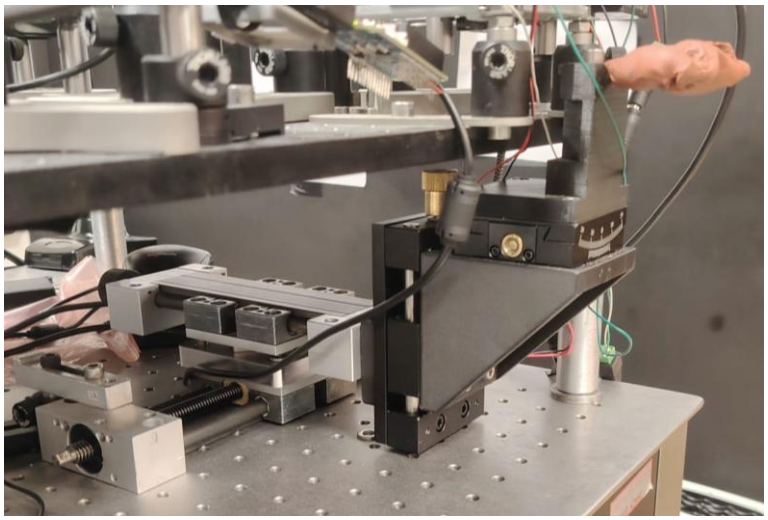


Figure 2.11. Bite bar holder including a 2D linear stage for X and Z positioning, a 1D linear stage for Y positioning, and a goniometer for tilt control.

In tandem with the motorized periscopic system, a bite bar with a positioning stage ensured that the pupils of the subject match the pupils of the device. A goniometer mount provided the necessary tilt to ensure parallel alignment between the planes defined by the subject's eyes and that of the optical system. Additionally, an XYZ translation stage enabled precise axial, lateral

and vertical adjustments. Finally, pupil separation was controlled using the motorized periscope to match it to the interpupillary distance of the subject for the baseline vergence angle of 0D. The positioning stage can be seen in Figure 2.11, and the final assembled prototype on an optical breadboard of 45x60 cm is shown in Figure 2.12.

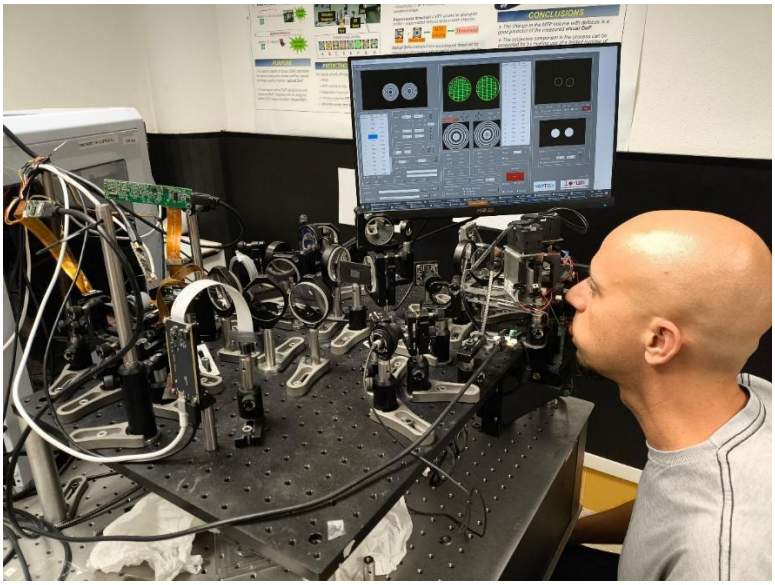


Figure 2.12. Picture of the B-AOVS prototype.

2.3. Instrument calibration

While all the steps of the alignment protocol led to a good starting point of the system, potential imprecisions could cause errors in the image quality or aberration measurement/correction. This was mitigated with a thorough calibration procedure as described in this section.

2.3.1. Intensity modulator

The intensity modulator was calibrated by measuring directly the size of the pupils generated in the eye plane to ensure that no errors are introduced. This was done by capturing an image of the pupil plane through a calibrated semi-transparent ruler of 0.1 mm precision (#30-075, Edmund Optics) with a camera, running a contour finding algorithm after binary thresholding, and finally fitting to an elliptical shape (Figure 2.13, left).

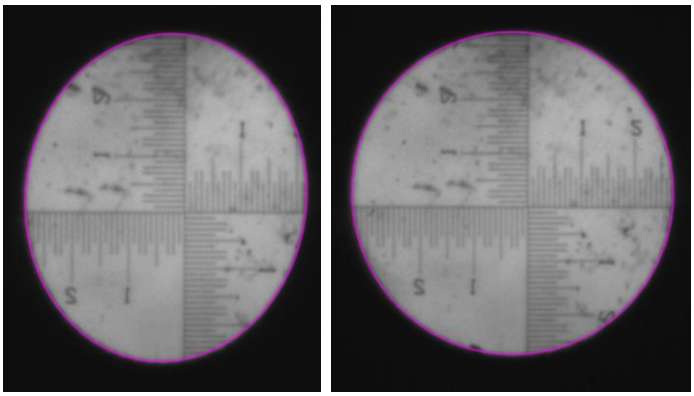


Figure 2.13. Left and right show the pupil generated by the intensity modulator before and after ellipticity correction respectively. The ruler shows distance in millimeters, and the purple outline represents the contour ellipsoidal fit.

Using the reference ruler to convert from pixels to millimeters, we obtained the values of the major and minor axes as well as their relative angle with respect to the horizontal direction. The elliptical nature of the images was the result of the relative tilt between the intensity modulator and the optical path, causing any circular pupils drawn to be projected as ellipses on the actual pupil plane.

2.3.2. Phase modulator

The phase modulator presented a similar problem as the intensity modulator, albeit less severe since its tilt angle was smaller. Its ellipticity and magnification were also calculated by using images of the pupil plane with a ruler superimposed. The elliptical fit was performed for the

outer ring of a 1 diopter defocus phase profile. The specific value of defocus is irrelevant, as the important feature is the ring pattern generated by its circular symmetry. An example of both the original contour fit and the ideal pupil size is shown in Figure 2.14, left. After correcting the phase map created by the LCOS, we obtained the fit shown in Figure 2.14, right. The major axis was measured to be 6.01mm and the minor axis 5.96mm.

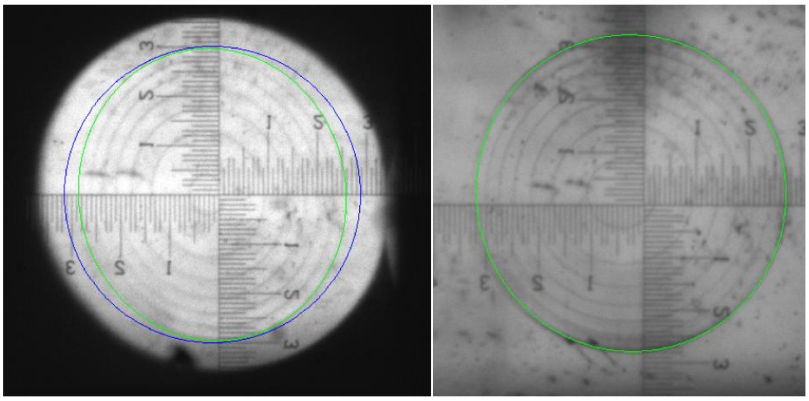


Figure 2.14. Left and right show the phase map generated before and after ellipticity correction respectively. The ruler shows distance in mm, the green outline represents the contour ellipsoidal fit and the blue outline represents the ideal pupil.

Finally, a small rotation in the placement of the phase modulator can cause a difference between its internal axes and the external XY reference. To test this, we introduced an astigmatism at 0 degrees in the phase modulator, which creates defined elliptical shapes with a major axis ideally along the horizontal direction. We measured a 1.6º rotation of the main axis, which was corrected digitally by rotating in the opposite direction the phase maps sent to the phase modulator.

2.3.3. Stimulus screen

The angular size of the stimulus presented is critical for the different visual tests that can be performed. To calibrate this, we used an external camera to capture an image of a letter E presented by one of the stimulus displays. The stimulus was generated with a 24-pixel size stroke and the measurement yielded a final angular size of 3.78 arcmin, resulting in a pixel size of 0.158 arcmin.

Another essential consideration for visual tests is the optical image quality of the stimuli, which could be potentially degraded by aberrations introduced by the system. A protocol to optimize image quality using the phase modulator was developed, where the Zernike coefficients

from orders 2 to 4 were iteratively changed to optimize image sharpness using the Tenenbaum gradient as a focus metric (Krotkov, 1988).

These iterative changes started with a coarse search with changes of 0.05µm in a range of -0.5 to 0.5µm for all coefficients in a 6mm pupil, followed by a fine search in steps of 0.01µm. We repeated this independently for each screen, as they follow independent optical paths within the optical system and therefore can present slightly different aberrations, and the results can be seen in Table 2.1.

	z3	z4	z5	z6	z7	z8	z9	z10	z11	z12	z13	z14
OD	-0.01	0.03	-0.10	0.00	0.05	0.01	0.00	0.00	0.00	0.00	0.00	0.00
OS	-0.14	0.00	0.10	0.00	-0.14	-0.14	0.00	0.00	-0.12	0.00	0.10	0.00

Table 2.1. Baseline aberration correction of the right and left eyes. All coefficients are expressed in microns for a 6mm pupil diameter.

2.3.4. Hartmann-Shack sensor

A reference image of an incident plane wavefront was used to compensate for the internal aberrations of the system, as the processing algorithm subtracts the reference Zernike coefficients from the final measured wavefront. This image was acquired by introducing an external laser with the same wavelength and through the same optical path as the measurement laser. This was performed in two steps, one for the optical path of each eye, and both images were spliced together into one final reference as shown in Figure 2.15.

On the other hand, measurements on a series of trial lenses were used to calibrate the distance between the microlens array and the camera sensor, termed effective focal length, by comparing the experimental defocus values with the nominal power of the lenses. The trial lenses had a range of powers between -10D to +10D and were placed at the LCOS plane and illuminated with the external laser. The images were processed and the series of defocus values obtained fitted to a non-linear equation:

$$Sph = a + \frac{b}{c - 1/P} \tag{8}$$

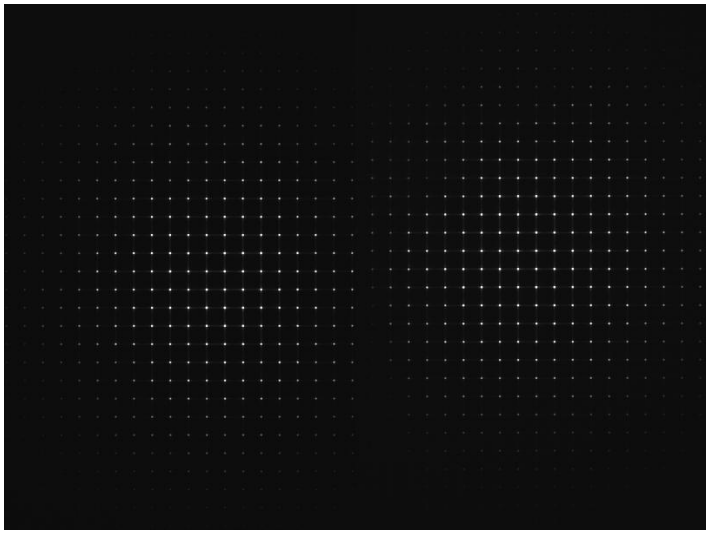


Figure 2.15. Composite image of the infrared alignment laser in the Hartmann-Shack from both the OD and OS optical paths.

Where *P* is the nominal value of the trial lens in diopters, *Sph* is the measured defocus in diopters and *a, b* and *c* are free parameters of the fit. Parameter *a* represents (in diopters) an overall bias of the system that should be compensated by the reference image. Parameter *c* represents a displacement between the optical planes determined by the HS and the position of the trial lenses, which can be compensated with the software if needed. Parameter *b* is a proportionality factor between the optical power of the trial lenses and the measured values in the HS sensor. This value can be used to recalculate the distance between the microlens array and sensor used for measurement processing.

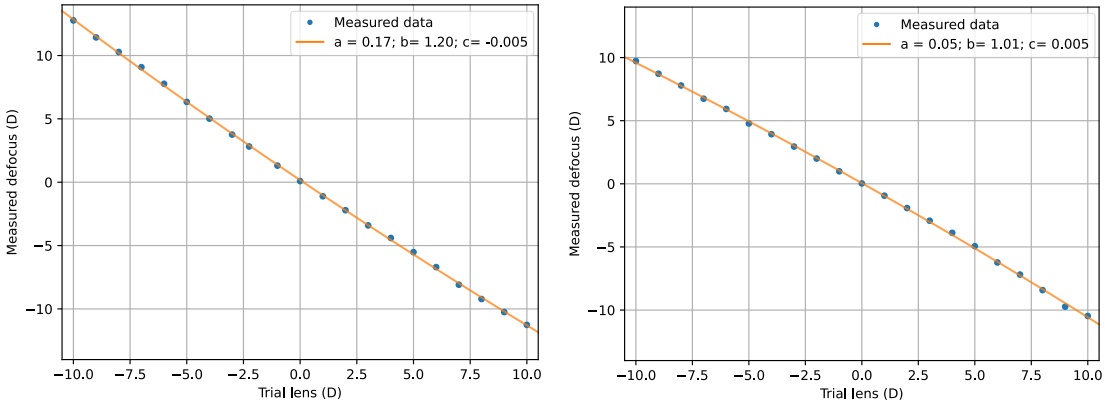


Figure 2.16. Measured defocus of trial lenses. Measured values are shown in blue, the fit in orange, X-axis and Y-axis represent the nominal and measured defocus values, respectively. Left and right show measurements before and after effective focal length correction respectively.

The calibrating measurement is shown in Figure 2.16, left, with the resulting coefficients being a = 0.17, b = 1.20, c = -0.005. The proportionality factor b was used to change the focal length from the nominal 3.12mm to an effective value of 3.76mm which was used to process a new set of measurements. The results can be seen in Figure 2.16, right, with the final coefficients of the fit being a = 0.05, b = 1.01, c = 0.005 where all parameters remained similar to their ideal values.

2.3.5. Tunable lens

Some of the optical aberrations introduced by the tunable lens had already been compensated with the phase modulator in previous steps. However, the main functionality of introducing defocus of the tunable lens needed to be verified and calibrated.

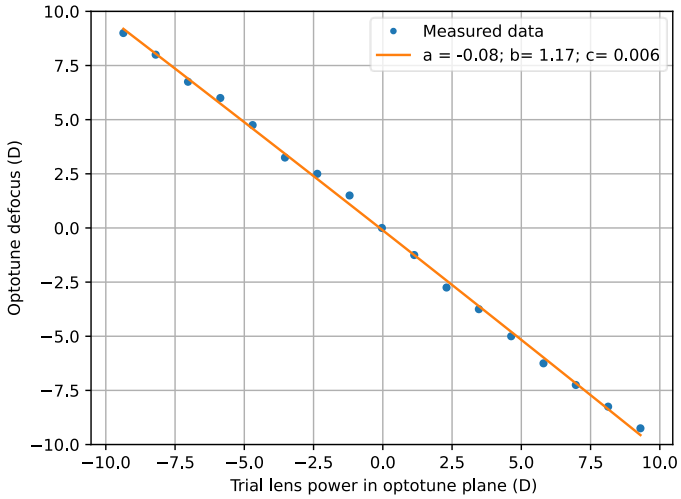


Figure 2.17. Defocus induced by the tunable lens to compensate trial lenses. Color scheme and axis are the same as in previous figures.

The protocol consisted in compensating with the tunable lens the power introduced by a series of trial lenses using an external laser to reach the Hartmann-Shack sensor. In other words, for each trial lens the nominal power of the tunable lens was iteratively changed to minimize the measured defocus in the HS sensor. This was repeated for trial lenses in a range of -2.25D to 2.25D in steps of 0.25D. Due to the magnification, the expected effective power of the lenses in the tunable lens plane was four times bigger than the eye's pupil plane where the lenses were located. The results are shown in Figure 2.17 where a fit to Equation (8) yields coefficients of a = -0.08, b = 1.17, c = 0.006. Parameters a and c remained small and similar to their ideal values, while parameter b was more similar to the pre-corrected Hartmann-Shack value. This parameter

was incorporated into the software to ensure that the final defocus introduced by the tunable lens is correct.

2.3.6. Positioning camera

The pixel size of the positioning camera in the pupil plane was obtained by acquiring an image of a ruler in the pupil plane for both eyes, with the resulting value being 33.38 ± 0.18 pix/mm. This was critical for pupil size estimation and to track the position of the subject.

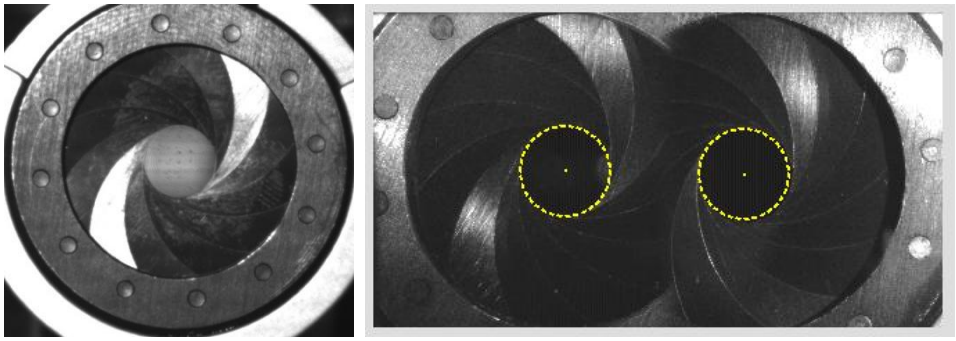


Figure 2.18. Left, aperture as seen by the calibration camera, centered with the pupil of the system. Right, both apertures as seen by the positioning camera with overlapping digital circular markers.

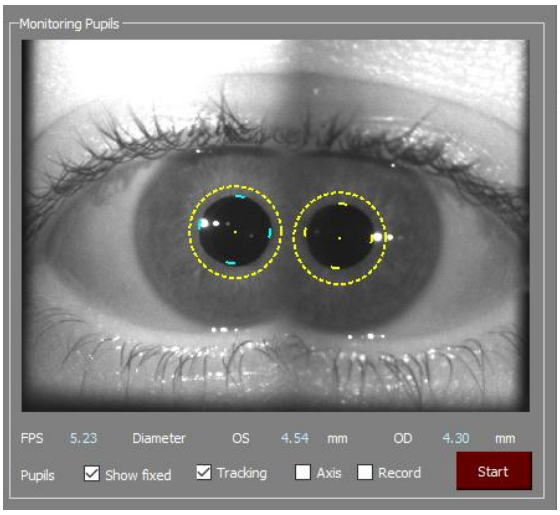


Figure 2.19. Image of the positioning camera. Subject's pupils are positioned within the calibrated dashed yellow circles, and the pupil tracking shows the estimated position and size of the right and left eye with a blue and yellow outline respectively.

The protocol designed to calibrate the eyes' position started by placing apertures at the same location as the pupils generated by the intensity modulator as shown in Figure 2.18, left. The recorded coordinates of the apertures in the positioning camera are used to draw reference circles necessary for subject placement. An example of the reference circles is shown in Figure

2.18, right. Gain and exposure time were optimized to have a clear image of real eyes, necessary for accurate pupil tracking as seen in Figure 2.19.

2.3.7. Motorized periscope

The calibration of the motorized periscope is important to ensure that vergence control functions properly. The periscope includes two types of motors: servo motors to control the angular changes and a stepper motor to set the interpupillary distance.

The behavior of the servo motors was initially assessed with their own control software (Dynamixel by ROBOTIS Co), as it has an interface with real time readings of the internal positional sensors of the system. Examples of the readings are shown in Figure 2.20, left. Internal motor parameters were manually adjusted until the feedback of the internal sensors showed no oscillations as shown in Figure 2.20, right.

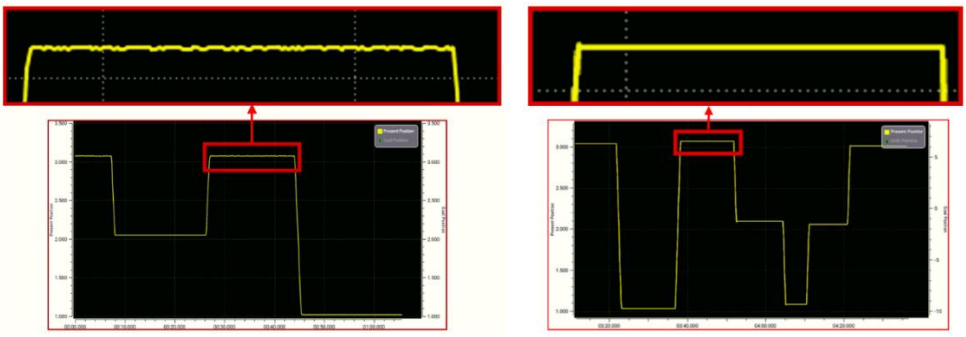


Figure 2.20. Registered servo motor position with a close-up image of the region with no induced changes. Left and right correspond to before and after the adjustment of motor parameters.

The nominal angles introduced by the motors were validated by measuring at 127.5cm the displacement of a laser reflected by the convergence mirrors. Single-step rotations showed larger angular deviations over the expected final position when compared to larger angular movements, possibly due to deformations introduced in the mirror mount with smaller torques. For this reason, we developed a two-movement protocol to avoid performing small movements, consisting of initially exceeding target position by 10 steps followed by a second movement covering the remaining angle. This 10-step movement protocol created a consistent final rotation, independent of the starting position.

The results of a single-step movement and the 10-step movement protocol are shown in Figure 2.21. Both protocols started in the same position and three series of five consecutive angular displacements of 0.09º, equivalent to one motor step, were performed. The 10-step

protocol removed the initial error introduced by single-step movements, reducing the maximum error between expected and measured movement from 0.096º to 0.026º.

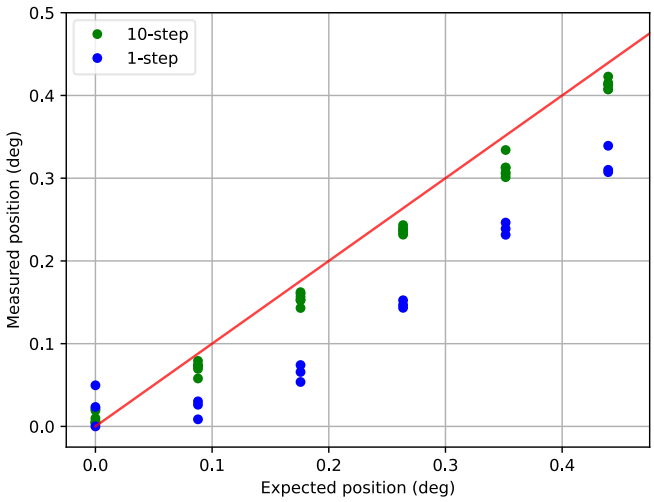


Figure 2.21. Blue and green data points show the single-step and 10-step protocol respectively. X and Y axis represent the nominal displacement of the motors and the measured displacement with respect to the origin respectively.

Concerning the stepper motor, its movements were calibrated using a camera to detect the edge of a plastic base attached to a rotating screw as shown in Figure 2.22. The displacements measured are shown in Figure 2.23, left. Three sets of measurements were performed starting from the same location and performing ten motor movements of 200 microsteps each, and a linear regression fit provided a microstep size of 8.03 µm.

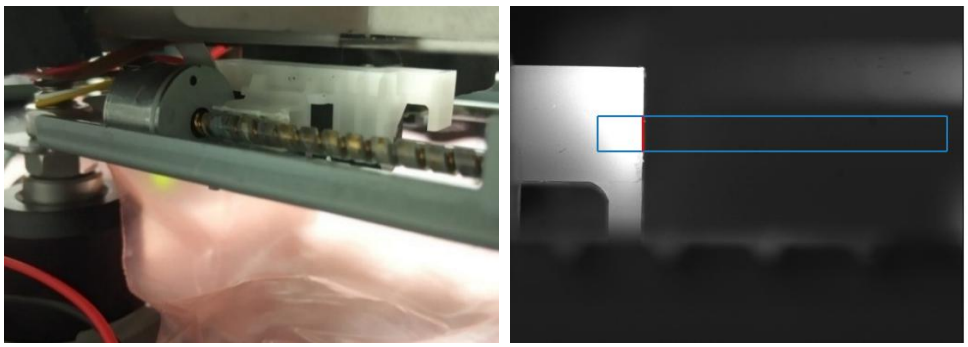


Figure 2.22. Left, picture of the stepper motor including the attached rotating screw which induced a translating movement for the white plastic mount. Right, software edge detection of the mount as represented in red versus the full range of measurement represented by the blue rectangle.

These measurements were repeated after the inclusion of the prism mirror mounted on top of the plastic base. As shown in Figure 2.23, right, errors between measured and expected

displacement (based on the calibration obtained in Figure 2.23, left) were strictly smaller than 0.025mm, which is bigger than the nominal microstep size of 0.008mm but smaller than our precision target of 0.1mm. This precision was achieved by adjusting the internal parameters of the motor to optimize precision, iterating over the prism mount design to improve weight distribution, and adding a homing protocol to provide an accurate starting point position.

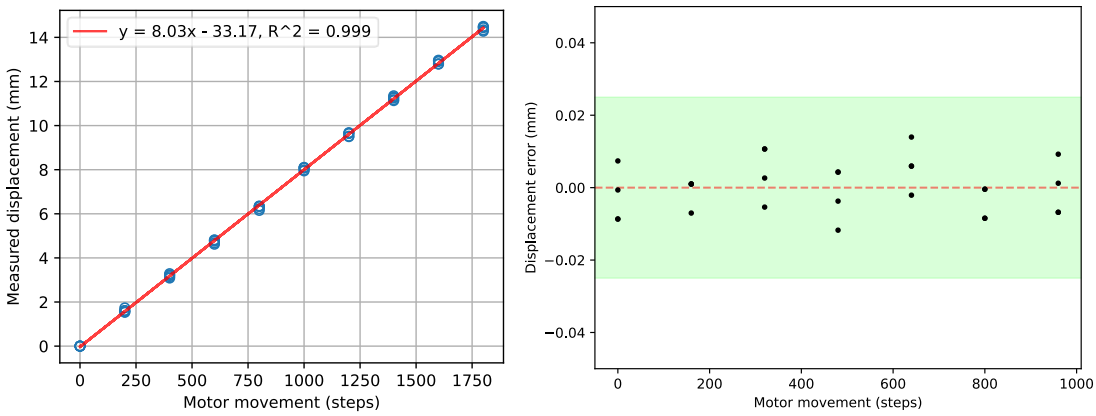


Figure 2.23. Left, Stepper motor calibration measurement. Blue circles show measured displacement and the red line the linear regression. Slope and intercept are expressed in microns. Right, difference between expected and measured positions for different displacements after homing protocol. The shaded green region represents differences smaller than 0.025mm.

These two calibration procedures for the standalone periscope helped to fix potential sources of errors and develop adequate movement protocols for the motors. However, the final calibration to relate step movement of the motors to distances was performed after alignment to ensure a direct relationship to the optical path of the system.

A camera focused at the pupil plane captured the movement of the pupils, and the displacement was measured by placing a transparent ruler in the same plane. The results are shown in Figure 2.24, where the linear regression yielded pupil displacement values of 9.2 and 9.4µm per microstep for the right and left pupil respectively. The differences with the nominal motor microstep size of 8µm were a result of the position of the convergence mirrors differing from 45º to compensate optical tilt of the system. The values obtained are consistent with mirror angles of 41 and 40.5 degrees respectively.

An asymmetry can be observed in the data, where the left eye is being displaced 0.75mm more than the right eye across the 25mm range of interpupillary distance change. This difference does not affect the final interpupillary distance set, as each pupil displacement was calibrated

independently. However, in theory this would require a lateral displacement of the subject to match the final pupils. In practice the largest difference only occurs for a large vergence change and for a subject with large interpupillary distance and would require a 0.375mm displacement to be compensated.

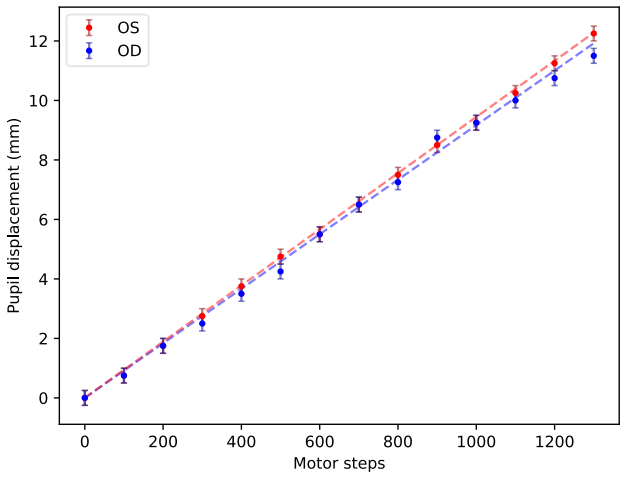


Figure 2.24. Pupil separation measurements. Red and blue represent left and right eye respectively, and dashed lines represent the linear regression fit. X axis shows the expected overall distance while Y axis shows the actual measured separation with respect to the smallest pupil separation distance.

As a final test, we set the interpupillary distance to 62mm and introduced all parameters to automatically calculate the necessary angle required for a specific object distance as well as the interpupillary distance compensation. These two movements should cancel each other and result in pupils that remain stationary. We measured the final pupil positions for different convergence values, with the results shown in Figure 2.25. Most data points remain around the expected position within only 0.25mm difference, which is the measurement precision of the ruler used. Only a few points show changes of 0.5mm, and only for the largest possible vergence settings. This indicates that both systems are working properly and that the pupil displacement introduced by the vergence angle is being properly compensated by the stepper motor automatically.

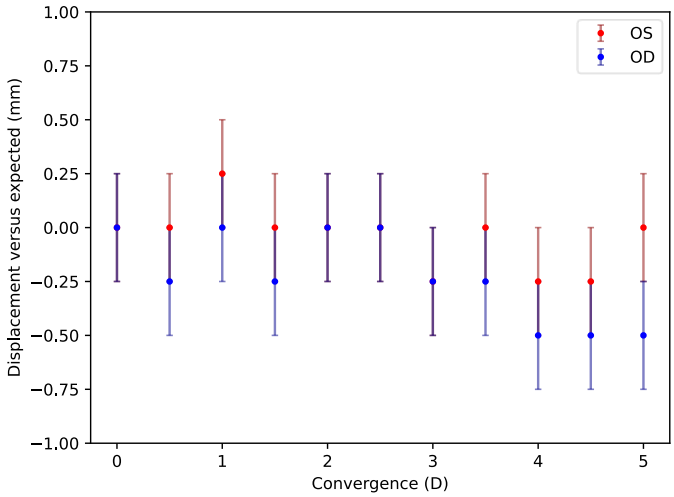


Figure 2.25. Pupil position as a function of induced convergence angle. Red and blue represent left and right pupils respectively. Y axis shows the displacement of the pupil with respect to the expected position while the X axis shows the convergence angle induced in diopters. Error bars represent measurement precision.

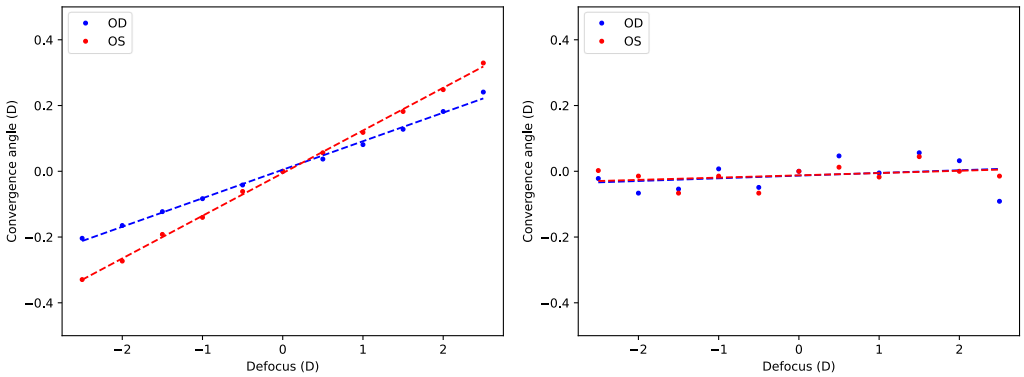


Figure 2.26. Angle induced as a function of defocus introduced by the tunable lens. X axis shows defocus, Y axis shows angular changes in terms of the equivalent vergence distance for a subject with 62mm interpupillary distance, dashed lines represent linear regression fits. Left and right correspond to measurements before and after applying the correction.

An additional consideration was the influence of the tunable lens on vergence angle. The slight decentration of each pupil over the tunable lens that naturally arises from fitting both pupils into a single optical path causes prismatic effects that result in small angular tilts dependent on induced defocus that affect convergence. The measurements of the angles created by the defocus introduced with the tunable lens are shown in Figure 2.26, left, where the induced angle is in this case expressed in terms of its corresponding vergence distance for an average 62mm interpupillary distance subject. A linear regression fit provided the parameters required to compensate for this effect, with measurements after calibration showing good accuracy as seen in Figure 2.26, right.

2.4. Instrument validation

A validation protocol was necessary to ensure that the calibration protocol resulted in adequate measurements. We developed different methods to assess wavefront sensing, stimulus generation, and phase modulation using an artificial eye and a calibration camera.

2.4.1. Wavefront sensing

We developed a simple implementation of an artificial eye to test the objective aberration measurements of the device. This eye consisted of three main components: A 30mm focal length achromatic lens (AC254-030-AB, Thorlabs); a 3D printed, one-inch diameter and 1mm thickness disc acted as a retina; and a tube that encased both elements, separated the lens and the retina 20.82mm and incorporated a 5mm diameter aperture to simulate a pupil.

This position of the retina was set by design to create a 0.8 diopter defocus, as this matched the amount subtracted by the software to compensate the effect of chromatic aberration between 780nm infrared used by the measurement laser and the center of the visible spectrum in human eyes. A 3D mount was printed to hold the artificial eye and included a trial lens holder in front of the aperture. A render of a cross-section of the artificial eye is shown in Figure2.27, left and an image of the eye is shown in Figure 2.27, right. Finally, a small vibrating disc was introduced behind the retina, which was allowed to move within a short space. This breaks coherence, as a completely static artificial eye produced speckle that affected the spot quality in the Hartmann-Shack as seen in Figure 2.28.

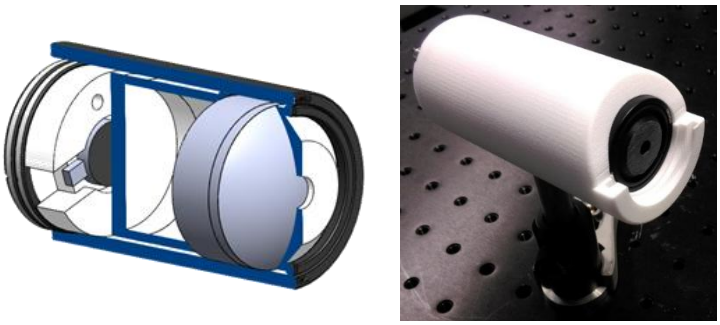


Figure 2.27. Left, render of the artificial eye including aperture, lens, retina, and vibrating disc. Right, physical implementation including the trial lens holder.

With the artificial eye fixed at the calibrated pupil position of the system, validation was performed with a procedure similar to the one described in section 2.3.4 where defocus was measured with different trial lenses placed at the lens holder and the results were fit to the Equation (8) described in that same section. The values of the proportionality factor for the left

and right eye were 0.995 and 1.004 respectively. The difference between the defocus measured and the nominal trial lens value is shown in Figure 2.29, where most differences remain within a ±0.25D range and only two cases, for large values of defocus, exceed the ±0.5D range.

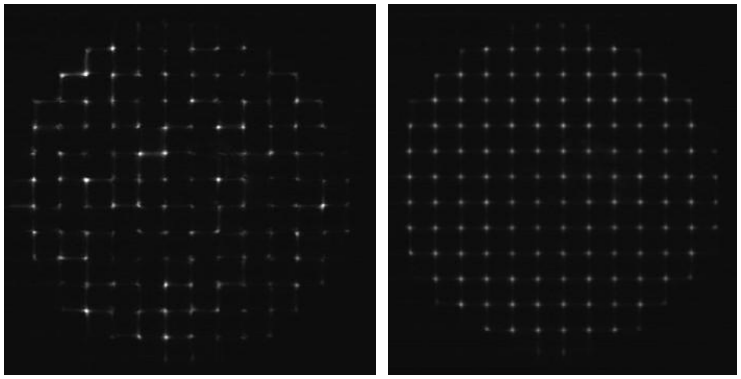


Figure 2.28. Left and right depict the Hartmann-Shack images of the artificial eye without and with vibration respectively.

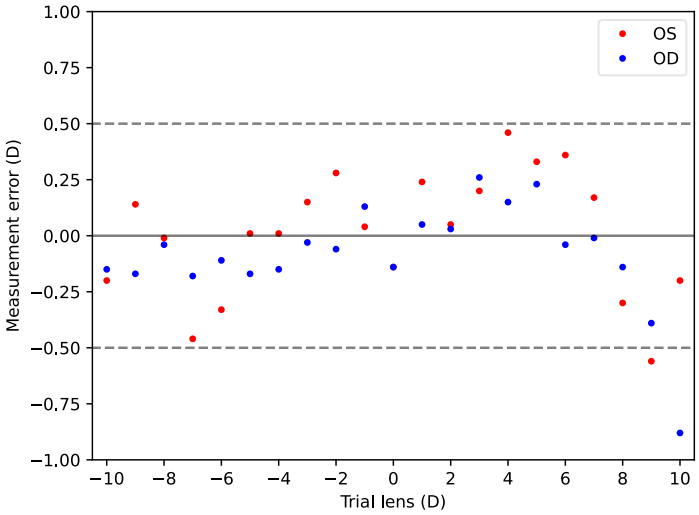


Figure 2.29. Defocus measurements with an artificial eye and trial lenses. Y axis represents the difference between the nominal lens power and the defocus measured with the HS sensor. Red and blue dots are the values for left and right eye respectively.

2.4.2. Stimulus generation

To validate the visual stimuli shown with the B-AOVS, the image quality of both of its screens was compared to the one presented by VAO. We compared the image size of a letter chart shown by both devices, as visual acuity tests are one of the most common tests performed with monocular adaptive optics visual simulators. An image of a Snellen chart with three different letter sizes was captured with an external camera for VAO and both stimulus screens of the B-AOVS as seen in Figure 2.30.

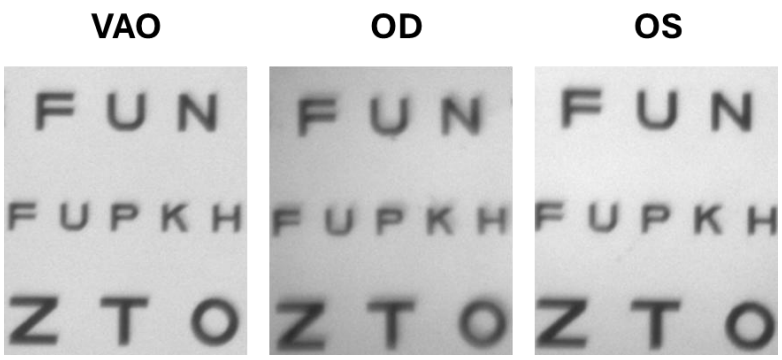


Figure 2.30. Close up images of a Snellen chart from VAO and the right and left displays of the B-AOVS captured with an external camera. Letter size corresponds to a decimal visual acuity of 0.7, 1, and 0.55 from top to bottom.

	VAO	OD	OS
VA 0.55	34.4	34.2	34.8
VA 0.7	26.8	26.8	27.4
VA 1	18.8	18.8	19.2

Table 2.2. Stroke size measurement in units of camera pixels for VAO and both screens of the B-AOVS. Visual acuity is expressed in decimal.

The stroke size of each letter was measured on the recorded images by first creating a threshold between the white and black background and then measuring the number of pixels in a horizontal or vertical stroke for each letter. An average of all the letters corresponding to the same visual acuity and stimulus screen was performed, and the results are shown in Table 2.2. The differences across displays are smaller than one pixel in all cases, validating our previous pixel size calibration.

2.4.3. Phase modulation

To validate the behavior of the phase modulator, a set of images with 1 decimal visual acuity letters were obtained for different defocus values in VAO and both screens of the B-AOVS. To test more complex phase profiles, a similar set of images were obtained while simulating a bifocal profile with 0 and 3 diopters foci in a 50/50 energy distribution. All sets of images are shown in Figure 2.31, where the screens remain qualitatively similar across all conditions.

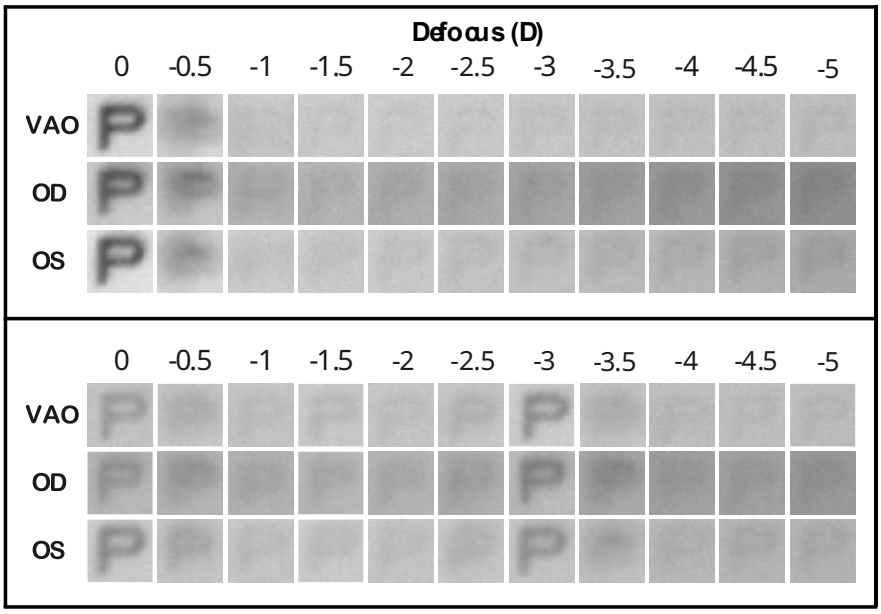


Figure 2.31. Top panel: Images of a letter corresponding to VA 1 decimal, as a function of defocus added with the phase modulator in VAO (top row) and B-AOVS right (central row) and left (bottom row) channels. Bottom panel: Images of the same letter and added defocus combined with a bifocal diffractive profile.

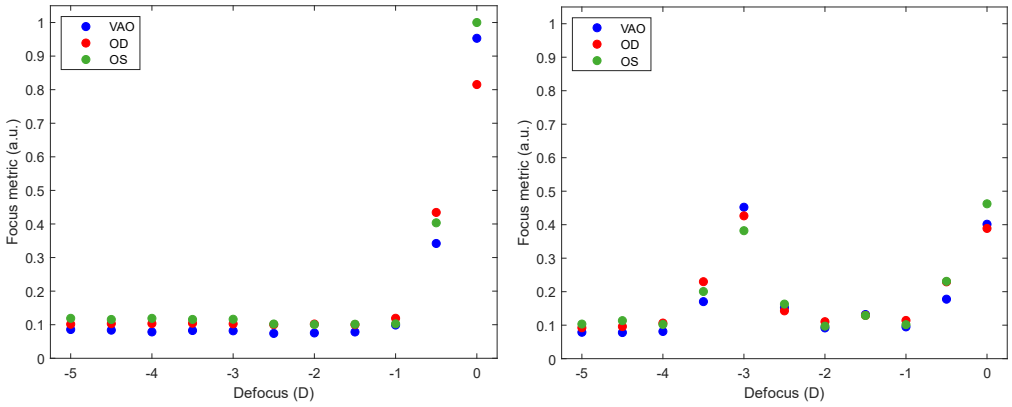


Figure 2.32. Focus quality measurements obtained from the screens of VAO, left and right eyes of the B-AOVS. X axis represents the induced defocus and Y axis represents the focus metric in arbitrary units. Left and right show the measurements without and with a bifocal diffractive profile respectively.

To quantitatively compare the image qualities, a focus metric was used to judge the sharpness of the images. The results of the focus metric parameter are shown in Figure 2.32. All screens exhibit similar trends, particularly noticeable for the bifocal profile which showcases the distribution of image quality across the two focus peaks for all displays, validating the correct behavior of the phase modulator for the new instrument.

Chapter 3: Applications

3.1. Through-focus curves with and without matching convergence

The main novelty of the B-AOVS (Sager, et al., 2025) is the incorporation of an automated vergence control system, enabling the study of binocular vision under more realistic viewing conditions. Previous B-AOVS devices have been used to assess visual quality under different phase profiles applied independently to each eye (Fernández, et al., 2013) (Lyu, et al., 2021), since asymmetric optical profiles are commonly employed in applications such as intraocular lens implantation to extend the depth of focus of binocular vision. These measurements were typically performed either in presbyopic subjects or under pharmacologically paralyzed accommodation, as this more accurately reproduces the visual experience following lens implantation. An advantage of these protocols was the assumption that the absence of accommodation effectively minimized the vergence-accommodation conflict. However, a realistic representation of natural binocular vision is not complete without appropriate control of the vergence angle. In fact, some studies have reported differences in through-focus measurements depending on whether distance changes were induced optically, using trial lenses, or physically, by moving the target, even in presbyopic subjects (Pieh, et al., 2002).

Complete testing requires independent control of convergence and accommodation, together with wavefront engineering capabilities, a combination previously unavailable. Using the new B-AOVS we measured binocular visual acuity defocus curves under different convergence conditions and with different phase profiles for subjects with absent accommodation. These measurements can provide insight into whether matching the vergence angle with the simulated accommodative distance results in a functional improvement for subjects without an accommodative response. This assessment is critical to either validate previous measurements obtained with other B-AOVS devices, or to limit their scope to simulating far distances and to perform relative comparisons between optical profiles.

3.1.1. Methods

Five subjects participated in this study that followed the tenets of the Helsinki Declaration and adhered to the ethical protocols approved by our institution. All subjects had refractive errors between 0D and -1.5D, astigmatism values below 0.5D, and high order RMS below 0.25µm for a 4.5mm pupil. Four of the subjects (**S1-S4**, ages 27 ± 2 years old) were measured after instilling one drop of tropicamide 1% to paralyze accommodation, while the last subject was

presbyopic (**S5**, age 54 years old). Without the influence of accommodation, the subjects were able to perform a visual acuity task under different distance and convergence combinations without noticeable discomfort. Their spherocylindrical refraction was calculated from Zernike coefficients measured and corrected with the phase modulator as a starting point for the measurements, while their high order aberrations remained uncorrected.

The defocus curves were obtained by measuring visual acuity in the range between +0.5D (virtual object 2m behind the subject) and -3.5D (object 28.6cm in front of the subject) in 0.5D steps. To ascertain whether convergence plays a role in the results when there is no accommodation present, the vergence angle was either fixed at 0D (far object) over the different distances or set to match each corresponding real distance (maintaining it at 0D for the virtual object). These measurements were repeated for three different amounts of spherical aberration symmetrically introduced in both eyes: 0, -0.09, and -0.19μm over a 4.5mm diameter pupil. These values were selected because there is evidence, in monocular conditions, that SA in this range can increase depth of focus without compromising visual acuity (Tabernero, et al., 2025).

Visual acuity measurements were performed using a black tumbling E over a white background with a 4-alternative forced-choice protocol (Bach, 1996). Five letter sizes were tested, changing in 0.1 LogMAR steps around a central value previously determined by adjustment for each condition. For each letter size there were eight repetitions, and the sequence of letter sizes and orientations was randomized for each trial.

The success rate was fitted to a psychometric logistic function (Wichmann & Hill, 2001) for each combination of defocus, spherical aberration, and convergence. The threshold of visual acuity was determined as the letter size that can be correctly identified half of the time, equivalent to a success rate in the middle point between clearly identifying the letter orientation (100% success rate) and randomly guessing (25% success rate in a 4-alternative method) which corresponds to a 62.5% success rate. The 95% confidence intervals were obtained using a bootstrapping method to randomly resample the data, as it has been shown to be less dependent on a large number of trials to provide accurate estimates (Wichmann & Hill, 2001).

Pupil size of both eyes was measured using the pupil tracking functionality of the B-AOVS for the presbyopic subject **S5** during all visual acuity tests. To obtain a pupil size value for each condition, the median was taken across all frames obtained during the duration of the test to minimize the impact of subject blinking. Subjects **S1-S4** were excluded from these measurements as the tropicamide drops used to paralyze accommodation also dilate the pupil.

These measurements could provide additional insight into whether pupil size plays a role in any potential differences in visual acuity for multiple convergence scenarios with absent accommodation.

3.1.2. Results

An example of the results obtained from an individual visual acuity test is shown in Figure 3.1. The visual acuity threshold obtained for this condition was 0.039 with 95% confidence interval [0.012,0.065] logMAR. The average confidence interval for all subjects was ±0.07 logMAR.

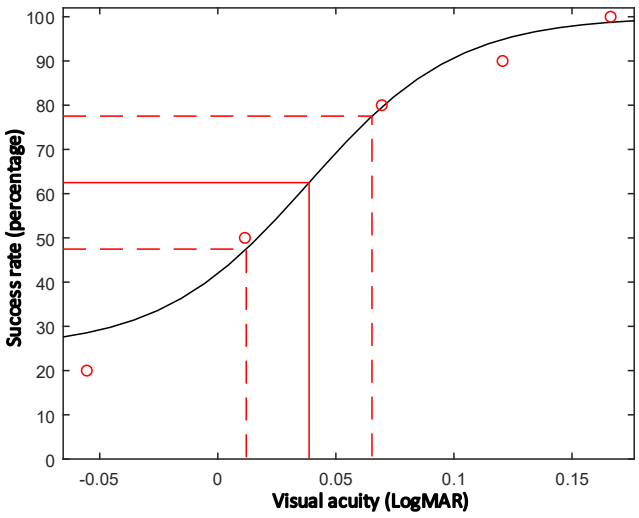


Figure 3.1. Psychometric fit of a visual acuity test. Red circles show the measurement results, solid black line shows the fit to a logistic function. Solid red line represents the visual acuity threshold and dashed red lines the 95% confidence intervals.

Individual defocus curves for all subjects are shown in Figure 3.2, showing that an increasing amount of negative spherical aberration creates flatter curves with lower peaks of visual acuity at closer distances, as would be expected from increasing the depth of focus. This is particularly noticeable for the presbyopic subject **S5**, for whom the accommodative response is completely absent and there is no risk of residual accommodation.

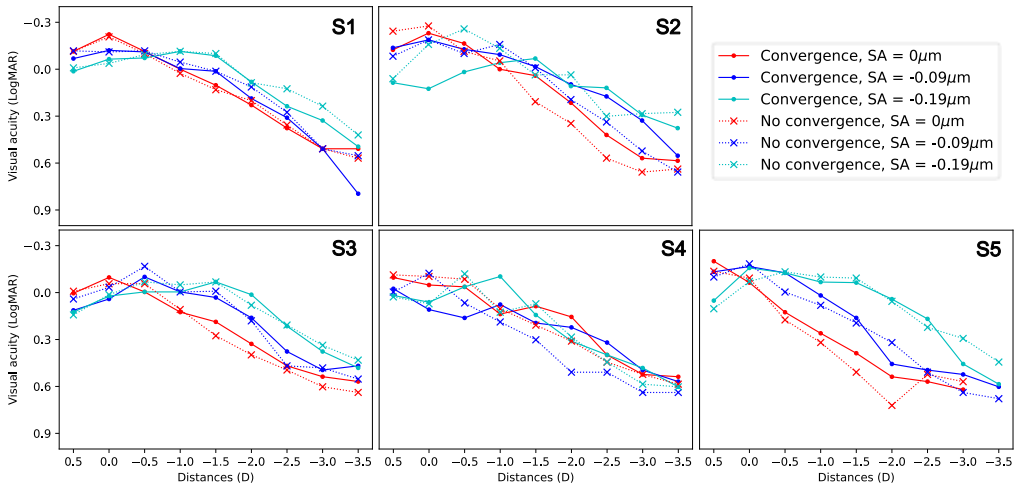


Figure 3.2. Individual defocus curves. Solid lines represent induced convergence matching accommodative distance, while dashed lines represent fixed convergence at 0D. Red, blue, and cyan represent induced spherical aberration values of 0, -0.09, and -0.19μm, respectively. Subjects S1-S4 were young people with paralyzed accommodation while subject S5 was a presbyope.

The average defocus curves across subjects for each spherical aberration case are shown in Figure 3.3. Curves with and without convergence induction remain in general close to each other. In terms of the average difference between the fixed and matching vergence conditions, no point presented differences larger than 0.1 logMAR while the overall average difference across all distances and SA values was 0.04 logMAR.

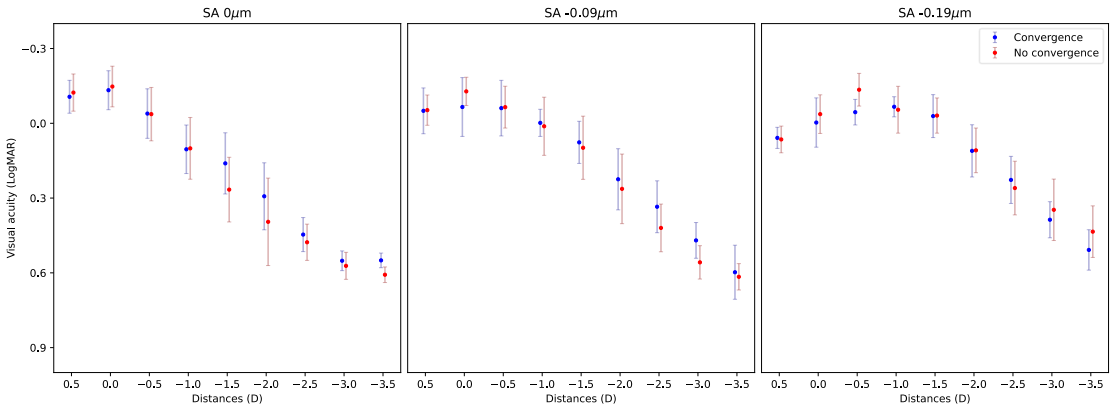


Figure 3.3. Mean defocus curves. Blue and red represent the presence or absence of convergence matching accommodation. Left, center and right represent induced spherical aberration values of 0, -0.09 and -0.19μm, respectively.

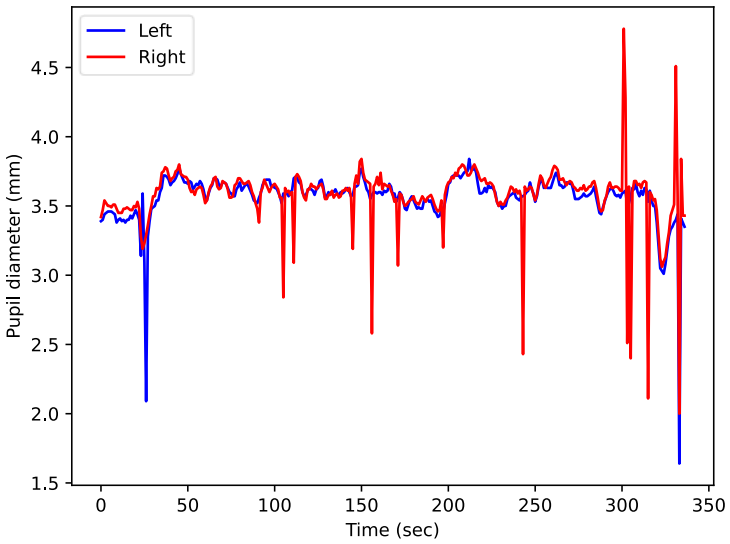


Figure 3.4. Pupil diameter measurements over one visual acuity measurement. Blue and red represent left and right eye, respectively.

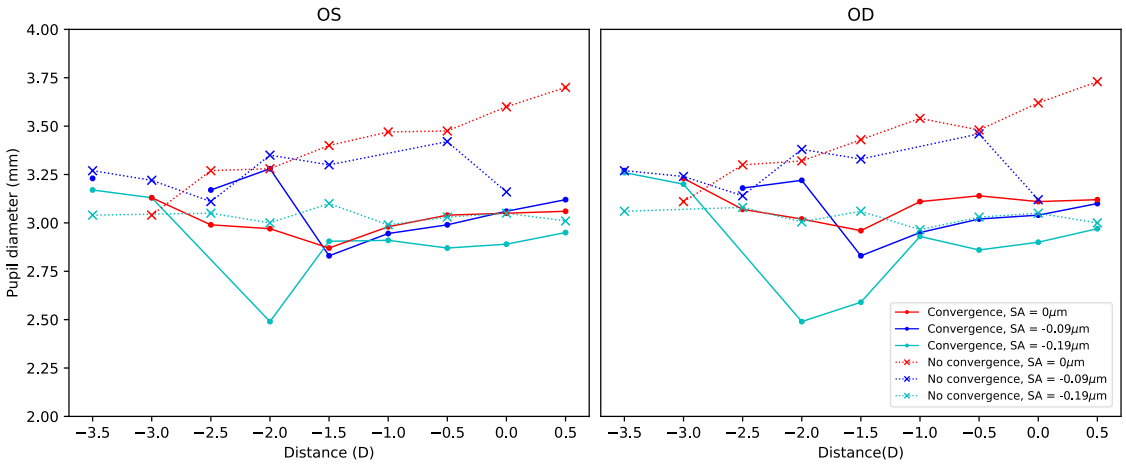


Figure 3.5. Pupil diameter measurements for subject S5 in every condition. Left and right represent the left and right eye, respectively, and the color scheme is the same as Figure 3.2.

An example of the pupil size measurement over the time of one visual acuity measurement is shown in Figure 3.4. The median of these measurements was taken for each distance and spherical aberration values, with the results shown in Figure 3.5. Pupil sizes for both eyes are very similar, as expected, with most points differing by less than 0.1mm. Regarding vergence conditions, pupil sizes seem to be more similar as the difference in vergence increases suggesting that vergence angle is not a dominant cause of pupil size, at least for this subject.

3.1.3. Discussion

Although some inter-subject variability was observed, the visual acuity values obtained with and without convergence induction were in general very similar, particularly in the averaged curves shown in Figure 3.3. In other words, the inclusion of convergence had little to no effect across any viewing distance or spherical aberration condition, suggesting that introducing the appropriate vergence angle in the absence of accommodation does not significantly affect visual acuity. Furthermore, when asked about their experience, subjects did not report any perceptible differences between the conditions with and without convergence in terms of image quality, fusion loss, discomfort, or visual fatigue.

The results previously obtained using earlier B-AOVS systems with presbyopic or cycloplegic subjects are therefore not challenged by these findings. While this outcome could be expected due to the absence of a vergence-accommodation conflict, it has previously been suggested that convergence might still influence visual acuity in presbyopic subjects through convergence-induced myosis (Pieh, et al., 2002). However, in our study no such effect was observed in the presbyopic subject (S5), who was tested under natural pupil conditions. On the contrary, the defocus curves appeared to converge across vergence conditions as the simulated viewing distance increased. The condition without spherical aberration is particularly interesting, since the largest pupil size differences occurred at 0D and +0.5D, where all vergence settings remained identical, suggesting that natural pupil fluctuations associated with fatigue may dominate over any effect produced by convergence matching.

Subjects also reported no preference for either the fixed-vergence or matched-vergence conditions, indicating a very similar subjective visual experience. Although subjective responses were not evaluated systematically in this experiment, preliminary measurements performed in subjects with normal accommodative responses resulted in clear reports of discomfort and fusion instability. This further supports the conclusion that the influence of vergence is minimal or nonexistent in the absence of accommodation.

To summarize, we measured defocus curves for increasing amounts of spherical aberration in subjects without active accommodation (four young cyclopleged individuals and one presbyopic subject), both with and without convergence matched to the accommodative stimulus. As expected, depth of focus increased with additional spherical aberration, but the inclusion of convergence control had no significant effect under these non-accommodating

conditions, thereby supporting the validity of results previously obtained with earlier generations of B-AOVS systems.

Beyond validating previous research, the new prototype provides the means to investigate the vergence-accommodation conflict under different vergence demands and optical phase profiles. This capability is particularly relevant in the field of extended reality, where the vergence-accommodation conflict is considered one of the main causes of visual discomfort, while the potential benefits of complex phase profiles remain largely unexplored due to the lack of instrumentation capable of simultaneously controlling vergence. The automated vergence control system allows specific vergence angles to be set within seconds, making it highly suitable for psychophysical experiments involving multiple vergence-accommodation combinations. This novel functionality of the B-AOVS was used to perform a series of objective and subjective measurements investigating the vergence-accommodation conflict under different spherical aberration conditions, as described in the following section.

3.2. Effect of spherical aberration on the vergence-accommodation conflict

Extended reality (ER) devices are increasingly used in fields such as entertainment, education, research, and professional practice. Despite their unique advantages as three-dimensional (3D) display systems, a substantial proportion of users report visual discomfort, particularly after prolonged use (Sharples, et al., 2008). This is mainly attributed to the vergence-accommodation conflict (VAC) introduced by such displays (Hoffman, et al., 2008).

The human visual system naturally couples vergence and accommodation, with changes in one typically eliciting a corresponding response in the other. When binocular stimuli are decoupled, such as when each eye receives an independent image, these responses can become incongruent, leading to visual discomfort or, for sufficiently large disparities, even fusion loss (Ogle, 1932). ER devices inherently induce some degree of VAC, since they allow flexible vergence control via independent displays while typically maintaining a fixed accommodative distance. Various strategies have been proposed to mitigate this problem (Kramida, 2016) (Zhan, et al., 2020) (Yin, et al., 2022), including multifocal displays with several focal planes or tunable lenses (Akeley, et al., 2004) (Hu & Hua, 2014) (Suyama, et al., 2000), ray-based devices such as Maxwellian or pinhole displays (Waldkirch, et al., 2004) (Maimone, et al., 2014), and systems employing gaze-contingent accommodation or vergence control (Hillaire, et al., 2008) (State, et al., 2001). However, none of these approaches has provided a definitive solution so far, either being unable to fully eliminate discomfort or being too complex and costly for widespread implementation.

Wavefront manipulation to achieve extended depth of focus (EDoF) may offer an alternative, relatively unexplored strategy to alleviate VAC as accommodation could change to match vergence without a significant visual quality loss. If suitable aberration-based EDoF profiles could reduce visual fatigue and discomfort, they might represent a simple and cost-effective solution applicable to existing ER systems. Such optical designs could be integrated as baseline components, added as interchangeable lenses (similar to the refraction correction already incorporated in some headsets), or implemented externally through customized spectacles or contact lenses.

To our knowledge, only one prior study by Lyu et al. (Lyu, et al., 2021) directly addressed this possibility. Using a binocular adaptive optics visual simulator, they evaluated EDoF profiles

based on spherical aberration (SA) of opposite signs and suggested that these profiles might slightly improve stereoacuity under certain VAC conditions. However, accommodative measurements were done with four vergence conditions and visual performance was assessed with a single vergence change, as each adjustment required manual reconfiguration of the optics, limiting the scope of their investigation.

We measured the impact of SA-based EDoF profiles alternating between multiple VAC conditions using the developed binocular visual simulator with motorized vergence control. The device allows rapid and precise adjustments of angular disparity, enabling a more systematic study of the effects of vergence variation. The selected EDoF profiles were based on negative SA values applied simultaneously to both eyes, avoiding potential discomfort that asymmetric profiles can introduce during short-term viewing (Collins, et al., 1994).

An initial pilot study was conducted to measure the time required for a subject to focus an image after an accommodative change under different conflict scenarios, as this has been used in recent studies to assess the effect of VAC (Spiegel & Erkelens, 2024). However, due to the unreliability of the data obtained in said pilot study a larger measurement protocol was developed focusing on two key outcomes: stereoacuity, as a quantitative measure of visual performance used more commonly in previous VAC studies (Hoffman, et al., 2008) (Duchowski, et al., 2014), and subjective discomfort assessed through standardized questionnaires, which remain the most common method for evaluating visual fatigue and perceived strain under such conditions (Chang, et al., 2020). Measurement methods and results of the larger study described in the following sections can also be found elsewhere (Sager, et al., 2026).

3.2.1. Methods

Both studies followed the tenets of the Helsinki Declaration and adhered to the ethical protocols approved by the institution pertaining to this project (University of Murcia, Spain).

Pilot study: Time to Focus

Three subjects under 35 years old with at least 4D of accommodative response were recruited. Subjects were measured with the Hartmann-Shack sensor of the novel B-AOVS (Sager, et al., 2025) to obtain an objective starting point for refraction correction, which was then refined with a standard subjective refraction protocol performed with the visual simulator. A value of -1D was added to refraction to simulate a stimulus at 1m distance, and vergence angle was set to match the accommodative distance of one meter as the baseline condition.

A 4-alternative forced-choice measurement with a tumbling E was performed, where the size of the letter was fixed at 0 logMAR for a variable presentation time of the stimulus. After a correct response from the letter orientation in the baseline condition, vergence and simulated distance changed to the considered conflict scenario and the user response was recorded Each test involved eight repetitions of five different presentations times chosen after an initial adjustment test, and a logistic psychometric curve was fit to the results to obtain the time required to focus. Tests were repeated for accommodative distances raging from -2D to 0D (distances from 0.5 m to infinity) in 0.5D steps, which induced VAC conditions from -1D to +1D.

Finally, the protocol was performed for spherical aberration values of 0, -0.09, and -0.19μm over a 4.5mm diameter pupil as they have been shown to increase depth of focus without a significant decrease in visual acuity (Tabernero, et al., 2025). All VAC and SA conditions were randomly presented during the measurement session to randomize the effects of training and fatigue, and to avoid anticipatory accommodative changes before stimulus presentation.

Main study: Stereoacuity

The larger experiment was performed with 10 subjects under 35 years old with at least 4D of accommodative response. Similarly to the previous study, subjective refraction was measured with the B-AOVS. Baseline defocus was changed by -1.5D to position the stimuli at a distance of 0.67cm in front of the subject. This distance was chosen to resemble some extended reality devices (Aizenman, et al., 2023) and provided a starting point to study both directions of the vergence-accommodation conflict, as it was kept constant while the vergence settings were cycled between 0 (i.e., parallel lines of sight), 1.5 and, 3 diopters (i.e., lines of sight converging on a point 33.3 cm in front of the subject), corresponding to conflicts of -1.5, 0 and 1.5 diopters, respectively.

The addition of SA should be theoretically sign symmetric, but its interaction with the eye's aberrations causes a myopic/hyperopic shift for negative/positive SA values (Rocha, et al., 2009). A negative sign for SA was selected to minimize the negative VAC, as this direction of the conflict has been shown to have a stronger effect on stereoacuity (Banks, et al., 2008), while the extended depth of focus provided by the profile could be expected to alleviate the other direction of the conflict.

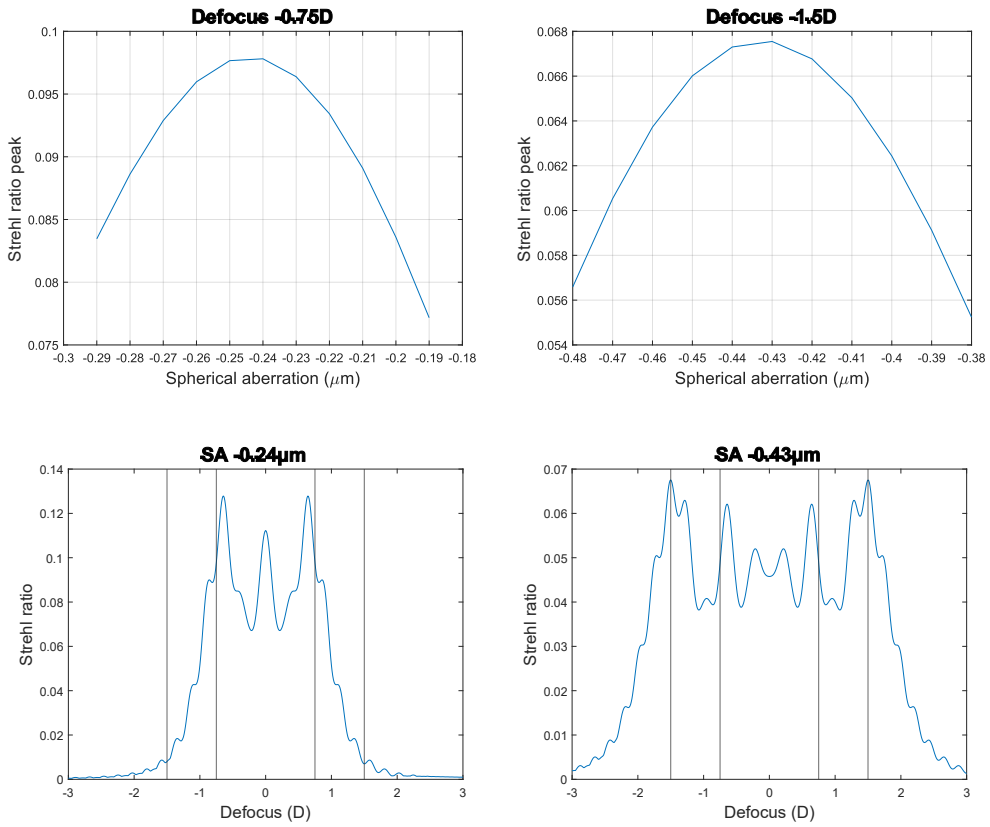


Figure 3.6. Top row, Strehl ratio peak as a function of spherical aberration for a defocus of -0.75 (left panel) and -1.5D (right panel). Bottom row, Strehl ratio as a function of defocus for SA values of -0.24 μm (left panel) and -0.43μm (right panel).

To select the specific values of SA, computer simulations were performed to obtain the Zernike coefficients for a 4.5mm diameter pupil that provide the first local maximum of Strehl ratio at -0.75D and -1.5D of defocus, as shown in Figure 3.6, top row. The optimal values found were -0.24 and -0.43μm, respectively, and their through focus values for the Strehl ratio are shown in Figure 3.6, bottom row. The largest SA value therefore should create a defocus shift of -1.5D, minimizing the negative condition of the conflict with the same value, while the smaller value results in an intermediate condition with a halfway shift of -0.75D.

Stereoscopic performance was evaluated using a three-needle protocol, adapted from Fernández et al. (Fernández, et al., 2010). Participants viewed three black lines on a white background: the two outer lines remained fixed while the central “needle” was laterally displaced in opposite directions for each eye, creating a binocular disparity that generated a perception of depth. The sign of the disparity determined whether the central needle appeared in front or behind the outer pair. Additionally, the baseline position of the central needle changed every trial, to avoid potential monocular cues. All needles had a width of 4.4 arcmin and height of 22 arcmin, and the fixed outer needles were separated 22 arcmin. Given the instrument’s

resolution, the smallest disparity step (one pixel between eyes) corresponded to 8.8 arcsec. Although this value remains sub-threshold for most observers, finer stereoacuity values have been reported (Fernández, et al., 2013) (Hess, et al., 2016). To avoid reaching the system's limit, presentation time was restricted to 0.5 s, which is known to raise stereoacuity thresholds (Harwerth, et al., 2003). A fixation cross was displayed between trials to maintain vergence and fusion throughout the test.

Nine experimental conditions combining three SA levels (0, -0.24, -0.43 μm) and three vergence disparities (-1.5, 0, +1.5 D) were tested. Each condition was subdivided into six sessions to minimize both training and/or fatigue effects. A session comprised six angular disparities with four repetitions (two forward and two backward displacements), resulting in 24 repetitions per data point. Sessions were grouped by vergence distance. A measurement block included all three vergence settings, each of them cycling through the three SA profiles. All possible permutations of SA–VAC combinations were evaluated, each block representing one permutation. Block order was randomized, with two blocks per day and a total of three measurement days per subject over one week. This protocol required 18 vergence changes per subject, which was facilitated by the automatic vergence control incorporated in the device.

Before the first block, each participant completed a training session consisting of stereoacuity measurements with 12 repetitions per data point under far-viewing conditions (0 D vergence and accommodation). Training continued until participants consistently perceived depth direction for large disparities and obtained stereoacuity values differing by <10% across consecutive runs. At the start of each day, an additional baseline session (no VAC, no SA) was recorded. If any participant reported excessive difficulty, discomfort, or fatigue, measurements were rescheduled. For each condition, the success rate versus disparity, combining forward and backward displacements into a single psychometric function, was fitted to a logistic function using maximum-likelihood estimation, and the stereoacuity threshold was extracted from the fitted curve.

To complement the objective measurements, a four-item subjective questionnaire, adapted from Hoffman et al (Hoffman, et al., 2008), was administered to assess visual blur, adverse effects, comparative discomfort, and session preference for each SA–VAC combination.

The first two questions evaluated each condition independently:

1. “How clear was your vision?”
2. “Did you experience nausea, headache, or visual fatigue?”

Responses were given on a five-point scale ranging from no impact to severe symptoms. The quantitative variables associated with these two questions will be dubbed “visual blur” and “side effects” respectively.

The remaining two questions compared each session with the previous one:

3. “Which session produced more discomfort?”
4. “Which session did you prefer?”

These were rated on a five-point comparative scale, where the central value indicated no preference and the lowest level a strong preference for the current session. Consequently, the associated quantities will have names with negative connotations: “comparative discomfort” and “comparative dislike”, respectively. The questionnaire is shown in Figure 3.7.

Because of the limited sample size, mean values were compared using the Wilcoxon signed-rank test instead of the parametric Student’s t-test. The obtained p-values are reported with subscript notation to specify the comparison:

- S0, S1, and S2 stand for SA cases: No SA, -0.24µm, and -0.43µm, respectively.

- C0, C+, and C- denote VAC cases: No conflict, positive VAC, and negative VAC, respectively.

For example, $P_{(S0,S1);C0}$ compares 0µm and -0.24µm SA in the no-conflict condition, whereas $P_{S0;(C0,C+)}$ compares no conflict vs positive conflict for the baseline SA.

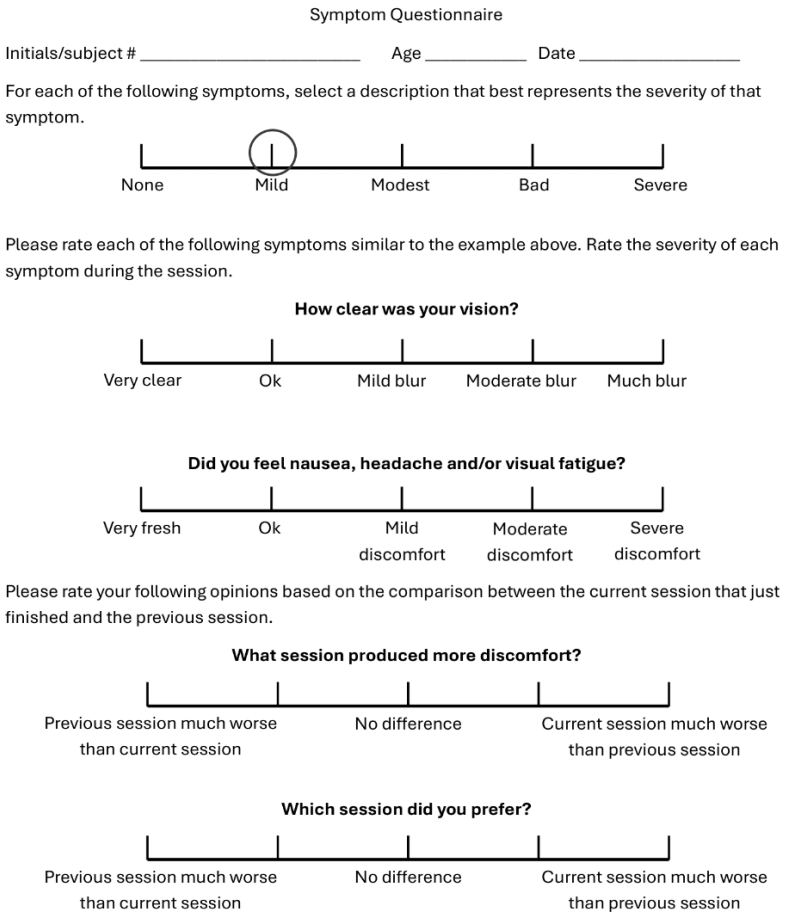


Figure 3.7. Subjective questionnaire presented to the subjects to answer after each session

As a final comment, when reporting the results and discussing the outcomes of this study, we decided to follow the recommendation of McShane et al (McShane, et al., 2019) and "abandon statistical significance". This means that instead of setting an arbitrary threshold (typically $p<0.05$) to binarize our analysis (happens/not happens), we will speak in terms of plausible possibilities suggested by the results and provide the p-values for the reader to consider.

3.2.2. Results

The results for the time to focus obtained in the pilot study for the three subjects across VAC and SA conditions are shown in Figure 3.8. Changes in spherical aberration do not show clear discernible trends and seem to have a small effect on the time to focus. More importantly, subjects S2 and S3 could not focus over any amount of time without prior rest for certain spherical aberration conditions at the largest VAC values. These conditions presented measurable values when measured independently. The unreliability of data acquisition using this

protocol led to the adoption of a different measurement procedure for the study on a larger sample.

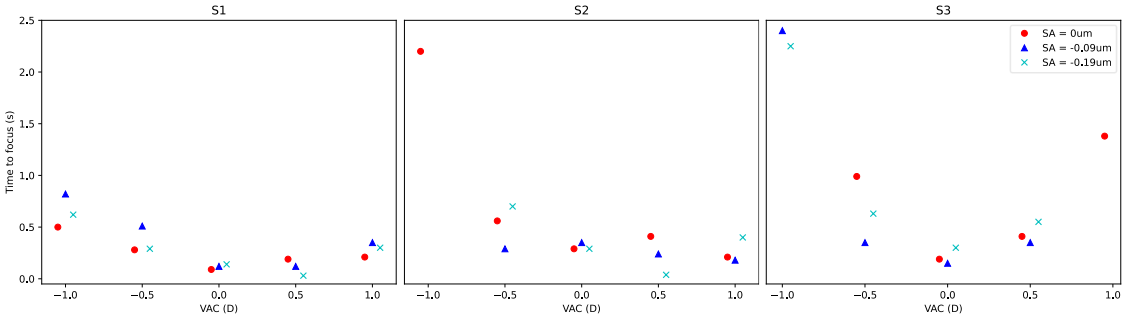


Figure 3.8. Time to focus measurements for three subjects. Red, blue and cyan represent spherical aberration values of 0, -0.09 and -0.19μm respectively. Left, center and right represent the results of subjects S1, S2 and S3 respectively.

The results of the main study for the ten individual subjects are shown in Figure 3.9 (left), where stereoacuity measurements are represented as a function of spherical aberration (SA). Each color represents a vergence condition, introducing different levels of conflict relative to the fixed accommodative distance. Subjects are ordered left to right by increasing mean stereoacuity threshold (averaged across all SA and VAC cases). The right panel of Figure 3.9 shows the mean normalized stereoacuity against SA using the same color scheme. Normalization was performed by dividing each individual threshold by each subject's mean stereoacuity across SA conditions in the no-conflict case. Normalized stereoacuity was compared between conflict cases for each spherical aberration value and between SA levels for each VAC condition. All p-values can be found in Table 3.1.

Substantial inter-subject variability was observed, both in absolute values and in trends, with no consistent pattern across participants. Baseline stereoacuity (no VAC, no SA) was generally poorer than standard literature values (Blakemore, 1970), which can be attributed to the shortened 0.5 s presentation time used in this experiment.

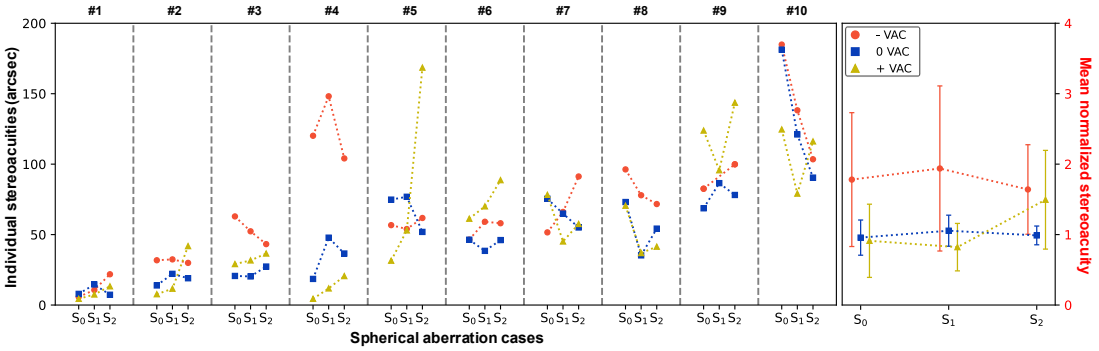


Figure 3.9. Left panel: Individual stereoacuity thresholds in arcsec (left vertical axis) for subjects #1 to #10, ordered by increasing mean stereoacuity across all cases, as a function of SA added (horizontal axis: S0=0, S1=-0.24µm, and S2= -0.43µm) for positive (yellow), negative (red) and no VAC (blue). Right panel: mean normalized stereoacuity (right vertical axis) versus SA. Before averaging, each individual value was divided by the subject's mean stereoacuity across SA cases in the absence of VAC. Error bars represent standard deviation.

Negative VAC in the absence of added SA tended to degrade stereoacuity for most subjects, particularly for those with the best baseline performance, supporting previous reports that more stereosensitive observers are also more susceptible to VAC effects (Duchowski, et al., 2014). Conversely, the influence of positive VAC was inconsistent among participants.

Spherical aberration had a modest overall effect on stereoacuity, but its impact depended on the conflict condition. In the no-conflict scenario, SA produced minimal and inconsistent changes, yielding a nearly flat trend on average (Figure 3.9, right). Under positive VAC, however, the addition of -0.43µm of SA appeared detrimental ($P_{(S0,S2);C+} = 0.084$; $P_{(S1,S2);C+} = 0.002$), whereas for negative VAC the same amount of SA may have improved performance slightly, although the behavior was very erratic among subjects. These effects were not evident for the smaller -0.24µm SA condition.

Figure 3.10 summarizes the results of the subjective questionnaire, including visual blur, side effects, comparative discomfort, and comparative dislike. All p-values for the corresponding Wilcoxon tests between conditions are provided in Table 3.1.

Visual blur (Figure 3.10, top row) increased consistently with SA in the no-conflict case (blue line; $P_{(S0,S1);C0} = 0.004$, $P_{(S0,S2);C0} = 0.002$, $P_{(S1,S2);C0} = 0.004$). For positive VAC (yellow line), blur started at a similar level to the baseline and also increased with SA ($P_{(S0,S2);C+} = 0.002$). This behavior aligns with the expected direction of focus shift. In contrast, for negative VAC (red line), blur was initially

higher than baseline ($P_{S0;(C0,C-)}$ = 0.008), did not ostensibly change with the addition of -0.24µm SA, and apparently rose slightly for -0.43µm ($P_{(S0,S2);C-}$ = 0.097).

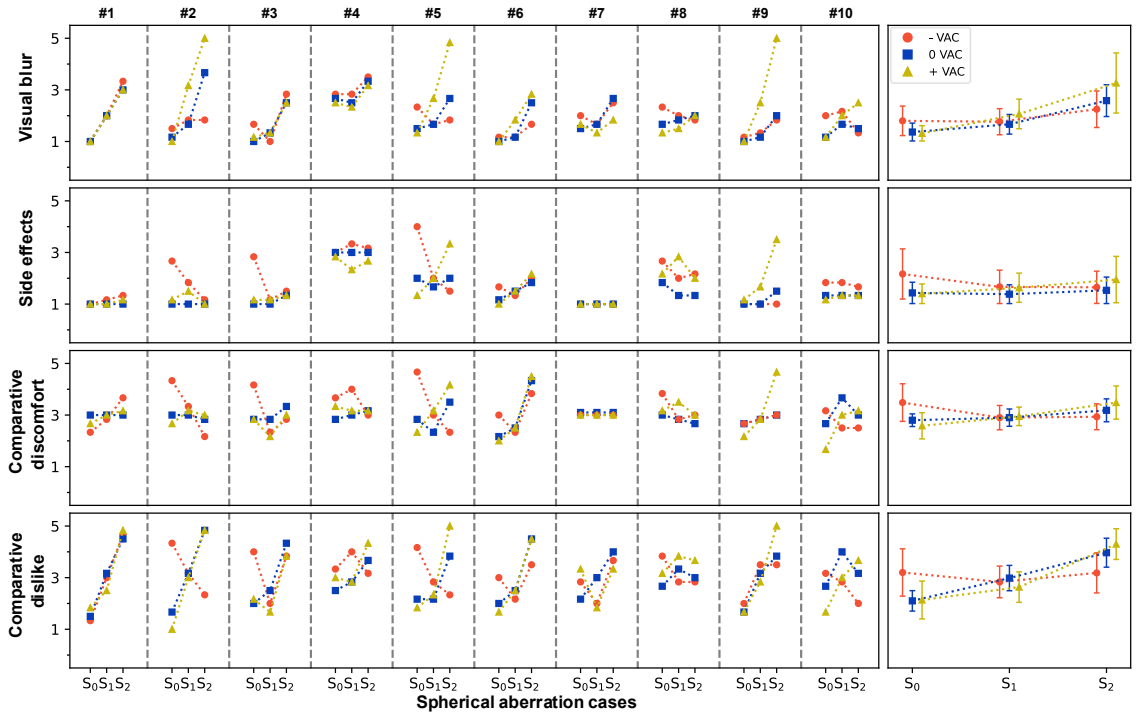


Figure 3.10. Individual (left panel) and mean (right panel) subjective scores for each conflict case as a function of SA added (S0=0, S1=-0.24µm, and S2= -0.43µm). Color scheme is the same as Fig. 1. Y-axes for visual blur (top row) and side effects (upper middle row) range from no symptoms (1) to severe symptoms (5). Y-axes for comparative discomfort (lower middle row) and general preference (bottom row) range from strong preference of present session (1) to strong preference for previous session (5). Error bars represent standard deviation across subjects.

Side effects (upper middle panel) showed no clear changes with SA under no conflict. For positive VAC, they were similar to baseline but tended to worsen slightly as SA increased, especially for some individuals (e.g., #5 and #9). As expected from previous reports (Shibata, et al., 2011), negative VAC without added SA produced higher levels of side effects ($P_{S0;(C0,C-)}$ = 0.027, $P_{S0;(C+,C-)}$ = 0.025). Importantly, they appeared to diminish with added SA ($P_{(S0,S1);C-}$ = 0.075) and remained at similar levels when increasing SA to -0.43µm.

Comparative discomfort (middle-lower row) confirmed these tendencies, revealing a clearer improvement with increasing SA under negative VAC: discomfort was greatest with no SA ($P_{S0;(C0,C-)}$ = 0.025, $P_{S0;(C+,C-)}$ = 0.013), and decreased for -0.24µm ($P_{(S0,S1);C-}$ = 0.050) and possibly for -0.43µm ($P_{(S0,S2);C-}$ = 0.192) of SA.

Comparative dislike (bottom row) apparently reflected the balance between perceived sharpness and side effects. Dislike increased with SA for no conflict ($P_{(S0,S1);C0}$ = 0.008, $P_{(S0,S2);C0}$ = 0.002) and positive conflict ($P_{(S0,S2);C+}$ = 0.004, $P_{(S1,S2);C+}$ = 0.008), consistent with greater perceived blur. In contrast, for negative VAC dislike was kept at similar or slightly lower levels with increasing SA, suggesting that comfort outweighed the loss of sharpness. Consequently, subjective preference switched direction: while negative VAC was least favored with no SA ($P_{S0;(C0,C-)}$ = 0.004), it became the preferred condition with -0.43µm SA ($P_{S2;(C0,C-)}$ = 0.006). Interestingly, the intermediate SA value tended to equalize side effects and discomfort among conditions, reducing preference differences.

		Normalized stereoacuity	*Visual blur*	*Side effects*	*Comparative discomfort*	*Comparative dislike*
C-	*(S0, S1)*	0.820	0.623	0.075	0.050	0.432
	(S0, S2)	0.846	0.322	0.182	0.192	0.770
	(S1, S2)	0.570	0.097	0.888	0.889	0.262
C0	*(S0, S1)*	0.770	0.004	0.414	0.400	0.008
	(S0, S2)	0.557	0.002	0.357	0.067	0.002
	(S1, S2)	0.375	0.004	0.059	0.398	0.020
C+	*(S0, S1)*	0.557	0.020	0.089	0.075	0.131
	(S0, S2)	0.084	0.002	0.234	0.033	0.008
	(S1, S2)	0.002	0.002	0.263	0.091	0.004
S0	(C0, C+)	0.557	0.450	0.723	0.139	0.858
	(C0, C-)	0.232	0.008	0.027	0.025	0.004
	(C+, C-)	0.160	0.008	0.025	0.013	0.037
S1	(C0, C+)	0.375	0.260	0.173	0.673	0.093
	(C0, C-)	0.074	0.172	0.024	1.000	0.514
	(C+, C-)	0.012	0.141	0.799	0.888	0.275
S2	(C0, C+)	0.049	0.193	0.116	0.078	0.121
	(C0, C-)	0.002	0.193	0.372	0.161	0.006
	(C+, C-)	1.000	0.091	0.677	0.035	0.015

Table 3.1. P-values for the Wilcoxon signed-ranked tests for stereoacuity and subjective questionnaire answers. Upper section: comparison between SA values for each conflict case; lower section: comparison between VAC conditions for each SA value.

To better illustrate this perceived trend of discomfort homogenization across VAC conditions, we performed a post hoc analysis on the differences between the subjective scores across conflict scenarios. Figure 3.11 shows (in purple) the range in subjective scores, defined as the difference between best and worst scores among conflict situations, as a function of added SA. Individual scores and mean values across subjects are shown in left and right panels, respectively. Additionally, we include (in blue) the average score across VAC conditions for each SA value. Table 3.2 shows the p-values of the Wilcoxon signed-rank tests between conditions for both score range and average.

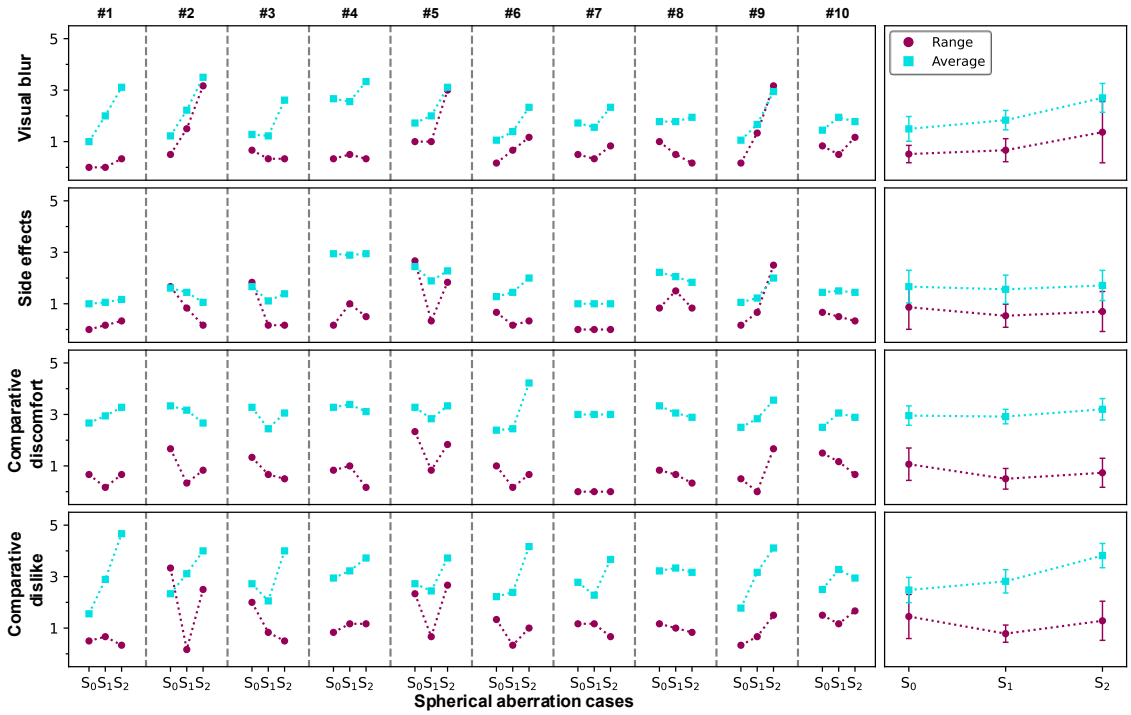


Figure 3.11. Average (cyan) and range (difference between highest and lowest scores; magenta) of subjective scores across VAC cases for each SA value (S0=0, S1=-0.24μm, and S2= -0.43μm). Left, individual results for each subject. Right, mean values across subjects.

Adding -0.24μm of SA may increase mean visual blur (and its range) and does not apparently improve on average any of the other three subjective scores, but it seems to reduce the changes in the level of bother caused by the different conflict cases, as the range goes down for comparative discomfort ($P_{(S0,S1);Range}$ = 0.013) and, possibly, for comparative dislike ($P_{(S0,S1);Range}$ = 0.131).

	Visual blur		*Side effects*		*Comparative discomfort*		*Comparative dislike*	
	Range	*Average*	*Range*	*Average*	*Range*	*Average*	*Range*	*Average*
(S0, S1)	0.722	0.051	0.553	0.513	0.013	0.953	0.131	0.193
(S0, S2)	0.058	0.002	0.528	1.000	0.161	0.515	0.322	0.004
(S1, S2)	0.020	0.004	0.888	0.214	0.339	0.192	0.173	0.010

Table 3.2. P-values for the comparison between data points for the range and average values across conflict conditions of the subjective questionnaire. Left column shows the SA values (S0=0, S1= -0.24μm, and S2= -0.43μm) being compared.

On the other hand, range values averaged across subjects (Figure 3.11, right panel) seem to bounce back for -0.43μm for discomfort and dislike, conceivably as a consequence of the previously mentioned opposing trends for negative and positive VAC. However, there is variability among subjects, with some of them giving better scores for the largest SA case, suggesting that there could be an optimal value of SA which could depend on the subject.

3.2.3. Discussion

The main goal of this work was to explore the potential of aberration based EDoF profiles, in this case based on spherical aberration, to mitigate the vergence-accommodation conflict. The first measurement metric was the time to focus, which showed no discernible correlation between spherical aberration and VAC conditions. Furthermore, some measurements were too difficult for the subjects in the full randomized protocol while a task focused on those specific scenarios yielded results in line with the other values. This could be explained by the higher demand of the complete task requiring accommodative changes in unknown directions (either relaxing or increasing accommodation), causing a level of fatigue that impedes proper focus on the stimulus in a reasonable amount of time. The independent measurements were always performed in a predictable manner, as the accommodative changes were always the same which considerably simplified the task. The unreliability of data collection for this method and the lackluster initial results was reason enough to switch measurement metric for a larger, more comprehensive second study with larger values of spherical aberration and vergence-accommodation conflict.

The task chosen to quantify visual performance in the final experiment was stereoacuity, and our results can be considered consistent with preceding studies: A strong variability was observed between subjects (Ukwade, et al., 2003), with a larger drop in stereoacuity for negative VAC (Hoffman, et al., 2008). However, we expected the addition of -0.43µm of spherical aberration to improve stereoacuity, at least for the -1.5D vergence-accommodation conflict, given that both the depth-of-focus extension and the focus shift caused by negative SA should be advantageous for that particular condition. Therefore, we find it somewhat surprising that the effect was not very pronounced or even consistent.

Consequently, there is little in the stereoacuity results to recommend the addition of spherical aberration in variable VAC situations. The mild effects observed when adding SA could be simply due to the ensuing best-focus shift. These effects could also be more pronounced for certain subjects, as it has been suggested that subjects with better baseline stereoacuity could experience a stronger relative effect when a conflict condition is introduced (Duchowski, et al., 2014). Our small sample size coupled with the lack of exclusion criteria based on baseline stereoacuity could be homogenizing the results and therefore hiding some tendencies pertaining specific groups of subjects. Additionally, some subjects may be experiencing a smaller range of depth of focus due to their own natural aberrations, limiting the effect of SA in some conflict

scenarios that could be improved with further customization. It is possible that EDoF optics provide an advantage for some subjects in some VAC situations but, from the point of view of visual performance, it seems an unlikely cure-all solution.

The results of the subjective questionnaire show improvements for certain conditions with the addition of SA, but there is no profile that results in an overall best experience under all conflict scenarios. In the baseline (no added SA) situation, the worst condition for both side effects and discomfort was negative VAC, which was also the least liked. In an extended reality setting with changing VAC situations, negative conflict may therefore have a stronger contribution to dizziness, headache, and other symptoms of tiredness experienced by some users after prolonged exposure. Adding spherical aberration to increase depth-of-focus clearly improves the situation for negative conflict, at least comparatively, changing to be the best liked option for the largest SA tested. The positive direction of the conflict shows the opposite trend, becoming less preferred with the addition of SA.

Consequently, the original hypothesis of this work, that the addition of SA profiles would reduce the effects of the vergence-accommodation conflict, is not supported by the results obtained. Neither stereoacuity measurements nor the subjective questionnaire suggest that a single SA profile could improve the overall experience for all subjects under a variety of VAC conditions. Whether the addition of such profiles provides an advantage for specific subjects after individual customization remains to be seen.

However, an interesting outcome may be happening for an intermediate amount of SA, where all three conflict cases seem to be more similar in side effects and comparative discomfort, as well as in terms of comparative dislike. We performed an exploratory analysis of this finding, yielding results that suggest that the addition of an intermediate amount of SA could homogenize the subjective experience across conflict scenarios.

Increasing the similarity between different conflict scenarios could be relevant when working with extended reality for lengthy periods of time, as studies have suggested that dynamic changes in VAC can generate more discomfort than having a constant conflict condition (Banks, et al., 2013) (Kim, et al., 2014). In that case, introducing a specific optical element to arrange an environment without significant differences between VAC conditions could be a welcomed option in applications with frequent changes in vergence, even if they prove to be slightly less comfortable or visually sharp than baseline on average.

The intermediate SA chosen for this study creates similar average levels of side effects and discomfort, only slightly worse levels of perceived visual blur, and improves homogenization of discomfort across conditions when compared to the baseline case with no SA added. Whether this kind of discomfort equalization results in a significant improvement in nausea or other fatigue symptoms for ER applications with dynamic vergence changes for all subjects without requiring optical customization remains to be seen, but it seems a topic worthy of investigation through specifically designed studies, as it could have implications in the usability of ER devices. If proven beneficial for the general public, the optics of such devices could be modified to add SA or other depth-of-focus-extending optical elements. On the other hand, if some degree of customization is required, the ER user may consider wearing multifocal contact lenses selected among the varieties already available in the market. Another option would be to modify the "lens inserts", already sold by VR companies to correct refraction, using wavefront-shaping lens designs that could be generic or specifically prescribed for each user.

Summarizing, the results of this study are less conclusive than we anticipated, even accounting for the small sample size. It was reasonable to expect the EDoF characteristics of SA to improve visual performance in vergence-accommodation conflict situations, but the stereoacuity results do not show that trend. This could be due to the small sample size as the effect of VAC on stereoacuity is notoriously subject-dependent (Ukwade, et al., 2003), and most studies in the field discard visual quality metrics in favor of purely subjective questionnaires. Regarding this matter, even if it is not advantageous from the point of view of visual performance, SA may be beneficial in terms of discomfort, not by reducing it globally but by mitigating its peaks for specific VAC cases. Although this is a very tentative hypothesis due, among other reasons, to the small sample size, the variability among subjects, and the fact that the task chosen does not resemble a typical use case of ER devices. However, the implications could be significant considering the increasing ubiquitousness of extended reality in science, industry, leisure, etc. This issue could be the subject of a future larger study analyzing the potential value of aberration based EDoF optics for extended reality users.

Chapter 4: Conclusions

The main objective of this thesis was the development and application of a novel binocular adaptive optics visual simulator with an automatic convergence control system, capable of simulating complex optical profiles and performing psychovisual tests under more realistic binocular conditions.

The conclusions of this work are as follows:

1. A new prototype of binocular adaptive optics visual simulator with an integrated automatic convergence control system was successfully developed. Its core functionalities also include independent eye control of pupil size, phase modulation, aberration measurement, and stimulus presentation. Its compact design minimizes cost and overall size of the device, making it suitable for clinical use.
2. A comprehensive calibration procedure was implemented to compensate for the ellipticity introduced by the intensity and phase modulator, to determine the effective focal length of the Hartmann-Shack wavefront sensor and the proportionality factor of the tunable lens, and to establish an accurate transformation between motor steps and both pupil displacement and angular change. Validation of the wavefront sensor was carried on an artificial eye while phase modulation performance was compared to the commercially available visual simulator, VAO.
3. Using the capabilities of the prototype developed in this thesis, through-focus visual acuity was measured in subjects without accommodative response yielding similar results with and without matching convergence, suggesting that secondary effects such as myosis do not significantly influence these tests. This study supports the validity of prior results obtained using simulators without vergence control.
4. A final experiment tested the impact of spherical aberration on the vergence-accommodation conflict, a line of research facilitated by the novel functionalities of the instrument. Results showed small differences in stereoacuity and overall subjective experience when depth of focus was increased through the addition of spherical aberration. However, evidence was found that one aberration profile resulted in a homogenization of discomfort across conflict scenarios, which could prove advantageous in extended reality applications involving dynamic vergence changes.
5. The instrument developed offers promising capabilities to study binocular vision under complex optical profiles and controlled vergence conditions, which is particularly relevant for augmented/virtual reality applications. Future studies will continue using the novel prototype to explore the effect of complex optical profiles in the vergence-accommodation conflict, an area that has remained largely unexplored so far due to the absence of suitable instrumentation.

Bibliography

Aizenman, A. M. et al., 2023. The Statistics of Eye Movements and Binocular Disparities during VR Gaming: Implications for Headset Design. *ACM Transactions on Graphics,* 42(1), p. 7.

Akeley, K., Watt, S. J., Girshick, A. R. & Banks, M. S., 2004. A stereo display prototype with multiple focal distances. *ACM Transactions on Graphics,* 23(3), p. 804–813.

Artal, P., 2014. Optics of the eye and its impact in vision: a tutorial. *Advances in Optics and Photonics,* Volume 6, pp. 340-367.

Artal, P., Berrio, E., Guirao, A. & Piers, P., 2002. Contribution of the cornea and internal surfaces to the change of ocular aberrations with age. *Journal of the Optical Society of America A,* 19(1), pp. 137-143.

Artal, P. et al., 2004. Neural compensation for the eye's optical aberrations. *Journal of Vision,* 4(4), pp. 281-7.

Artal, P. et al., 2023. Inverted meniscus intraocular lens as a better optical surrogate of the crystalline lens. *Biomedical Optics Express,* 14(5), pp. 2129-2137.

Artal, P. & Guirao, A., 1998. Contributions of the cornea and the lens to the aberrations of the human eye. *Optics Letters,* 23(21), pp. 1713-1715.

Artal, P., Guirao, A., Berrio, E. & Williams, D. R., 2001. Compensation of corneal aberrations by the internal optics in the human eye. *Journal of Vision,* 1(1), pp. 1-8.

Artal, P., Manzanera, S., Piers, P. & Weeber, H., 2010. Visual effect of the combined correction of spherical and longitudinal chromatic aberrations. *Optics Express,* 18(2), pp. 1637-48.

Atchison, D., 2023. *Optics of the Human Eye*. 2nd ed. s.l.:CRC Press.

Atchison, D. A., Guo, H., Charman, W. N. & Fisher, S. W., 2009. Blur limits for defocus, astigmatism and trefoil. *Vision Research,* 49(19), p. 2393–2403.

Babcock, H. W., 1953. The possibility of compensating astronomical seeing. *The Astronomical Society of the Pacific,* Volume 65, p. 386.

Bach, M., 1996. The Freiburg Visual Acuity Test-automatic measurement of visual acuity. *Optometry and Vision Science,* 73(1), pp. 49-53.

Banks, M., Akeley, K., Hoffman, D. & Girshick, A., 2008. Consequences of Incorrect Focus Cues in Stereo Displays. *Journal of the Society for Information Display,* 24(7), p. 7.

Banks, M. S., Kim, J. & Shibata, T., 2013. *Insight into vergence/accommodation mismatch*. s.l., Proceedings SPIE 8735, Head- and Helmet-Mounted Displays XVIII: Design and Applications, 873509.

Blakemore, C., 1970. The range and scope of binocular depth discrimination in man. *Journal of Physiology,* 211(3), pp. 599-622.

Burns, S. A. et al., 2019. Adaptive optics imaging of the human retina. *Progress in Retinal and Eye Research,* Volume 68, pp. 1-30.

Cánovas, C. et al., 2010. Hybrid adaptive-optics visual simulator. *Optics Letters,* 35(2), pp. 196-198.

Carpio, M. & Malacara, D., 1994. Closed cartesian representation of the Zernike polynomials. *Optics Communications,* 110(5-6), pp. 514-516.

Castejón-Mochón, J. F., López-Gil, N., Benito, A. & Artal, P., 2002. Ocular wave-front aberration statistics in a normal young population. *Vision Research,* 42(13), pp. 1611-1617.

Chang, E., Kim, H. T. & Yoo, B., 2020. Virtual Reality Sickness: A Review of Causes and Measurements. *International Journal of Human–Computer Interaction,* 36(17), p. 1658–1682.

Chen, L., Artal, P., Gutierrez, D. & Williams, D. R., 2007. Neural compensation for the best aberration correction. *Journal of Vision,* 7(10), pp. 1-9.

Collins, M., Bruce, A. & Thompson, B., 1994. Adaptation to monovision. *Int. Contact Lens Clinic,* 21(11-12), pp. 218-224.

Collins, M., Bruce, A. & Thompson, B., 1994. Adaptation to monovision. *International Contact Lens Clinic,* 21(11-12), pp. 218-224.

Cornelissen, S. A. et al., 2010. *MEMS deformable mirrors for astronomical adaptive optics*. s.l., Proceedings SPIE 7736, Adaptive Optics Systems II, 77362D .

Dalimier, E., Dainty, C. & Barbur, J. L., 2008. Effects of higher-order aberrations on contrast acuity as a function of light level. *Journal of Modern Optics,* 55(4-5), p. 791–803.

Doble, N. et al., 2002. Use of a microelectromechanical mirror for adaptive optics in the human eye. *Optics Letters,* 27(17), pp. 1537-1539.

Dreher, A. W., Bille, J. F. & Weinreb, R. N., 1989. Active optical depth resolution improvement of the laser tomographic scanner. *Applied Optics,* 28(4), pp. 804-808.

Duchowski, A. T. et al., 2014. *Reducing visual discomfort of 3D stereoscopic displays with gaze-contingent depth-of-field.* s.l., Proceedings of the ACM Symposium on Applied Perception, p. 39–46.

Elliott, S. L. et al., 2009. Role of high-order aberrations in senescent changes in spatial vision. *Journal of Vision,* 9(2), p. 24.

Fernández, E. J., 2012. Adaptive Optics for Visual Simulation. *International Scholarly Research Notices,* Issue 1.

Fernández, E. J. & Artal, P., 2003. Membrane deformable mirror for adaptive optics: performance limits in visual optics. *Optics Express,* 11(9), pp. 1056-1069.

Fernández, E. J. & Artal, P., 2005. Study on the effects of monochromatic aberrations in the accommodation response by using adaptive optics. *Journal of the Optical Society of America A,* 22(9), pp. 1732-1738.

Fernández, E. J., Iglesias, I. & Artal, P., 2001. Closed-loop adaptive optics in the human eye. *Optics Letters,* 26(10), pp. 746-748.

Fernández, E. J., Manzanera, S., Piers, P. & Artal, P., 2002. Adaptive optics visual simulator. *Journal of Refractive Surgery,* 18(5), pp. S634-8.

Fernández, E. J., Prieto, P. M. & Artal, P., 2009. Binocular adaptive optics visual simulator. *Optics Letters,* 34(17), pp. 2628-2630.

Fernández, E. J., Prieto, P. M. & Artal, P., 2010. Adaptive optics binocular visual simulator to study stereopsis in the presence of aberrations. *Journal of the Optical Society of America A,* 27(11), pp. 48-55.

Fernández, E. J. et al., 2013. Impact on stereo-acuity of two presbyopia correction approaches: monovision and small aperture inlay. *Biomedical Optics Express,* 4(1), pp. 822-830.

Fernández, E. J. et al., 2006. Adaptive optics with a magnetic deformable mirror: applications in the human eye. *Optics Express,* 14(20), pp. 8900-8917.

Fry, G., 1939. Further experiments on the accommodative convergence relationship. *American Journal of Optometry,* 16(9), p. 325–334.

García-Pedreño, C. et al., 2026. Halo assessment in intraocular lenses through high dynamic range images. *Journal of Cataract & Refractive Surgery,* 52(3), pp. 296-302.

Guirao, A., Porter, J., Williams, D. R. & Cox, I. G., 2002. Calculated impact of higher-order monochromatic aberrations on retinal image quality in a population of human eyes. *Journal of the Optical Society of America A,* 19(3), pp. 1-9.

H. Rouger, Y. B. D. G. R. L., 2010. Visual Tasks Dependence of the Neural Compensation for the Keratoconic Eye's Optical Aberrations. *Journal of Optometry,* 3(1), pp. 60-65.

Hartmann, J., 1900. Bemerkungen uber den Bau und die Justirung. *Z Instrumentenkd ,* Volume 20, pp. 47-58.

Harwerth, R. S., Fredenburg, P. & Smith, E., 2003. Temporal integration for stereoscopic vision. *Vision Research,* 43(5), pp. 505-17.

Hermann, B. et al., 2004. Adaptive-optics ultrahigh-resolution optical coherence tomography. *Optics Letters,* 29(18), pp. 2142-2144.

Hervella, L., Villegas, E. A., Prieto, P. M. & Artal, P., 2019. Assessment of subjective refraction with a clinical adaptive optics visual simulator. *Journal of Cataract & Refractive Surgery,* 45(1), pp. 87-93.

Hervella, L., Villegas, E. A., Robles, C. & Artal, P., 2020. Spherical Aberration Customization to Extend the Depth of Focus With a Clinical Adaptive Optics Visual Simulator. *Journal of Refractive Surgery,* 36(4), pp. 223-229.

Hess, R. F. et al., 2016. A Robust and Reliable Test to Measure Stereopsis in the Clinic. *Investigative Ophthalmology and Vision Science,* 57(3), pp. 798-804.

Hillaire, S., Lecuyer, A., Cozot, R. & Casiez, G., 2008. *Using an Eye-Tracking System to Improve Camera Motions and Depth-of-Field Blur Effects in Virtual Environments*. s.l., IEEE Virtual Reality Conference, pp. 47-50.

Hofer, H. et al., 2001. Improvement in retinal image quality with dynamic correction of the eye's aberrations. *Optics Express,* 8(11), pp. 631-643.

Hoffman, D. M., Girshick, A. R., Akeley, K. & Banks, M. S., 2008. Vergence–accommodation conflicts hinder visual performance and cause visual fatigue. *Journal of Vision,* 8(3), pp. 1-30.

Hu, X. & Hua, H., 2014. High-resolution optical see-through multi-focal-plane head-mounted display using freeform optics. *Optics Express,* 22(11), pp. 13896-13903.

Jaeken, B. et al., 2015. Comparison of presbyopia correcting IOL's profiles with a clinical adaptive optics instrument. *Investigative Ophthalmology and Vision Science,* 56(7), p. 2982.

Jaeken, B. et al., 2014. Clinical Validation of Adaptive-Optics Guided Refraction. *Investigative Ophthalmology and Vision Science,* 55(13), p. 2114.

Kim, J., Kane, D. & Banks, M. S., 2014. The rate of change of vergence–accommodation conflict affects visual discomfort. *Vision Research,* Volume 105, pp. 159-165.

Kramida, G., 2016. Resolving the Vergence-Accommodation Conflict in Head-Mounted Displays. *IEEE Transactions on Visualization and Computer Graphics,* 22(7), pp. 1912-1931.

Krotkov, E., 1988. Focusing. *International Journal of Computer Vision,* 1(3), p. 223–237.

Kujawinska, M., Porras-Aguilar, R. & Zaperty, W., 2012. LCoS spatial light modulators as active phase elements of full-field measurement systems and sensors. *Metrology and Measurement Systems,* Volume 19, pp. 445-458.

Lakshminarayanan, V. & Fleck, A., 2011. Zernike polynomials: a guide. *Journal of Modern Optics,* 58(18), p. 545–561.

Liang, J., Grimm, B., Goelz, S. & Bille, J. F., 1994. Objective measurement of wave aberrations of the human eye with the use of a Hartmann-Shack wave-front sensor. *Journal of the Optical Society of America A,* 11(7), pp. 1949-57.

Liang, J., Williams, D. R. & Miller, D. T., 1997. Supernormal vision and high-resolution retinal imaging through adaptive optics. *J. Opt. Soc. Am. A,* Volume 14, pp. 2884-2892.

Lin, T. et al., 2020. Maxwellian near-eye display with an expanded eyebox. *Optics Express,* 28(26), pp. 38616-38625.

Lin, Z. et al., 2019. Zhenghua Lin, Zhao Chen, Wenyu Gao, Can Chen, Weizhong Lan, Zhikuang Yang. *Chin J Optom Ophthalmol Vis Sci*.

Lyu, J., Ng, C. J., Bang, S. P. & Yoon, G., 2021. Binocular accommodative response with extended depth of focus under controlled convergences. *Journal of Vision,* 21(8), p. 21.

Madec, P. Y., 2012. *Overview of deformable mirror technologies for adaptive optics and astronomy.* s.l., Proceedings SPIE 8447, Adaptive Optics Systems III.

Maimone, A. et al., 2014. Pinlight displays: wide field of view augmented reality eyeglasses using defocused point light sources. *ACM Transactions on Graphics,* 33(4).

Manzanera, S. et al., 2007. Liquid crystal Adaptive Optics Visual Simulator: Application to testing and design of ophthalmic optical elements. *Optics Express,* 15(24), pp. 16177-16188.

Marcos, S. et al., 2022. Adaptive optics visual simulators: a review of recent optical designs and applications [Invited]. *Biomedical Optics Express,* 13(12), pp. 6508-6532.

Marcos, S., Artal, P., Lundström, L. & Yoon, G., 2025. Visual simulation of intraocular lenses: technologies and applications [Invited]. *Biomedical Optics Express,* 16(3), pp. 1025-1042.

Marcos, S. et al., 2021. Simulating Outcomes of Cataract Surgery: Important Advances in Ophthalmology. *Annual Review of Biomedical Engineering,* Volume 23, pp. 277-306.

Marcos, S., Sawides, L., Gambra, E. & Dorronsoro, C., 2008. Influence of adaptive-optics ocular aberration correction on visual acuity at different luminances and contrast polarities. *Journal of Vision,* 8(13), p. 1.

Marcos, S. et al., 2017. Vision science and adaptive optics, the state of the field. *Vision Research,* Volume 132, pp. 3-33.

Martin, J. et al., 2011. Unbiased estimation of refractive state of aberrated eyes. *Vision Research,* 51(17), pp. 1932-40.

McShane, B. et al., 2019. Abandon Statistical Significance. *The American Statistician,* Volume 73, p. 235–245.

Mompeán, J., Aragón, J. L., Prieto, P. M. & Artal, P., 2019. GPU-based processing of Hartmann–Shack images for accurate and high-speed ocular wavefront sensing. *Future Generation Computer Systems,* Volume 91, pp. 177-190.

Ng, C. J. et al., 2021. Optics and neural adaptation jointly limit human stereovision. *Proceedings of the National Academy of Sciences of the United States of America,* 118(23).

Niu, K. & Tian, C., 2022. Zernike polynomials and their applications. *Journal of Optics,* 24(12).

Ogle, K. N., 1932. An analytical treatment of the longitudinal horopter, its measurement and application to related phenomena, especially to the relative size and shape of the ocular images. *Journal of the Optical Society of America,* 12(22), pp. 665-728.

Otero, C. et al., 2015. Repeatability of aberrometric measurements with a new instrument for vision analysis based on adaptive optics. *Journal of Refractive Surgery,* 31(3), pp. 188-94.

Panum, P. L., 1858. *Physiologische Untersuchungen über das Sehen*. s.l.:Schwers'sche Buchhandlung.

Percival, A. S., 1892. The relation of convergence to accommodation and its practical bearing. *Ophthalmological Review,* Volume 11, p. 313–328.

Perez, G. M. et al., 2013. Customizing depth of focus outcomes in Hyperopic Lasik using an Adaptive Optics Vision Analyzer. *Investigative Ophthalmology and Vision Science,* 54(15).

Pieh, S. et al., 2002. Comparison of visual acuities at different distances and defocus curves. *Journal of Cataract & Refractive Surgery,* 28(11), pp. 1964-7.

Piers, P. A. et al., 2004. Adaptive Optics Simulation of Intraocular Lenses with Modified Spherical Aberration. *Investigative Ophthalmology and Vision Science,* 45(12), pp. 4601-4610.

Platt, B. C. & Shack, R., 2001. History and Principles of Shack-Hartmann Wavefront Sensing. *Journal of Refractive Surgery,* 17(5), pp. 573-S577.

Platt, B. & Shack, R., 1971. Lenticular Hartmann-screen. *Journal of the Optical Society of America,* Volume 61, pp. 656-661.

Prieto, P. M., Fernández, E. J., Manzanera, S. & Artal, P., 2004. Adaptive optics with a programmable phase modulator: applications in the human eye. *Optics Express,* Volume 12, pp. 4059-4071.

Prieto, P. M., Vargas-Martín, F., Goelz, S. & Artal, P., 2000. Analysis of the performance of the Hartmann–Shack sensor in the human eye. *Journal of the Optical Society of America A,* 17(8), pp. 1388-1398.

Rocha, K. M., Vabre, L., Chateau, N. & Krueger, R. R., 2009. Expanding depth of focus by modifying higher-order aberrations induced by an adaptive optics visual simulator. *Journal of Cataract & Refractive Surgery,* 11(35), p. 1885.

Rosen, R., Lundstrom, L. & Unsbo, P., 2012. Adaptive Optics for Peripheral Vision. *Investigative Ophthalmology and Vision Science,* 53(14).

Sabesan, R., Zheleznyak, L. & Yoon, G., 2012. Binocular visual performance and summation after correcting higher order aberrations. *Biomedical Optics Express,* 3(12), pp. 3176-89.

Sager, S., Gambín, A., Prieto, P. M. & Artal, P., 2025. Binocular adaptive optics visual simulator with convergence control. *Biomedical Optics Express,* 16(10), pp. 4017-4026.

Sager, S., Prieto, P. M. & Artal, P., 2026. Effect of spherical aberration on the vergence-accommodation conflict. *Biomed. Opt. Express,* 17(4), pp. 1782-1793.

Sharples, S., Cobb, S., Moody, A. & Wilson, J. R., 2008. Virtual reality induced symptoms and effects (VRISE): Comparison of head mounted display (HMD), desktop and projection display systems. *Displays,* 29(2), pp. 58-69.

Sheard, C., 1934. The prescription of prisms. *American Journal of Optometry,* Volume 11, p. 364–378.

Shetty, N. et al., 2019. Patient-specific determination of change in ocular spherical aberration to improve near and intermediate visual acuity of presbyopic eyes. *Journal of Biophotonics,* 12(4).

Shetty, R. et al., 2017. Repeatability of a Commercially Available Adaptive Optics Visual Simulator and Aberrometer in Normal and Keratoconic Eyes. *Journal of Refractive Surgery,* 33(11), pp. 769-772.

Shetty, R. et al., 2017. Keratoconus Screening Indices and Their Diagnostic Ability to Distinguish Normal From Ectatic Corneas. *American Journal of Ophthalmology,* Volume 181, pp. 140-148.

Shibata, T., Kim, J., Hoffman, D. M. & Banks, M. S., 2011. The zone of comfort: Predicting visual discomfort with stereo displays. *Journal of Vision,* 11(8).

Soomro, S. R. et al., 2024. Head-mounted adaptive optics visual simulator. *Biomedical Optics Express,* 15(2), pp. 608-623.

Spiegel, D. & Erkelens, I., 2024. Vergence-accommodation conflict increases time to focus in augmented reality. *Journal of the Society for Information Display,* 32(5), p. 194–205.

State, A. et al., 2001. *Dynamic virtual convergence for video see-through head-mounted displays: maintaining maximum stereo overlap throughout a close-range work space*. s.l., Proceedings IEEE and ACM International Symposium on Augmented Reality, pp. 137-146.

Suchkov, N., Fernández, E. J. & Artal, P., 2019. Impact of longitudinal chromatic aberration on through-focus visual acuity. *Optics Express,* 27(24), pp. 35935-35947.

Suchkov, N., Fernández, E. J. & Artal, P., 2019. Wide-range adaptive optics visual simulator with a tunable lens. *Journal of the Optical Society of America A,* 36(5), pp. 722-730.

Suyama, S., Date, M. & Takada, H., 2000. Three-Dimensional Display System with Dual-Frequency Liquid-Crystal Varifocal Lens. *Japanese Journal of Applied Physics,* Volume 39, pp. 480-484.

Tabernero, J. et al., 2025. Depth of focus as a function of spherical aberration using adaptive optics in pseudophakic subjects. *Journal of Cataract & Refractive Surgery,* 51(4), p. 307–13.

Ukwade, M. T., Bedell, H. E. & Harwerth, R. S., 2003. Stereopsis is perturbed by vergence error. *Vision Research,* 43(2), pp. 181-193.

Vargas-Martín, F., Prieto, P. M. & Artal, P., 1998. Correction of the aberrations in the human eye with a liquid-crystal spatial light modulator: limits to performance. *Journal of the Optical Society of America A,* 15(9), pp. 2552-2562.

Villegas, E. A. et al., 2020. Visual simulation to customize depth of focus with new aspheric IOLs. *Investigative Ophthalmology and Vision Science,* 61(7), p. 587.

Villegas, E. A. et al., 2019. Effect of Crystalline Lens Aberrations on Adaptive Optics Simulation of Intraocular Lenses. *Journal of Refractive Surgery,* 35(2), pp. 126-131.

Vinas, M. et al., 2015. Longitudinal chromatic aberration of the human eye in the visible and near infrared from wavefront sensing, double-pass and psychophysics. *Biomedical Optics Express,* 6(3), pp. 948-62.

Waldkirch, M. v., Lukowicz, P. & Tröster, G., 2004. *Spectacle-Based Design of Wearable See-Through Display for Accommodation-Free Viewing*. s.l., Pervasive Computing, p. 106–123.

Wang, Y. J. & Lin, Y. H., 2021. Liquid crystal technology for vergence-accommodation conflicts in augmented reality and virtual reality systems: a review. *Liquid Crystal Reviews,* Volume 9, pp. 1-52.

Watson, A. B. & Pelli, D. G., 1983. Quest: A Bayesian adaptive psychometric method. *Perception & Psychophysics,* 33(2), p. 113–120.

Wichmann, F. A. & Hill, N. J., 2001. The psychometric function: I. Fitting, sampling, and goodness of fit. *Perception & Psychophysics,* 63(8), pp. 1293-1313.

Wichmann, F. & Hill, N., 2001. The psychometric function: II. Bootstrap-based confidence intervals and sampling. *Perception & Psychophysics,* 63(8), p. 1314–1329.

Williams, D. et al., 2000. Visual benefit of correcting higher order aberrations of the eye. *Journal of Refractive Surgery,* 16(5), p. S554–S559.

Yin, K. et al., 2022. Advanced liquid crystal devices for augmented reality and virtual reality displays: principles and applications. *Light: Science & Applications,* 11(1), p. 161.

Yoon, G. Y. & Williams, D. R., 2002. Visual performance after correcting the monochromatic and chromatic aberrations of the eye. *Journal of the Optical Society of America A,* 19(2), p. 266–275.

Zernike, F. & Stratton, F. J. M., 1934. Diffraction Theory of the Knife-Edge Test and its Improved Form, The Phase-Contrast Method. *Monthly Notices of the Royal Astronomical Society,* 94(5), p. 377–384.

Zhang, Z., You, Z. & Chu, D., 2014. Fundamentals of phase-only liquid crystal on silicon (LCOS) devices. *Light: Science & Applications,* Volume 3, p. 213.

Zhan, T., Xiong, J., Zou, J. & Wu, S., 2020. Multifocal displays: review and prospect. *PhotoniX,* 1(1), p. 10.

Zheleznyak, L. et al., 2013. Modified monovision with spherical aberration to improve presbyopic through-focus visual performance. *Investigative Ophthalmology and Vision Science,* 54(5), pp. 3157-65.

Agradecimientos

En primer lugar, quiero agradecer a mis directores Pablo Artal y Pedro Prieto. A Pablo por haberme dado la oportunidad de realizar investigación en ciencias de la visión, primero a través de Voptica y después gracias a este programa de doctorado. A Pedro por las incontables horas de diálogo, con las que he aprendido más que con ningún otro programa académico. También quiero agradecer a todo el equipo del LOUM y de Voptica, cuya ayuda ha sido invaluable a lo largo de estos años. En particular quiero mencionar a Adrián, que ha desarrollado gran parte del software usado en esta tesis; a Ortega, que ha diseñado los componentes optomecánicos usados en el instrumento; a Alba, que me ha enseñado muchísimo desde que entré en Voptica; y a Rosa, que siempre me ha ayudado con todas las gestiones necesarias desde el inicio.

Por supuesto, valoro enormemente todas las conversaciones tanto personales como profesionales que he tenido con el resto del equipo. Tanto de profesores que me han ayudado con lo que ha hecho falta como Josua, Eloy, Juanma, Esther y Antonio; como del resto del equipo en Voptica con los que he compartido tantas horas juntos como Jose Belmonte, David, Lucía, Luis y Maria Dolores. Y para terminar, mi más sincera gratitud hacia el resto de integrantes del chapter de Optica cuya compañía y amistad me ha acompañado a lo largo de esta etapa. A Lin, Vahid, Consu, Rosa y Raúl que han estado conmigo desde que empecé y con quienes hemos hecho mil y una actividades; a Pedro, Arturo y Clara por todas las tardes de juegos de mesa y trivia; a Alex, Marta, Roberto y Anuar por compartir tantas horas escalando y fortaleciendo cuerpo y mente.

A nivel personal, un agradecimiento eterno a todas las personas en las que me he apoyado durante este tiempo. A mi madre, mi padre y mis hermanos que siempre han estado ahí para cualquier cosa que me hiciera falta. A Marta, Marqués, Lu, Martín y el pequeño Samu, quienes siempre han prestado un oído atento a todos mis problemas. Y por supuesto a Pablo, Juan, JV, Miguel, Draguini, Adri y Cano que me han tenido que aguantar en nuestras aventuras por el mundo real y por otros tantos ficticios.

Muchas gracias desde el fondo de mi corazón a todos aquellos que habéis formado parte de este viaje.